DEPARTMENT OF NANOBIOTECHNOLOGY

SUPERVISOR: Prof. Dr. Wolfgang Knoll

New Amplification Strategies for Fluorescence Biosensors

DISSERTATION FOR OBTAINING THE DOCTORAL DEGREE
UNIVERSITY OF NATURAL RESOURCES AND LIFE SCIENCES, VIENNA

SUBMITTED BY
Koji Toma

VIENNA, JULY 2012

ACKNOWLEDGEMENTS

Prof. Knoll Wolfgang

Dr. Jakub Dostalek

Mana Toma

Dr. Chun-Jen Huang

Dr. Yi Wang

Martin Bauch

All Nanos at AIT Austrian Institute of Technology GmbH

Prof. Pum Dietmar

ABSTRACT

This thesis focuses on new fluorescence-based biosensors with advanced sensitivity in detection of molecular analytes. Particularly, new amplification strategies based on the interaction of fluorophore labels with intense and confined field of surface plasmons are pursued in order to enhance the fluorescence signal by increasing the excitation rate and by controlling the angular distribution of emitted light. The thesis comprises the experimental and theoretical study of plasmon-mediated emission on metallic nanostructures supporting coupled surface plasmon modes (long range and Bragg-scattered surface plasmons). The results show that the emission via these modes combined with reverse Kretschmann configuration allows to confine the fluorescence intensity in specific polar and azimuth directions. These features enable to achieve high emission directionality and thus advance the collection efficiency of emitted fluorescence light. The majority of fluorescence light can be delivered to a detector, which is substantial improvement with respect to regular sensors where only a few per cent of emitted photons are detected. The observed phenomena were applied for sensitive detection of molecular analytes by using fluorescence immunoassays, hydrogel-based binding matrix, and specifically designed sensor surfaces supporting surface plasmon modes. In addition, the implementation of surface plasmon-enhanced fluorescence to compact biochip that allows for the simplification of the overall sensor setup and that is suitable for portable biosensors devices was carried out. The achieved results provide leads on further advancing the sensitivity of fluorescence biosensors. The thesis is structured to five chapters. The first chapter provides an introduction and an overview of the current state-of-the-art. The second chapter defines the project goals and the third chapter summarizes the results achieved in four specific projects. The first two projects embrace the investigation of long range surface plasmon and Bragg-scattered surface plasmon-coupled fluorescence emission. The third project focuses on immunoassay-based detection with fluorescence intensity enhancement by Bloch surface waves on dielectric one-dimensional photonic crystals. In the fourth project, a new compact biochip with integrated diffractive optical elements for plasmon-enhanced fluorescence was carried out. The chapter four provides summary of achieved results and in the last chapter number five the published papers are attached.

TABLE OF CONTENT

1. INTRODUCTION

After rapid advances in biology in the fields of genomics, proteomics and bioinformatics we observed since 1990s, a number of biomolecules that cause diseases or can be used as biomarkers have been discovered [1-3]. The analysis of these compounds became an irreplaceable tool in various application areas of modern society such as medical diagnostics, food control, and environmental monitoring [4]. For the analysis of protein and DNA analytes, mostly enzyme-linked immunoassays (ELISA) [5] and polymerase chain reaction (PCR) [6] – based methods are used, respectively. These established technologies provide reliable means for many routine tests. However they need trained personnel and sophisticated instruments that have to be operated in specialized laboratories. In addition, the analysis typically require from several hours to a few days as they rely on laborious multi-step procedures. Therefore, increasing efforts are devoted to research in new technologies that can detect and analyze harmful compounds and biomarkers in emergency situations and point-of-care testing [7, 8]. For these scenarios, new tools enabling rapid, sensitive detection by portable devices represent a key.

Biosensors are the devices that are designed to fulfill these needs. After their introduction in 1962 with a paper by Clark and Lyons [9], they are attracting gradually increasing attention in broad range of applications [4]. Biosensors are composed of two key parts: a sensitive biological element and a transducer. The biological element specifically interacts with an analyte of interest and the transducer platform translates this interaction into signal. Up to now biosensors exploiting mainly three different transducer techniques have been proposed – electrochemical [10-15], optical [16-23] and piezoelectric [24, 25]. In optical sensors, changes in absorbance [16, 17], fluorescence [18, 19], chemiluminescence [20, 21] or light reflectivity [22, 23] are measured. Among them, fluorescence-based detection is one of the most widely used techniques due to the intrinsic sensitivity, safety, easy handling and availability of fluorophores. In this method, fluorophores are used as labels that report the presence of target analyte in analyzed samples.

With use of fluorophores-based sensors, the ultra-high sensitivity enabling single molecule detection has been reported [26, 27]. However they require highly sophisticated and bulky

devices with well-trained experts for the operation. Therefore they are not suited for emergency situations, point-of-care medical diagnostics, security and food control or environmental monitoring which are typically performed outside specialized laboratories. For such application fields, it is urgently needed to develop biosensors that are capable of sensitive and rapid detection and real-time monitoring in simplified compact devises.

1.1. Guided waves and Fluorescence at surfaces

1.1.1. Surface plasmons on planar metallic films

Surface plasmons (SPs) propagating on semi-infinite thick gold film are described in this section. Further, let us consider Cartesian coordinate system with a planar interface in xz-plane between semi-infinite, homogeneous and non-magnetic metal and dielectric with optical properties described by spatially isotropic frequency-dependent complex $\varepsilon_m(\omega)$ and real dielectric constants $\varepsilon_s(\omega)$, respectively (See Figure 1).

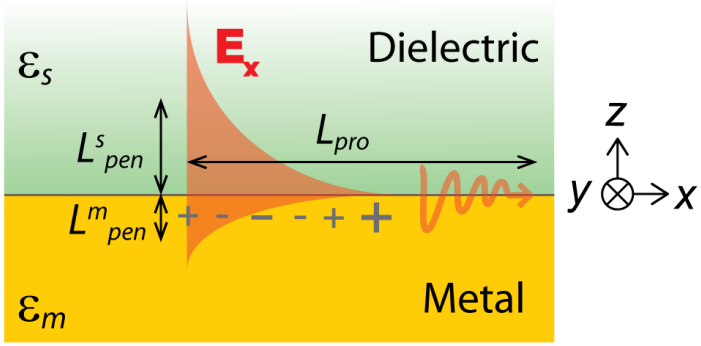

Figure 1 Semi-infinite planar metal-dielectric interface with Cartesian coordinates.

From Maxwell's equations and boundary conditions which require continuity of parallel components (x-direction) of electric and magnetic field amplitudes to a surface, the dispersion relation of SPs at a planar metal-dielectric interface can be derived as [28]:

$$k_{SP} \equiv k_x = \frac{\omega_0}{c_0}\sqrt{\frac{\varepsilon_s \varepsilon_m}{\varepsilon_s + \varepsilon_m}} = k_0\sqrt{\frac{\varepsilon_s \varepsilon_m}{\varepsilon_s + \varepsilon_m}}, \quad (1)$$

where k_x is a parallel component of propagation constant, ω_0, c_0 and k_0 are angular frequency,

speed and a propagation constant of light in vacuum, respectively. As shown in Figure 2, in z-direction (perpendicular to a surface) the SP field is transverse magnetic (TM) polarized and peaks at the interface. It decays exponentially into the metal and dielectric. Its confinement can be described by a penetration depth L^{j}_{pen} (j=s, m for a dielectric or metal, respectively) defined as a distance from a surface at which the amplitude of the evanescent field drops by a factor of 1/e:

$$L^{\mathrm{s}}_{\mathrm{pen}} \equiv \mathrm{Re}\left[\left(k_{\mathrm{SP}}^2 - \varepsilon_{\mathrm{s}} k_0^2\right)^{-\frac{1}{2}}\right], \tag{2}$$

$$L^{\mathrm{m}}_{\mathrm{pen}} \equiv \mathrm{Re}\left[\left(k_{\mathrm{SP}}^2 - \tilde{\varepsilon}_{\mathrm{m}} k_0^2\right)^{-\frac{1}{2}}\right]. \tag{3}$$

In x-direction (parallel to a surface) the electromagnetic field of SPs propagates along the surface and dissipates due to the damping in a metal film (ohmic loss). As with the penetration depth, this characteristic is described by a propagation length L_{pro} defined as a distance from the excitation point at which the amplitude of the SP field drops by a factor of 1/e. The propagation length of SPs is given by:

$$L_{\mathrm{pro}} \equiv \frac{1}{\mathrm{Im}[k_{\mathrm{SP}}]}. \tag{4}$$

For the sake of illustration, typical characteristics of SPs are calculated by using equation (2)-(4) for a dielectric with the refractive index n_{s}=1.332 and gold with n_{m}=0.153+3.52i at the wavelength 633 nm. The penetration depth and propagation length are $L^{\mathrm{s}}_{\mathrm{pen}}$=185 nm, $L^{\mathrm{m}}_{\mathrm{pen}}$=26 nm and L_{pro}~10 μm, respectively. Let us note that the `1relation between dielectric constants ε and refractive index n is ε=(Re[n]^2 -Im[n]^2)+2Re[n]Im[n].

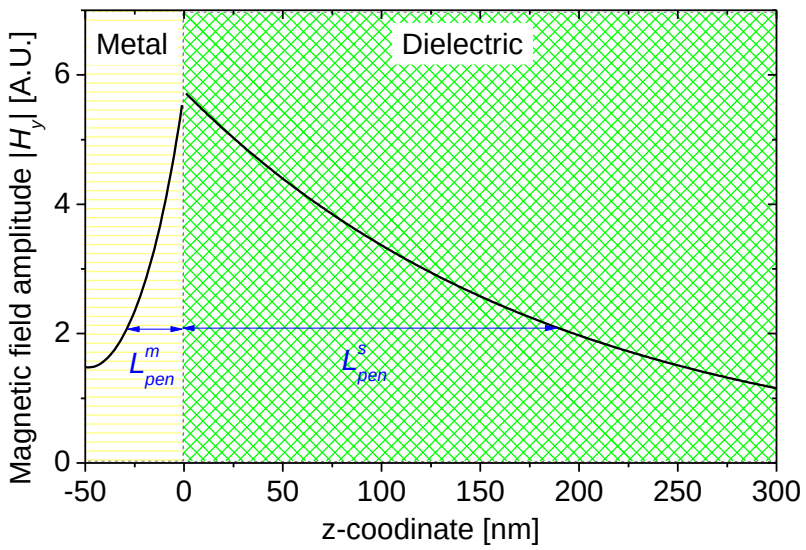

Figure 2 Simulated magnetic field amplitude of SPs propagating along the interface of gold (n_m=0.153+3.52i) and dielectric (n_s=1.332) at the wavelength λ=633 nm.

In addition, let us consider a modified geometry with a thin planar metallic film with a thickness t_m and refractive index n_m sandwiched between two semi-infinite dielectrics with a refractive index n_s (Figure 3a). When the thickness t_m is close to L^m_{pen}, SPs on the opposite interfaces of the metal film can interact each other. For refractive index symmetrical geometries, the interaction gives rise to two new coupled SP modes with symmetrical and anti-symmetrical profile of field. These modes can be distinguished by their energy loss properties and related to their relative propagation lengths. They are referred to as long range surface plasmon (LRSP) that is a low-loss wave and propagates longer distance and short range surface plasmon (SRSP) that is a high-loss wave [29]. LRSP and SRSP obey the dispersion relation [30]:

$$\tan\left(\kappa t_m\right) = \frac{2\left(\gamma n_m^2 / \kappa n_s^2\right)}{1-\left(\gamma n_m^2 / \kappa n_s^2\right)^2}, \tag{5}$$

where $\kappa=(k_0^2 n_m^2 - k_{SP}^2)^{1/2}$ and $\gamma=(k_{SP}^2 - k_0^2 n_s^2)^{1/2}$.

For the sake of illustration, typical characteristics of LRSP and SRSP are calculated by using equation (5) for a dielectric with the refractive index n_s=1.332 and gold with t_m=20 nm and n_m=0.2+2.68i at the wavelength 633 nm. The propagation length of LRSP and SRSP are $L_{pro,LRSP}$=88 μm and $L_{pro,SRSP}$=0.3 μm, respectively.

As shown in Figure 3b, with respect to the penetration depth of SPs $L^{s}_{pen,SP}$ that is typically about 200 nm, that of LRSPs $L^{s}_{pen,LRSP}$ that is close to 500 nm.

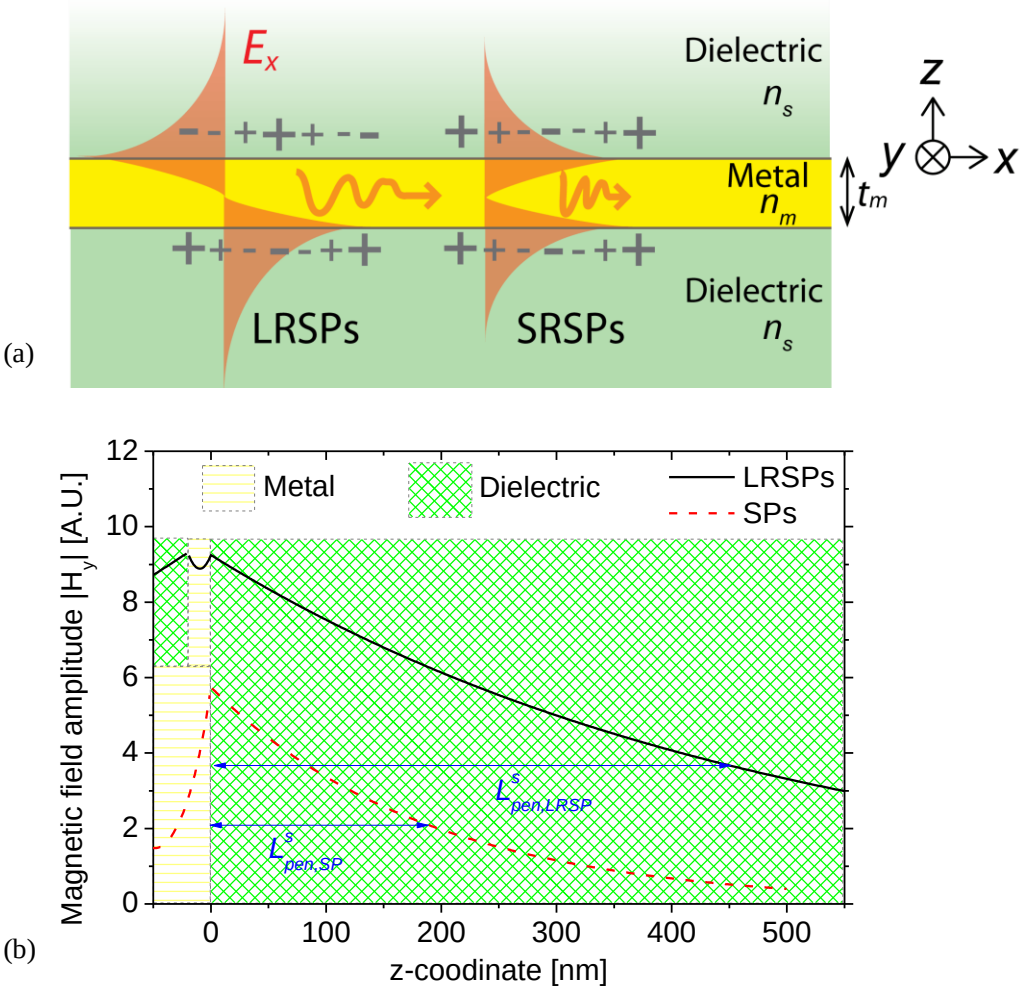

Figure 3 (a) Layer structures supporting long range (LRSPs) and short range (SRSPs) surface plasmons. (b) Simulated magnetic field amplitude of LRSPs (black solid) propagating along the interface between a gold film (n_m=0.2+2.68i) with the thickness t_m=20 nm and a dielectric (n_s=1.332) at the wavelength λ=633 nm. As a comparison, that of SPs is also shown in the figure (red dashed).

1.1.2. Surface plasmons on Bragg gratings

The characteristics of SPs can be modified by periodically corrugating a metallic surface. Here let us consider geometry with the sinusoidally modulated surface with a period Λ and depth d. When the wave vector of SPs $\boldsymbol{k}_{\mathbf{SP}}$ [equation (1)] is half of the grating vector $\boldsymbol{G}$ ($|\boldsymbol{G}|=G=2\pi/\Lambda$), Bragg scattering of SPs can occur which results in the coupling of forward and backward propagating SPs. They can interfere constructively to form a standing wave. This scattering leads to a split in the dispersion relation of SPs and plasmonic band gap opens up at a wavelength. In the band gap, SPs cannot propagate because SPs propagating opposite directions interfere destructively [31, 32] (see Figure 4). According to the work of Barnes et al. [31], the width of a band gap in frequency $\Delta\omega$ can be derived from:

$$\frac{\Delta\omega}{\omega_0}=\frac{\alpha}{\sqrt{-\varepsilon_m\varepsilon_s}}\left(\frac{\varepsilon_m\varepsilon_s}{\varepsilon_m+\varepsilon_s}\right)\left\{1-2\alpha^2+\frac{\alpha^2}{2(-\varepsilon_m\varepsilon_s)}\left(\frac{\varepsilon_m\varepsilon_s}{\varepsilon_m+\varepsilon_s}\right)^2+O(\alpha)^4\right\}, \tag{6}$$

where

$$\left(\frac{\omega_0}{c_0}\right)^2=\left(\frac{G}{2}\right)^2\frac{\varepsilon_m+\varepsilon_s}{\varepsilon_m\varepsilon_s}, \tag{7}$$

and $\alpha=G/2\times d/2$, ω_0 is the SPs frequency without corrugation, c_0 are speed of light in vacuum, respectively, ε_m and ε_s are dielectric constants of metal and dielectric.

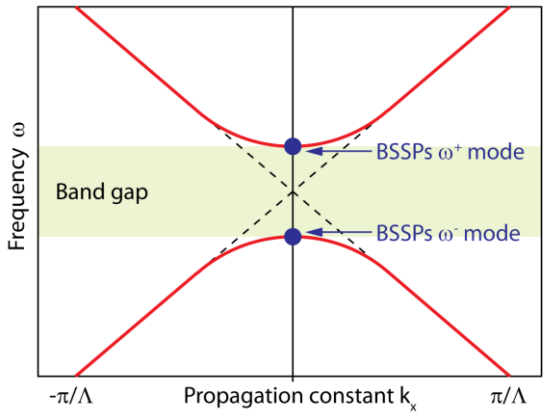

Figure 4 Schematic of dispersion relation of BSSPs.

At the edges of the band gap, the constructive interference of surface plasmon modes leads to the occurrence of new modes. They exhibit electric field intensity localized at grating peaks (ω^-)

and valleys (ω^+). Those new modes are referred to as Bragg scattered surface plasmons (BSSPs) ω^- and ω^+ mode corresponding to their relative resonance frequencies. For the sake of illustration, typical characteristics of BSSP fields are simulated by using finite element method (FEM) for a dielectric with the refractive index n_s=1.332 and 1.330, and gold with n_m=0.186+3.51 and 0.147+4.30i at the wavelength 633 nm (ω^+) and 710 nm (ω^-), respectively as shown in Figure 5. The gold surface is sinusoidally corrugated with a period Λ=230 nm and depth d=30 nm.

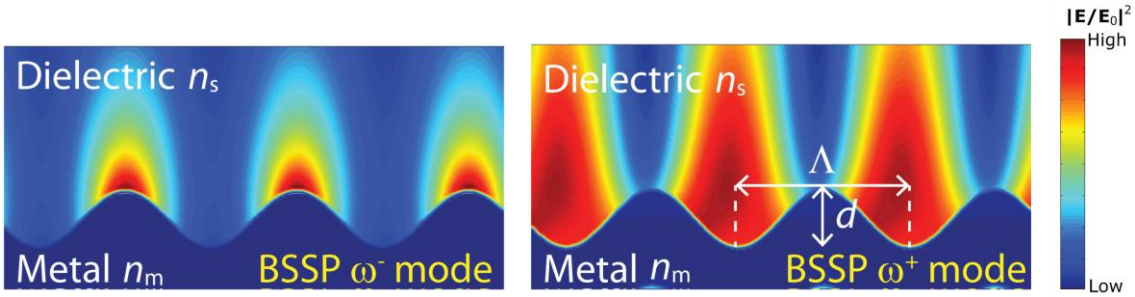

Figure 5 Simulated electric field intensity of BSSPs ω^- (right) and ω^+ (left) mode on sinusoidally corrugated gold with Λ=230 nm and d=30 nm. The refractive indices of gold and dielectric are n_m=0.186+3.51 and 0.147+4.30i, n_s=1.332 and 1.330 at the wavelength 633 nm (ω^+ mode) and 710 nm (ω^- mode), respectively

1.1.3. Bloch surface waves

Now let us consider one dimensional photonic crystal (1DPC) composed of repetitive stack of high (n_H) and low (n_L) refractive index dielectric layers as shown in Figure 6a. 1DPC supports electromagnetic waves called Bloch surface waves (BSWs) [33-41]. Similarly to SPs, the field is confined at the interface of 1DPC and decays exponentially from the surface (see Figure 6b).

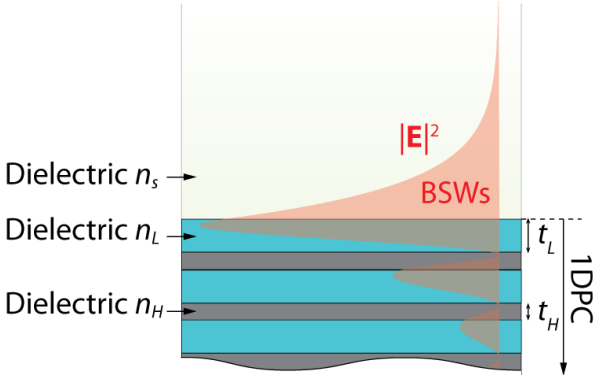

(a)

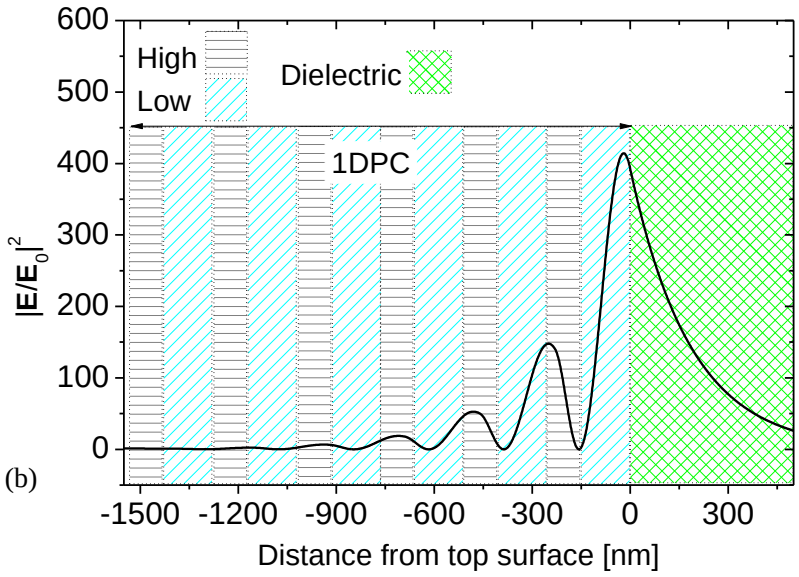

Figure 6 (a) Layer structures of 1DPC supporting BSWs. (b) Simulated electric field intensity enhancement of BSWs propagating along the interface between 1DPC composed of 6 repetitive stack of high (n_H=2.403+0.0013i, t_H=80 nm) and low (n_L=1.7844+0.0001i, t_L=150 nm) refractive index dielectrics, and dielectric (n_s=1.332) at the wavelength λ=633 nm.

1.1.4. Coupling of surface plasmons

Since the propagation constant of guided waves (SPs and BSWs) is always larger than that of light in a media with the refractive index n_s, the surface waves cannot be excited by the direct incidence of light (e.g. SPs shown in Figure 7). The main approaches for the coupling of the light to SPs are attenuated total reflection (prism coupling), diffraction on a periodically corrugated metallic surface (grating coupling) and dielectric waveguides (waveguide coupling) [42, 43]. These methods allow to increase the parallel component of propagation constant of the light to match Re[k_{SP}]. as shown in Figure 7

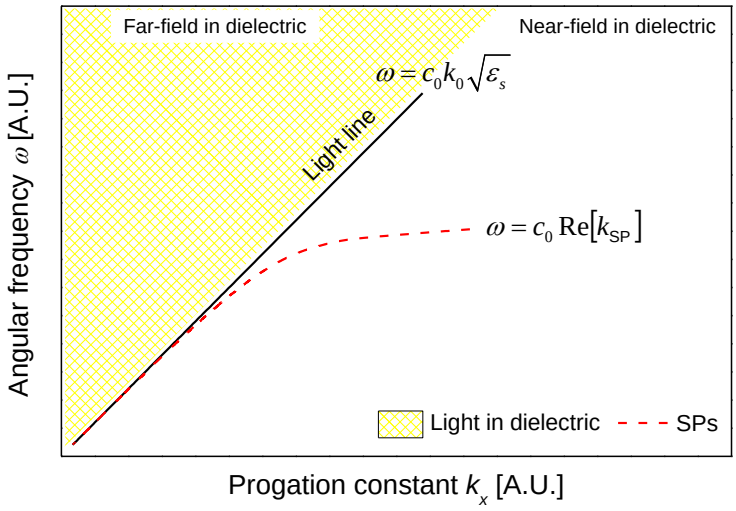

Figure 7 Dispersion relations of the light propagating in a dielectric (black solid) and SPs propagating along the interface between a dielectric and metal (red dashed).

1.1.4.1. Prism coupling

In prism coupling using Kretschmann configuration of ATR method, a metallic film is attached to the base of a prism with the refractive index n_p (see Figure 8a). Light at a wavelength λ reflects at the base of the prism at an angle θ. Let us note that the refractive index of the prism n_p is higher than that of a dielectric n_s. At the angle $\theta > \theta_c = \arcsin(n_s/n_p)$, the evanescent wave is generated by the totally reflected light at the prism-metal interface with a parallel component of propagation constant k^p_x:

$$k_x^p \equiv k_0 n_p \cdot \sin\theta. \tag{8}$$

As shown in Figure 8b, by varying the angle θ, the evanescent wave penetrating through the metallic film can be resonantly coupled with SPs at the lower refractive index dielectric interface if the phase matching condition is fulfilled:

$$k_x^p = \mathrm{Re}\left[k_{SP}\right]. \tag{9}$$

The resonant excitation of SPs is referred to as surface plasmon resonance (SPR) and is manifested as a decrease in the reflectivity as a function of the angle of incidence θ_{SPR} and wavelength λ_{SPR}.

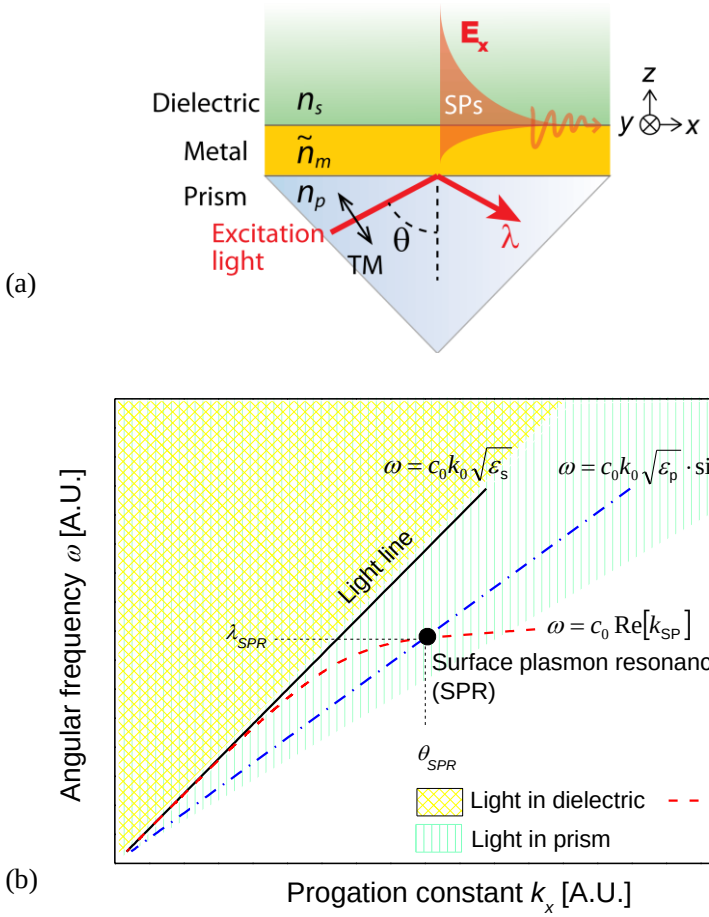

Figure 8 (a) Schematic of Kretschmann configuration of ATR method for the resonant excitation of SPs. (b) Dispersion relations of the light propagating in a dielectric (black solid), the light propagating in the prism at the angle of incidence $\theta=\theta_c$ (green dot), the light propagating in the prism and near field in a dielectric (blue dashed dot), and SPs propagating along the interface between a dielectric and metal (red dashed).

1.1.4.2. Grating coupling

In a diffraction grating based coupler, a metallic surface that is periodically corrugated with a period Λ is employed (See Figure 9a). When a light is incident from a dielectric with the refractive index n_s to the surface, diffraction occurs. This diffraction provides additional momentum to the parallel component of propagation constant of the light:

$$k_0 n_s \sin\theta + mG \quad (m = 0, \pm 1, \pm 2...), \tag{10}$$

where θ is an angle of incidence, m is an integer corresponding to the diffraction order of the light and $G=|\boldsymbol{G}|=2\pi/\Lambda$ is an absolute value of the grating vector. The light can be resonantly coupled with SPs at the dielectric-metal interface if the parallel component of propagation constant of the light and the propagation constant of SPs are matched:

$$k_0 n_s \sin\theta + mG = \mathrm{Re}\left[k_{\mathrm{SP}}\right] \tag{11}$$

In Figure 9b, the dispersion relation of SP coupled with a light propagating in the dielectric via m=0, ±1 and ±2 order is presented. Let us note that the coupling strength depends on the modulation depth and shape. In addition, the diffraction efficiency tends to drop drastically as increasing m, and thus practically m=±1 is dominant for the excitation of SPs.

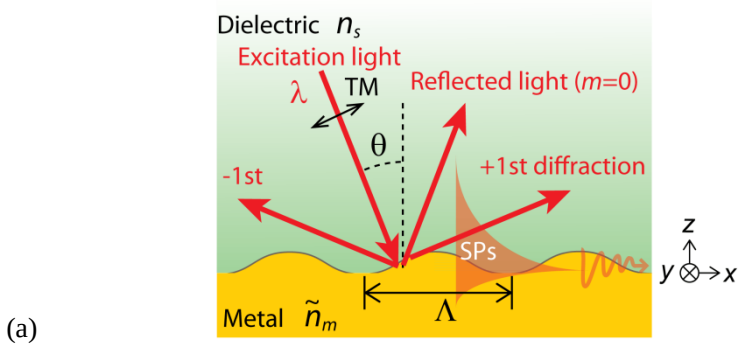

(a)

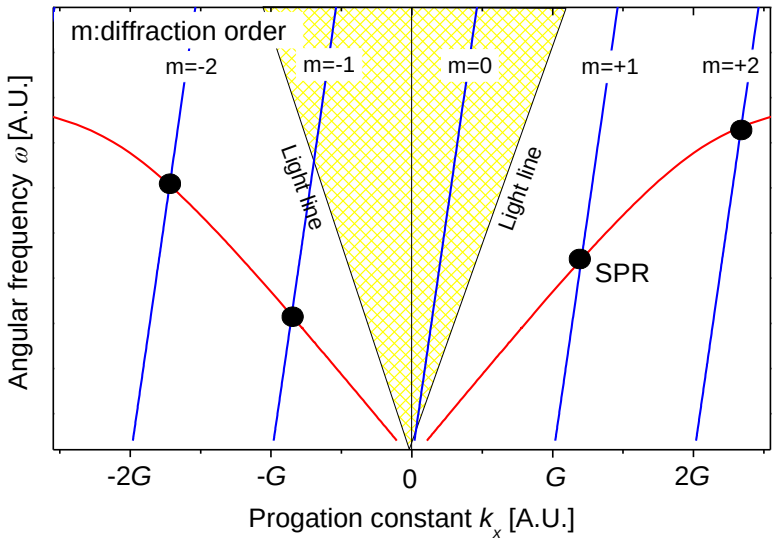

(b)

Figure 9 (a) Schematic of grating coupling for the excitation of surface plasmons. (b) The dispersion relations for SPs (red solid) and the diffracted light (blue solid, m=0,±1 and ±2). SPR occurs at each black point in the figure.

1.1.5. Fluorescence near interfaces

A randomly oriented fluorophore in a free space emits fluorescence light isotropically. However such an emission distribution is changed when it is close to a surface between two media. Here let us consider a fluorophore in a dielectric with the refractive index n_s is placed at a distance d_F from a dielectric with the refractive index n_p (n_p>n_s) (see Figure 10a). Contrary to that in a free space, the fluorophore at the surface emits a majority of fluorescence light into the dielectric with the higher refractive index n_p and angular distribution of emitted light is changed (see in Figure 10b) [44]. For instance at the distance d_F=20 nm, about 65 % of total emitted fluorescence intensity is into a glass substrate ($0<\theta<90$ deg and $0\leq\phi\leq360$ deg in Figure 10b). The maximum fluorescence intensity appears above the critical angle θ_c. This phenomenon is called supercritical angle emission (SAF). For a randomly oriented dipole, it gives rise to the emission distribution directional in polar direction θ and homogeneous in azimuth direction ϕ.

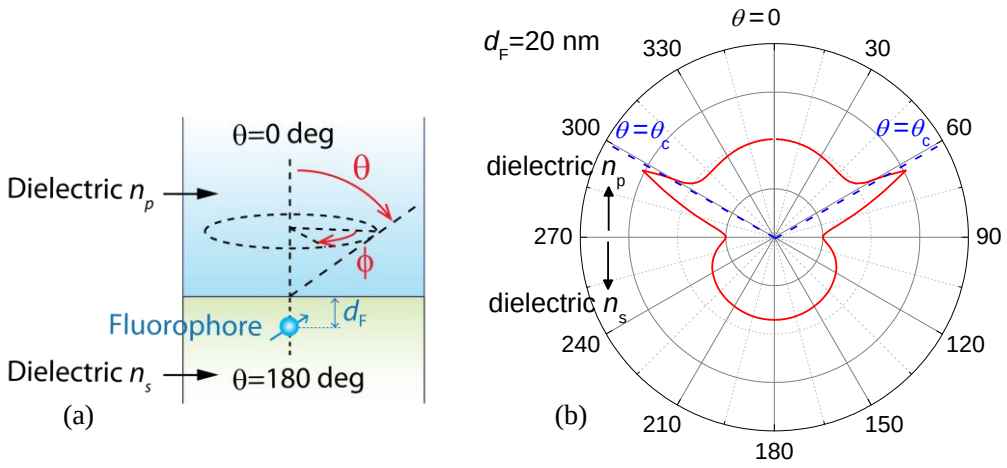

Figure 10 (a) Definition of coordinate system. (b) Simulated fluorescence intensity distribution in polar direction θ emitted from a fluorophore at distance d_F=20 nm at the wavelength λ=670 nm. The refractive indices of dielectrics are n_p=1.515 and n_s=1.331, respectively.

Now let us consider that a metallic film with the refractive index n_m and thickness t_m is between the two dielectrics. A randomly oriented fluorophore is in the dielectric of the refractive index n_s and located at a distance d_F from the metallic surface (see Figure 14a). As the distance d_F is as small as a penetration depth of SPs (L^s_{pen} in section 1.1.1), new transition channels are opened between the energy ground state S_0 and excited state S_1 as shown in the Jablonski diagram in

Figure 11b.

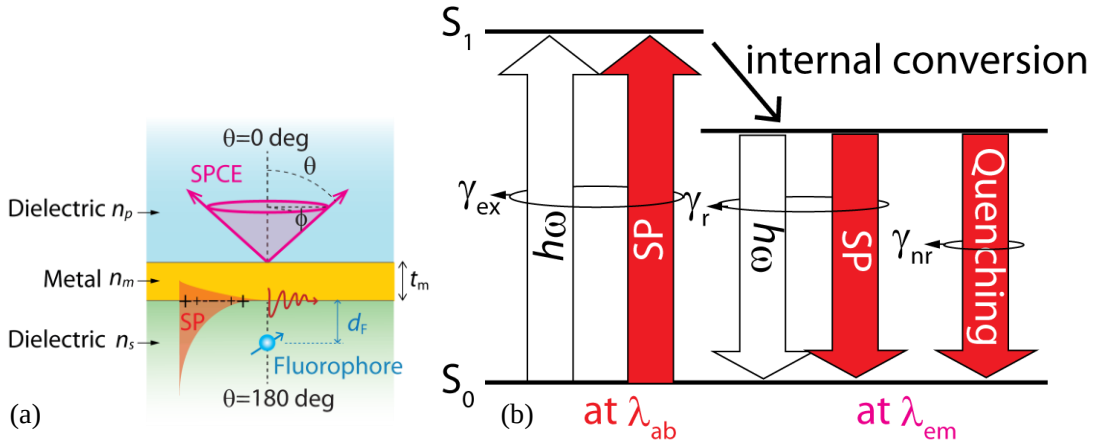

Figure 11 (a) Definition of coordinate system. (b) Jablonski diagram depicting the energy transition of a fluorophore in a free space (black arrow) and additional energy decay channels due to the presence of a metal (red arrow).

The fluorophore-metal interaction strongly depends on the distance d_F and it alters the fluorescence excitation rate γ_{ex}, ratiative decay rate γ_r and non-radiative decay rate γ_{nr}. When SPs are resonantly excited on a metallic surface at a wavelength that matches to a fluorophore absorption wavelength λ_{ab}, the plasmon-enhanced electric field intensity increases the excitation rate γ_{ex}. The excitation rate γ_{ex} can be expressed as a following function of the electric field vector $\boldsymbol{E}$ and the fluorophore absorption dipole moment $\boldsymbol{\mu}_{ab}$:

$$\gamma_{ex} \propto \left|\mathbf{E}(\lambda_{ab})\cdot\boldsymbol{\mu}_{ab}\right|. \tag{12}$$

From the excited state S_1, a fluorophore returns to its ground state S_0 either by emitting a photon propagating in a free-space or SPs (radiative decay rate $\gamma_r = \gamma_r^{free} + \gamma_r^{SP}$) at a wavelength that is higher than the excitation wavelength $\lambda_{em} > \lambda_{ab}$ (known as Stokes shift) or by non-radiative transitions (non-radiative decay rate γ_{nr}). The ratio $\eta = \gamma_r/(\gamma_r+\gamma_{nr})$ defines a fluorophore quantum yield. As shown in Figure 12, at distances d_F<15-20 nm, quenching of fluorescence due to Förster energy transfer leads to the enhanced non-radiative decay rate γ_{nr}, shorten lifetime $\tau = (\gamma_r + \gamma_{nr})^{-1}$ of the fluorophore at excited state S_1 and decreased quantum yield η (see Figure 13). At larger distance d_F that is smaller than the penetration depth of SPs L^s_{pen}, the emission via SPs becomes dominant which is accompanied with an enhanced radiative rate γ_r and can lead to

increased fluorophore quantum yield η.

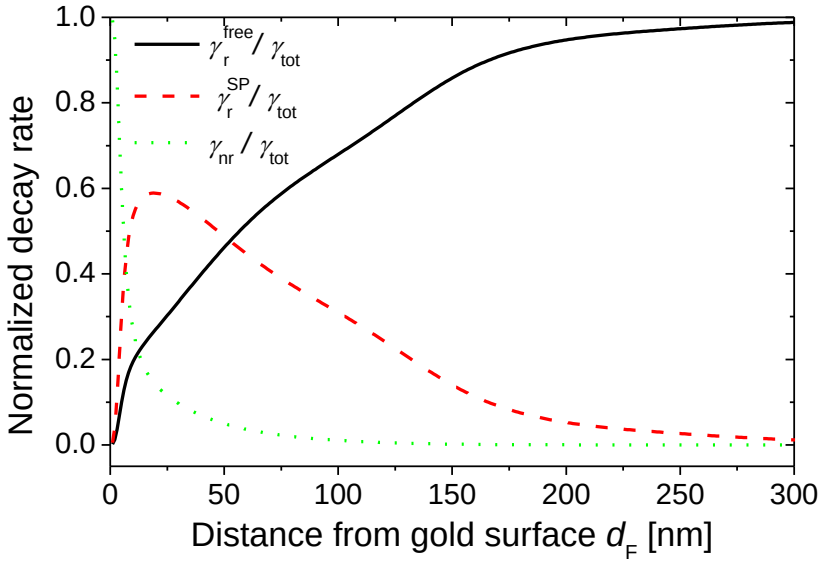

.

Figure 12 Normalized decay rate dependence of a randomly oriented dipole on its distance from a gold film d_F. Decay rates are optical waves propagating into free space γ_r^{free}, surface plasmons (SPCE) γ_r^{SP} and quenching γ_{nr}.

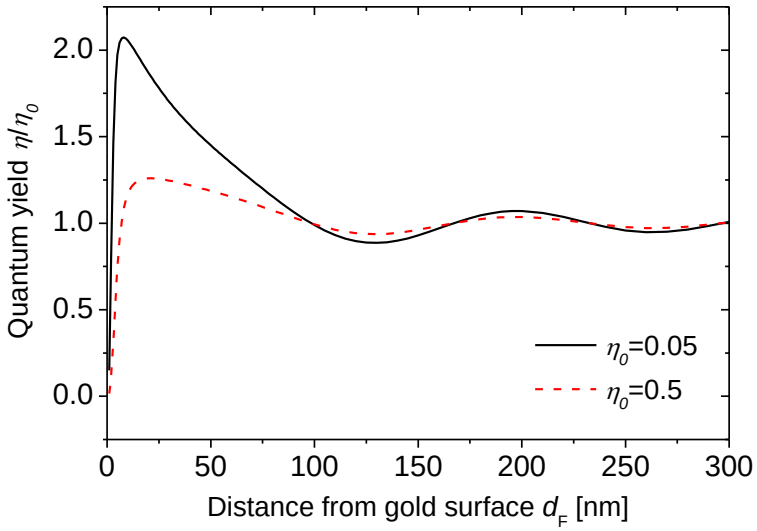

Figure 13 Obtained changes in the quantum yield η/η_0 for a model fluorophore with low (η_0=0.05) and high (η_0=0.5) intrinsic quantum yield far from the metal.

Fluorescence emission rate γ_{em} is proportional to the product of excitation rate γ_{ex} and quantum yield η as:

$$\gamma_{em} \propto \gamma_{ex} \frac{\gamma_r}{\gamma_r + \gamma_{nr}}, \tag{13}$$

which represents that the strong electric field intensity and high quantum yield lead high fluorescence light intensity.

Fluorescence light trapped via SPs can be converted to far-field radiation in a substrate with the refractive index n_p by using the coupling schemes. It is called surface plasmon-coupled emission (SPCE). For reverse Kretschmann configuration with a thin metallic film on a glass substrate, SPCE is directional in polar angle θ and homogeneous in azimuth angle ϕ, resulting in a characteristic cone shape in its emission pattern. The emission angle θ is a SPR angle at the emission wavelength of a fluorophore defined by equation (9). Theoretical and experimental studies showed that the total amount of fluorescence photons collected through the prism with the metallic film (SPCE) and without the metallic film (SAF) are similar or lower for randomly oriented dyes with quantum yield η>0.1 [45, 46]. However, through the higher directionality the SPCE approach offers means for better separation of the fluorescence signal from the light contributing to the background and efficient collection of the signal (see Figure 14b). For example, at the distance d_F=20 nm, 54 % of total fluorescence light is emitted as SPCE in the polar angle range 7.2 deg (=3×full width at half maximum of SPCE: 65.4≤θ≤72.6 deg and 0≤ϕ≤360 deg), while for SAF it was about 28 % in the polar angle range 38.6 deg (above θ_c: 61.5≤θ≤90 deg and 0≤ϕ≤360 deg).

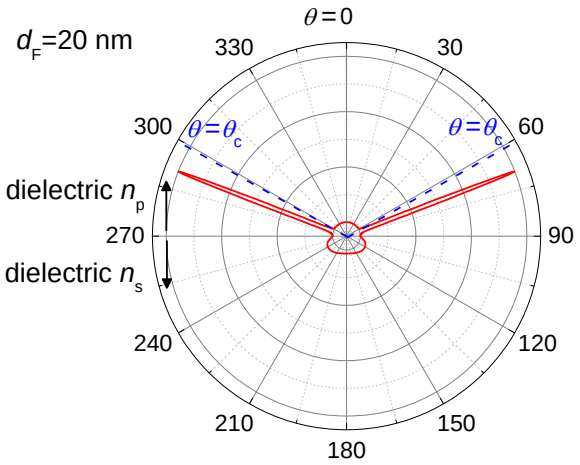

Figure 14 Simulated fluorescence intensity distribution in polar direction θ emitted from a fluorophore at the distance d_F=20 nm from a gold film (t_m=50 nm, n_m=0.118+3.92i) at the wavelength λ=670 nm. The refractive indices of dielectrics are n_p=1.515 and n_s=1.331, respectively.

1.2. State of the art fluorescence-based biosensors

In fluorescence-based biosensors, fluorophore-labeled molecules bound on the surface are excited by the light and emitted fluorescence light is detected. Key points determining the sensitivity of these biosensors are the ways of excitation and collection of fluorescence lights. In the simplest scheme, direct incidence of a laser or a white light excites randomly oriented fluorophores and isotropically emitted fluorescence light in a dielectric with the lower refractive index than a substrate is collected by a lens. As mentioned in section 1.1.5, for a glass substrate more than half of total emitted fluorescence light is in the substrate. Therefore the collection efficiency is very low. Here let us introduce the extensive efforts that have been devoted to improve the sensitivity in fluorescence-based biosensors by exploring the means of enhancing the excitation rate and collection efficiency of fluorescence light.

1.2.1. Enhancing excitation rate

The efforts have been focusing on increasing the local electric field intensity by employing total internal reflection, waveguide and plasmons. Total internal reflection fluorescence (TIRF) or bulk optical waveguide, evanescent waves generated by totally internally reflected light at the surface of bulk optical elements, e.g. prisms or glass slide with the higher refractive index than surroundings [47]. This field excites only fluorphores near the surface (a few hundred nanometer), which leads great suppression of background signal originating from bulk sample solution. It also brings a moderate enhancement of the electric field intensity. By using a bulk waveguide (microscope slide), the comparable sensitivity in the detection of viral, bacterial and protein analytes to ELISA was demonstrated [48]. Waveguides made of thin film (a few hundred nanometer thick) with the high refractive index contrast to the surroundings further increases electric field intensity enhancement. With respect to a low-refractive index contrast waveguide, the enhancement at the waveguide surface is more than an order of magnitude higher [49].

In plasmon enhanced fluorescence (PEF), various metallic structures are introduced. They support localized surface plasmons (LSPs) on nanoparticles [50, 51] or propagating surface plasmons (SPs) on planar metallic films [52]. They include arbitrary rough metallic surfaces, monodispersed metallic nanoparticles, metallic nanohole arrays and planar metallic film. Random metallic nanostructures are the simplest and generates LSPs by direct light incidence

[53-59]. It achieved about an order of magnitude improve of fluorescence intensity when compared to a bare glass substrate [54]. However since the structure is random, it is challenging to analytical and systematical description of electromagnetic field enhancement by LSPs. Chemically synthesized monodispersed metallic nanoparticles were employed in fluorescence-based biosensors [60, 61]. Their contribution to fluorescence intensity amplification was demonstrated with a model immunoassay experiment. In the experiments Cy5 dyes (η_0~0.28) labeled secondary IgG antibodies. The dyes were excited by LSPs on silver nanoparticles with the diameter of 150 nm deposited on a substrate [61]. Matching the dipole resonance of LSPs spectra to absorption wavelength of the dye allowed efficient excitation of dyes and up to 37-fold increase in fluorescence light intensity compared to a substrate in absence of the particles. Metallic nanohole arrays exhibiting extraordinary optical transmission by SPs attracted an attention in fluorescence-based biosensors, recently [62, 63]. These structures are prepared by focused ion beam (FIB) milling or electron-beam lithography (EBL) which does not allow direct preparation of large area. The nanohole arrays showed considerable potential for the enhancement of fluorescence intensity. Their performance was examined in experiment with Boron-dipyrromethene (BODIPY) dyes (η_0~0.9). The dyes were deposited on the array surface and their fluorescence intensity was increased about 11-fold relative to a silver film without the arrays. Since the quantum efficiency of BODIPY is close to 1, the fluorescence intensity enhancement was mostly attributed to the electric field intensity enhancement [62]. Planar metallic films are adopted to support SPs and referred to as surface plasmon-enhanced fluorescence spectroscopy (SPFS) [52, 64]. In a model experiment with biotin-labeled fluorescence latex particles that are bound to streptavidin on the surface of 50 nm thick gold film, the fluorescence intensity enhances by a factor of 15 [64].

1.2.2. Improving collection efficiency of fluorescence light

The main approaches to enhance the collection efficiency of fluorescence light are beaming or controlling the direction of emitted fluorescence light. Thus it has been in great interest to utilize phenomenon accompanied with directional emission including supercritical angle emission (SAF) and surface plasmon-coupled emission (SPCE) [65].

In biosensors implementing SAF, various optical elements such as parabolic elements [66-70] and diffractive optical elements [71] were proposed for efficient collection of SAF. With

parabolic optical elements, SAF is reflected at the side walls of the element and collimated which is eventually focused at a detector by additional lenses. A comparable sensitivity for the detection of interleukin 2 (IL-2) to ELISA was demonstrated [70].

In biosensors implementing SPCE, the major detection schemes are reverse Kretschmann configuration with bulk hemispherical prisms where SPCE is collected by an optical fiber [65, 72-74]. It is a simple setup and suited to trace the peak intensity of SPCE. However this way collects only a fragment of SPCE. Aiming at collecting all SPCE, dielectric paraboloid elements [75, 76] were proposed similarly to SAF. In addition to directionality of SPCE, selective emission is a great advantage. Since only fluorophores in the range of penetration depth of SPs L^{s}_{pen} from a metallic surface emit SPCE, its intensity is not attenuated even in highly optically dense media, e.g. serum or blood. In such an environment isotropically emitted fluorescence light is unable to be detected anymore. This powerful property has been demonstrated by the detection of a cardiac marker myglobin or in a model immunoassay experiments [72, 77-79]. SPCE signal decreases only two or three-fold in serum and hemoglobin solution with respect to that in buffer solution, while isotropically emitted fluorescence light decreases to undetectable level. The attenuated SPCE signal was, still, allowed to detect better than the required in clinical analysis 90 ng/mL for myglobin detection.

References

1. R. Molidor, A. Sturn, M. Maurer, and Z. Trajanoski, "New trends in bioinformatics: from genome sequence to personalized medicine," Experimental gerontology **38**, 1031-1036 (2003).
2. J. D. Wulfkuhle, L. A. Liotta, and E. F. Petricoin, "Proteomic applications for the early detection of cancer," Nature reviews cancer **3**, 267-275 (2003).
3. S. E. Ilyin, S. M. Belkowski, and C. R. Plata-Salam ̄ɾ。n, "Biomarker discovery and validation: technologies and integrative approaches," TRENDS in Biotechnology **22**, 411-416 (2004).
4. J. H. T. Luong, K. B. Male, and J. D. Glennon, "Biosensor technology: Technology push versus market pull," Biotechnology Advances **26**, 492-500 (2008).
5. R. M. Lequin, "Enzyme immunoassay (EIA)/enzyme-linked immunosorbent assay (ELISA)," Clinical Chemistry **51**, 2415-2418 (2005).
6. P. P. Thompson and R. P. Kowalski, "A 13-year retrospective review of polymerase chain reaction testing for infectious agents from ocular samples," Ophthalmology (2011).
7. P. B. Luppa, C. Müller, A. Schlichtiger, and H. Schlebusch, "Point-of-care testing (POCT): Current techniques and future perspectives," TrAC Trends in Analytical Chemistry (2011).
8. E. Aguilera-Herrador, M. Cruz-Vera, and M. Valcárcel "Analytical connotations of point-of-care testing," Analyst **135**, 2220-2232 (2010).
9. L. C. Clark and C. Lyons, "ELECTRODE SYSTEMS FOR CONTINUOUS MONITORING IN CARDIOVASCULAR SURGERY," Annals of the New York Academy of Sciences **102**, 29-45 (1962).
10. A. Numnuam, K. Y. Chumbimuni-Torres, Y. Xiang, R. Bash, P. Thavarungkul, P. Kanatharana, E. Pretsch, J. Wang, and E. Bakker, "Potentiometric Detection of DNA Hybridization," Journal of the American Chemical Society **130**, 410-411 (2007).
11. E. I. Rainina, E. N. Efremenco, S. D. Varfolomeyev, A. L. Simonian, and J. R. Wild, "The development of a new biosensor based on recombinant E. coli for the direct detection of organophosphorus neurotoxins," Biosensors and Bioelectronics **11**, 991-1000 (1996).
12. S. Hrapovic, Y. L. Liu, K. B. Male, and J. H. T. Luong, "Electrochemical biosensing platforms using platinum nanoparticles and carbon nanotubes," Analytical Chemistry **76**, 1083-1088 (2004).
13. Y. H. Lin, F. Lu, Y. Tu, and Z. F. Ren, "Glucose biosensors based on carbon nanotube nanoelectrode ensembles," Nano Letters **4**, 191-195 (2004).
14. Y. Liu, Z. H. Qin, X. F. Wu, and H. Jiang, "Immune-biosensor for aflatoxin B(1) based bio-electrocatalytic reaction on micro-comb electrode," Biochemical Engineering Journal **32**, 211-217 (2006).
15. H. C. Tsai, R. A. Doong, H. C. Chiang, and K. T. Chen, "Sol-gel derived urease-based optical biosensor for the rapid determination of heavy metals," Analytica Chimica Acta **481**, 75-84

(2003).

16. T. Endo, K. Kerman, N. Nagatani, Y. Takamura, and E. Tamiya, "Label-free detection of peptide nucleic acid-DNA hybridization using localized surface plasmon resonance based optical biosensor," Analytical Chemistry **77**, 6976-6984 (2005).
17. N. Nath and A. Chilkoti, "A colorimetric gold nanoparticle sensor to interrogate biomolecular interactions in real time on a surface," Analytical Chemistry **74**, 504-509 (2002).
18. Y. Fu, J. Zhang, and J. R. Lakowicz, "Plasmon-Enhanced Fluorescence from Single Fluorophores End-Linked to Gold Nanorods," Journal of the American Chemical Society **132**, 5540-5541 (2010).
19. Y. Wang, A. Brunsen, U. Jonas, J. Dostalek, and W. Knoll, "Prostate Specific Antigen Biosensor Based on Long Range Surface Plasmon-Enhanced Fluorescence Spectroscopy and Dextran Hydrogel Binding Matrix," Analytical Chemistry **81**, 9625-9632 (2009).
20. J. Zhang, H. L. Qi, Y. Li, J. Yang, Q. Gao, and C. X. Zhang, "Electrogenerated chemiluminescence DNA biosensor based on hairpin DNA probe labeled with ruthenium complex," Analytical Chemistry **80**, 2888-2894 (2008).
21. S. S. Zhang, H. Zhong, and C. F. Ding, "Ultrasensitive flow injection chemiluminescence detection of DNA hybridization using signal DNA probe modified with Au and CuS nanoparticles," Analytical Chemistry **80**, 7206-7212 (2008).
22. V. Hana, Z. Alice, L. Markéta, Josef, Sbreve, ebreve, pánek, K. árka, L. Radek, R. Dominik, R. Ivan, Ji, rbreve, and H. í, "Investigating oligonucleotide hybridization at subnanomolar level by surface plasmon resonance biosensor method," Biopolymers **82**, 394-398 (2006).
23. Y. Wang, C.-J. Huang, U. Jonas, T. Wei, J. Dostalek, and W. Knoll, "Biosensor based on hydrogel optical waveguide spectroscopy," Biosensors and Bioelectronics **25**, 1663-1668 (2010).
24. K. A. Marx, "Quartz crystal microbalance: A useful tool for studying thin polymer films and complex biomolecular systems at the solution-surface interface," Biomacromolecules **4**, 1099-1120 (2003).
25. C. K. O'Sullivan and G. G. Guilbault, "Commercial quartz crystal microbalances - theory and applications," Biosensors & Bioelectronics **14**, 663-670 (1999).
26. R. Roy, S. Hohng, and T. Ha, "A practical guide to single-molecule FRET," Nature Methods **5**, 507-516 (2008).
27. J. Eid, A. Fehr, J. Gray, K. Luong, J. Lyle, G. Otto, P. Peluso, D. Rank, P. Baybayan, and B. Bettman, "Real-time DNA sequencing from single polymerase molecules," Science **323**, 133-138 (2009).
28. W. Knoll, "Interfaces and thin films as seen by bound electromagnetic waves," Annual Review of Physical Chemistry **49**, 569-638 (1998).
29. D. Sarid, "Long-Range Surface-Plasma Waves on Very Thin Metal Films," Physical Review

Letters **47**, 1927 (1981).

30. J. Dostalek and W. Knoll, "Biosensors based on surface plasmon-enhanced fluorescence spectroscopy," Biointerphases **3**, Fd12-Fd22 (2008).
31. W. L. Barnes, T. W. Preist, S. C. Kitson, and J. R. Sambles, "Physical origin of photonic energy gaps in the propagation of surface plasmons on gratings," Physical Review B **54**, 6227 (1996).
32. W. L. Barnes, T. W. Preist, S. C. Kitson, J. R. Sambles, N. P. K. Cotter, and D. J. Nash, "Photonic gaps in the dispersion of surface plasmons on gratings," Physical Review B **51**, 11164 (1995).
33. X. I. Saldana and G. G. de la Cruz, "Electromagnetic surface waves in semi-infinite superlattices," J. Opt. Soc. Am. A **8**, 36-40 (1991).
34. W. M. Robertson, "Experimental measurement of the effect of termination on surface electromagnetic waves in one-dimensional photonic bandgap arrays," Journal of lightwave technology **17**, 2013-2017 (1999).
35. W. M. Robertson and M. S. May, "Surface electromagnetic wave excitation on one-dimensional photonic band-gap arrays," Applied Physics Letters **74**, 1800-1800 (1999).
36. J. A. Gaspar-Armenta and F. Villa, "Band-structure properties of one-dimensional photonic crystals under the formalism of equivalent systems," J. Opt. Soc. Am. B **21**, 405-412 (2004).
37. Y. Guo, C. Divin, A. Myc, F. L. Terry, J. R. Baker, T. B. Norris, and J. Y. Ye, "Sensitive molecular binding assay using a photonic crystal structure in total internal reflection," Optics Express **16**, 11741-11749 (2008).
38. Y. Guo, J. Y. Ye, C. Divin, B. Huang, T. P. Thomas, J. R. Baker, and T. B. Norris, "Real-time biomolecular binding detection using a sensitive photonic crystal biosensor," Analytical Chemistry **82**, 5211-5218 (2010).
39. V. N. Konopsky and E. V. Alieva, "Photonic crystal surface waves for optical biosensors," Analytical Chemistry **79**, 4729-4735 (2007).
40. M. Shinn and W. M. Robertson, "Surface plasmon-like sensor based on surface electromagnetic waves in a photonic band-gap material," Sensors and Actuators B: Chemical **105**, 360-364 (2005).
41. P. Yeh, A. Yariv, and C.-S. Hong, "Electromagnetic propagation in periodic stratified media. I. General theory," J. Opt. Soc. Am. **67**, 423-438 (1977).
42. H. Raether, *Surface plasmons on smooth and rough surfaces and on gratings*, Springer Tracts in Modern Physics (Springer-Verlag Berlin, 1988).
43. J. Homola, "Surface plasmon resonance sensors for detection of chemical and biological species," Chemical Reviews **108**, 462-493 (2008).
44. E. H. Hellen and D. Axelrod, "Fluorescence emission at dielectric and metal-film interfaces," J. Opt. Soc. Am. B **4**, 337-350 (1987).
45. J. Enderlein and T. Ruckstuhl, "The efficiency of surface-plasmon coupled emission for sensitive

fluorescence detection," Optics Express **13**, 8855-8865 (2005).

46. M. Trnavsky, J. Enderlein, T. Ruckstuhl, C. McDonagh, and B. D. MacCraith, "Experimental and theoretical evaluation of surface plasmon-coupled emission for sensitive fluorescence detection," J. Biomed. Opt. **13**(2008).
47. C. R. Taitt, G. P. Anderson, and F. S. Ligler, "Evanescent wave fluorescence biosensors," Biosensors and Bioelectronics **20**, 2470-2487 (2005).
48. C. A. Rowe, M. Leonard, M. J. Feldstein, J. P. Golden, S. B. Scruggs, B. D. MacCraith, J. John, and F. S. Ligler, "Array biosensor for simultaneous identification of bacterial, viral, and protein analytes," Analytical Chemistry **71**, 3846-3852 (1999).
49. H. Mukundan, A. S. Anderson, W. K. Grace, K. M. Grace, N. Hartman, J. S. Martinez, and B. I. Swanson, "Waveguide-based biosensors for pathogen detection," Sensors **9**, 5783-5809 (2009).
50. A. M. Kern and O. J. F. Martin, "Excitation and Reemission of Molecules near Realistic Plasmonic Nanostructures," Nano Letters **11**, 482-487 (2011).
51. A. Kinkhabwala, Z. Yu, S. Fan, Y. Avlasevich, K. M llen, and W. E. Moerner, "Large single-molecule fluorescence enhancements produced by a bowtie nanoantenna," Nature Photonics **3**, 654-657 (2009).
52. J. W. Attridge, P. B. Daniels, J. K. Deacon, G. A. Robinson, and G. P. Davidson, "Sensitivity enhancement of optical immunosensors by the use of a surface plasmon resonance fluoroimmunoassay," Biosensors and Bioelectronics **6**, 201-214 (1991).
53. A. Renier, T. Mangeat, H. Benalia, C. Elie-Caille, C. Pieralli, and B. Wacogne, "Gold/silica thin film for biosensors applications: Metal enhanced fluorescence," Laser Physics **20**, 591-595 (2010).
54. E. G. Matveeva, I. Gryczynski, A. Barnett, Z. Leonenko, J. R. Lakowicz, and Z. Gryczynski, "Metal particle-enhanced fluorescent immunoassays on metal mirrors," Analytical Biochemistry **363**, 239-245 (2007).
55. R. Aroca, G. J. Kovacs, C. A. Jennings, R. O. Loutfy, and P. S. Vincett, "Fluorescence enhancement from Langmuir-Blodgett monolayers on silver island films," Langmuir **4**, 518-521 (1988).
56. K. Aslan, Z. Leonenko, J. R. Lakowicz, and C. D. Geddes, "Annealed silver-island films for applications in metal-enhanced fluorescence: Interpretation in terms of radiating plasmons," Journal of Fluorescence **15**, 643-654 (2005).
57. E. Matveeva, Z. Gryczynski, J. Malicka, I. Gryczynski, and J. R. Lakowicz, "Metal-enhanced fluorescence immunoassays using total internal reflection and silver island-coated surfaces," Analytical Biochemistry **334**, 303-311 (2004).
58. K. Ray, M. H. Chowdhury, and J. R. Lakowicz, "Aluminum Nanostructured Films as Substrates for Enhanced Fluorescence in the Ultraviolet-Blue Spectral Region," Analytical Chemistry **79**,

6480-6487 (2007).

59. M. T. Zin, K. Leong, N. Y. Wong, H. Ma, M. Sarikaya, and A. K. Y. Jen, "Surface-plasmon-enhanced fluorescence from periodic quantum dot arrays through distance control using biomolecular linkers," Nanotechnology **20**, 015305 (2009).
60. X. Wei, H. Li, Z. Li, M. Vuki, Y. Fan, W. Zhong, and D. Xu, "Metal-enhanced fluorescent probes based on silver nanoparticles and its application in IgE detection," Analytical and Bioanalytical Chemistry, 1-7 (2012).
61. R. Nooney, A. Clifford, X. LeGuevel, O. Stranik, C. McDonagh, and B. D. MacCraith, "Enhancing the analytical performance of immunoassays that employ metal-enhanced fluorescence," Analytical and Bioanalytical Chemistry **396**, 1127-1134 (2010).
62. P.-F. Guo, S. Wu, Q.-J. Ren, J. Lu, Z. Chen, S.-J. Xiao, and Y.-Y. Zhu, "Fluorescence Enhancement by Surface Plasmon Polaritons on Metallic Nanohole Arrays," The Journal of Physical Chemistry Letters **1**, 315-318 (2010).
63. H. Im, S. H. Lee, N. J. Wittenberg, T. W. Johnson, N. C. Lindquist, P. Nagpal, D. J. Norris, and S. H. Oh, "Template-Stripped Smooth Ag Nanohole Arrays with Silica Shells for Surface Plasmon Resonance Biosensing," ACS nano (2011).
64. T. Liebermann and W. Knoll, "Surface-plasmon field-enhanced fluorescence spectroscopy," Colloids and Surfaces a-Physicochemical and Engineering Aspects **171**, 115-130 (2000).
65. J. R. Lakowicz, J. Malicka, I. Gryczynski, and Z. Gryczynski, "Directional surface plasmon-coupled emission: a new method for high sensitivity detection," Biochemical and biophysical research communications **307**, 435-439 (2003).
66. T. Ruckstuhl, M. Rankl, and S. Seeger, "Highly sensitive biosensing using a supercritical angle fluorescence (SAF) instrument," Biosensors and Bioelectronics **18**, 1193-1199 (2003).
67. D. Hill, B. McDonnell, S. Hearty, L. Basabe-Desmonts, R. Blue, M. Trnavsky, C. McAtamney, R. O'Kennedy, and B. D. MacCraith, "Novel disposable biochip platform employing supercritical angle fluorescence for enhanced fluorescence collection," Biomedical Microdevices, 1-9 (2011).
68. D. Kurzbuch, J. Bakker, J. Melin, C. J テカ nsson, T. Ruckstuhl, and B. D. MacCraith, "A biochip reader using super critical angle fluorescence," Sensors and Actuators B: Chemical **137**, 1-6 (2009).
69. H. Välimäki and K. Tappura, "A novel platform for highly surface-sensitive fluorescent measurements applying simultaneous total internal reflection excitation and super critical angle detection," Chemical Physics Letters **473**, 358-362 (2009).
70. T. Ruckstuhl, C. M. Winterflood, and S. Seeger, "Supercritical Angle Fluorescence Immunoassay Platform," Analytical Chemistry (2011).
71. P. Macko and M. P. Whelan, "Fabrication of holographic diffractive optical elements for enhancing light collection from fluorescence-based biochips," Optics Letters **33**, 2614-2616

(2008).

72. E. Matveeva, Z. Gryczynski, I. Gryczynski, and J. R. Lakowicz, "Immunoassays based on directional surface plasmon-coupled emission," Journal of Immunological Methods **286**, 133-140 (2004).
73. I. Gryczynski, J. Malicka, J. R. Lakowicz, E. M. Goldys, N. Calander, and Z. Gryczynski, "Directional two-photon induced surface plasmon-coupled emission," Thin Solid Films **491**, 173-176 (2005).
74. I. Gryczynski, J. Malicka, Z. Gryczynski, and J. R. Lakowicz, "Surface plasmon-coupled emission with gold films," Journal of Physical Chemistry B **108**, 12568-12574 (2004).
75. J. S. Yuk, M. Trnavsky, C. McDonagh, and B. D. MacCraith, "Surface plasmon-coupled emission (SPCE)-based immunoassay using a novel paraboloid array biochip," Biosensors & Bioelectronics **25**, 1344-1349 (2010).
76. J. S. Yuk, B. D. MacCraith, and C. McDonagh, "Signal enhancement of surface plasmon-coupled emission (SPCE) with the evanescent field of surface plasmons on a bimetallic paraboloid biochip," Biosensors & Bioelectronics **26**, 3213-3218 (2010).
77. E. G. Matveeva, I. Gryczynski, A. Barnett, N. Calander, and Z. Gryczynski, "Red blood cells do not attenuate the SPCE fluorescence in surface assays," Analytical and Bioanalytical Chemistry **388**, 1127-1135 (2007).
78. E. Matveeva, Z. Gryczynski, I. Gryczynski, J. Malicka, and J. R. Lakowicz, "Myoglobin immunoassay utilizing directional surface plasmon-coupled emission," Analytical Chemistry **76**, 6287-6292 (2004).
79. E. G. Matveeva, Z. Gryczynski, J. Malicka, J. Lukomska, S. Makowiec, K. W. Berndt, J. R. Lakowicz, and I. Gryczynski, "Directional surface plasmon-coupled emission: Application for an immunoassay in whole blood," Analytical Biochemistry **344**, 161-167 (2005).

2. RESEARCH OBJECTIVES

This thesis focuses on research in new plasmonic phenomena for the amplification of intensity from fluorescence assays and on their implementation to advanced biosensors for the detection of trace amounts of target molecular analytes. Particularly, we aim at development of metallic structures that simultaneously enable enhancing the excitation rate of fluorophore labels in close proximity to a sensor surface and beaming the fluorescence light towards the detector. The dependence of the polar and azimuth angular distribution of emitted fluorescence light is investigated by manipulating characteristics of surfaces plasmons. Rich spectrum of plasmon modes arising from their coupling across thin metallic film (sections 3.1) and from dense periodic metallic gratings is studied (section 3.2). The fluorescence excitation through the enhanced field of surface plasmon is applied for new biosensors for immunoassay-based detection of target analytes (section 3.3). In addition, the implementation of observed phenomena to a new compact biosensor chip is carried out. The chip takes advantages of combined amplification strategies relying on the enhanced excitation and directional emission. Its key biosensor characteristics are also determined (section 3.4).

3. RESEARCH OVERVIEW

3.1. Long range surface plasmon-coupled fluorescence emission for biosensor applications

In this project, surface plasmon-coupled emission (SPCE) of fluorophore labels dispersed in an extended three-dimensional hydrogel matrix via long range surface plasmons (LRSP) is experimentally and theoretically investigated. The reverse Kretschmann configuration is employed for the extraction of the fluorescence light collected by these types of surface plasmon modes (see Figure 15a). A layer structure supporting LRSPs that consists of a low refractive index fluoropolymer layer, a thin gold film and a large binding capacity N-isopropylacrylamide (NIPAAm)-based hydrogel matrix swollen in an aqueous sample is employed (see Figure 15b). A new setup for the measurement of angular distribution of fluorescence light was developed. A model based on Chance-Prock-Silbey model was also implemented for the simulations of fluorescence emission above a planar layer structure.

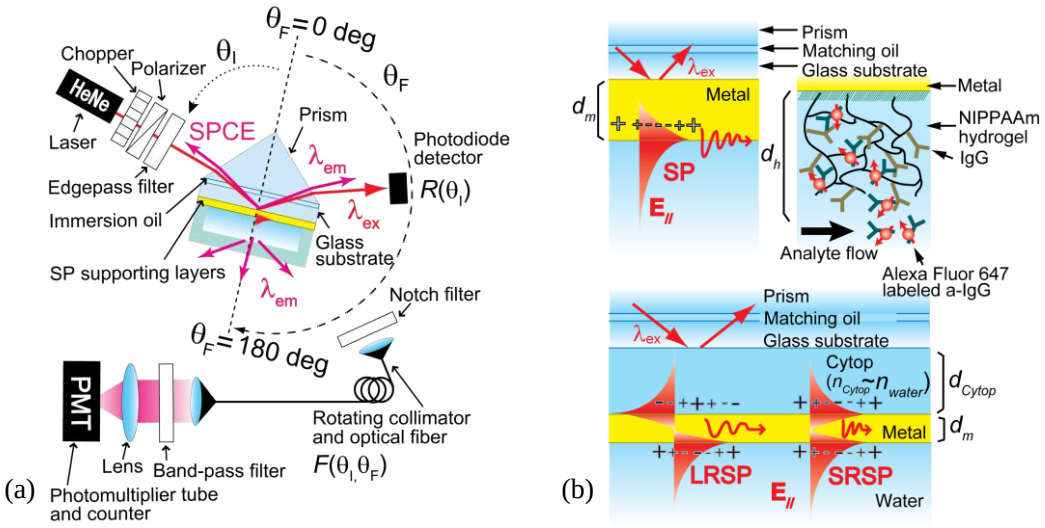

Figure 15 (a) Optical setup for the measurement of fluorescence $F(\theta_I, \theta_F)$ and reflectivity $R(\theta_I)$ angular spectra. (b) Layer architectures supporting regular SPs and LRSPs with a hydrogel binding matrix.

The obtained experimental data exhibited good agreement with simulations. Compared to regular surface plasmons, the results revealed the combined excitation and emission via LRSPs allowed increasing the peak fluorescence intensity with a factor of 4.4 and squeezing the emission in a cone with 6-fold narrower full width in half maximum (see Figure 16). The results indicate that probing the hydrogel interface by LRSPs and regular SPs leads to similar total fluorescence light intensity collected through the SPCE. However, the employment of LRSPs offers the advantage of the excitation and emission at lower angles which can simplify the implementation of this method to practical biosensor devices. In addition, the highly directional emission manifested as a narrow emission peak can be more efficiently filtered from the background signal and it can be useful for e.g. angular multiplexing of sensing channels.

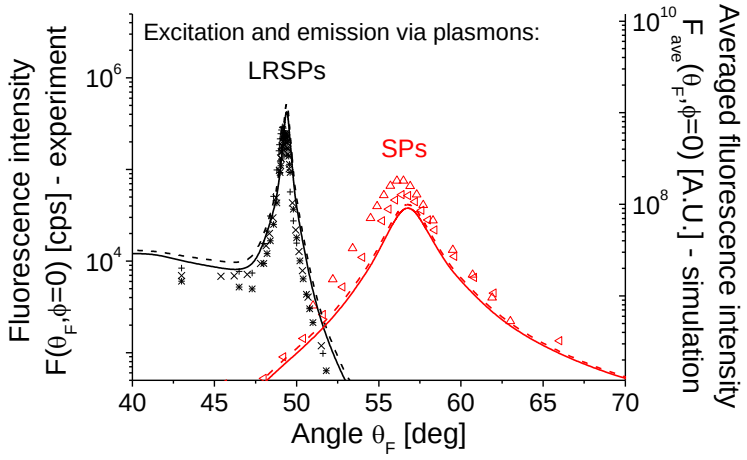

Figure 16 Experimental fluorescence intensity emitted via LRSP and SP modes for the excitation via LRSP and SP modes (θ_I=48.5 and θ_I=56.7 deg, respectively). In each experiment, three samples were measured (black symbols for LRSPs and red symbols for SPs) and compared to the simulations with the relative angles γ=0 and 45 deg (dashed and solid lines, respectively).

This work was published to peer-reviewed journal paper as:

K. Toma, J. Dostalek, and W. Knoll, "Long range surface plasmon-coupled fluorescence emission for biosensor applications," Optics Express **19**, 11090-11099 (2011).

Also selected in The Virtual Journal for Biomedical Optics **6**, 7 (2011).

3.2. Surface plasmon-coupled emission on plasmonic Bragg gratings

An alternative way to manipulate the dispersion relation of surface plasmons based on their diffraction coupling on dense sub-wavelength metallic gratings was studied (see Figure 17). This work shows that dense sub-wavelength plasmonic gratings allow controlling spatial distribution of surface plasmon-coupled emission (SPCE) into a dielectric substrate through surface plasmons propagating along a thin metal film. The dispersion relation of surface plasmons at upper and lower interfaces of a thin metallic film can be simply tuned by changing the refractive index at respective metallic interfaces. This manipulation of propagation constant of surface plasmons enables exploiting a rich spectrum of Bragg scattered and cross-coupled surface plasmon modes. These surface plasmon modes can serve as efficient fluorescence decay channels for emitters placed on the top of the metallic film. In particular, they can suppress or

enhance the fluorescence light intensity emitted to specific directions on or inside the characteristic SPCE emission cone (see Figure 18). These features can provide means for controlling the interaction of emitters with surface plasmons in areas including optical sources relying on nanoscale antennas and sensor utilizing surface plasmon-enhanced fluorescence spectroscopy. In particular, these observations may provide leads to advance plasmon-enhanced fluorescence sensors through more efficient collection of fluorescence light emitted via Bragg-scattered surface plasmons, simpler detection of SPCE signal emitted at smaller polar angles, and can be useful for multiplexing of sensing channels by emitting the fluorescence light from different sensing areas to different directions.

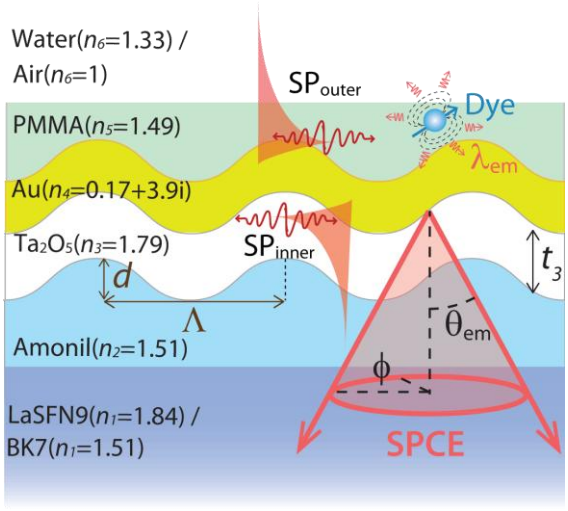

Figure 17 Diffraction grating supporting surface plasmons that serve as emission channels for DiD dyes dispersed in a PMMA layer. Refractive indices of layers at the wavelength λ_{em}=670 nm are shown for each layer.

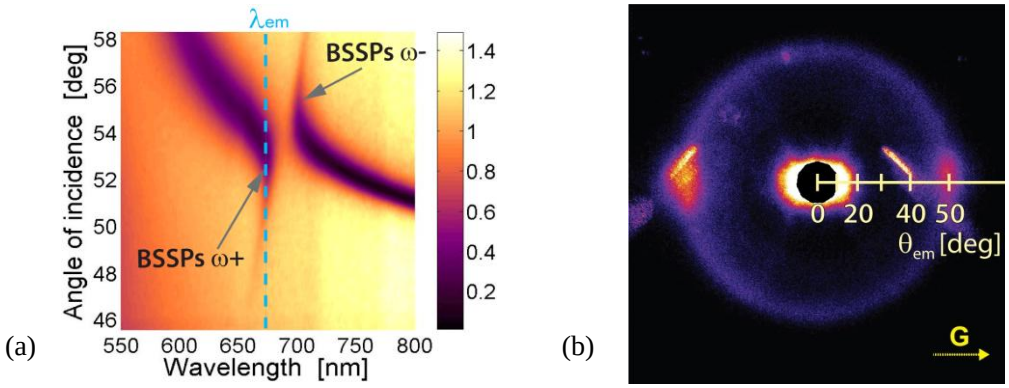

Figure 18 (a) Measured dispersion relation of and (b) bottom view of SPCE patterns of Bragg scattered surface plasmons on a Bragg grating structured metallic film. ***G*** indicates a grating vector.

This work was published to peer-reviewed journal paper as:

M. Toma*, **K. Toma***, P. Adam, J. Homola. Homola, W. Knoll, and J. Dostálek, "Surface plasmon-coupled emission on plasmonic Bragg gratings," Optics Express **20**, 14042-14053 (2012). *Authors equally contributed to this work.

3.3. Bloch surface wave-enhanced fluorescence biosensor

In this work, an alternative structure supporting surface waves with similar characteristics like surface plasmons is employed for the fluorescence amplification. It is a one dimensional photonic crystal (1DPC) composed of series of high (Si-rich) and low (N-rich) refractive index dielectric layers. 1DPC supports Bloch surface waves (BSWs) and of Bragg mirror (S1 and S2 in Figure 19, respectively). 1DPC was designed to amplify the fluorescence signal from fluorophore labels by the combination of enhancing excitation rate (though strong electric field intensity of resonantly excited BSW on S1) and shaping the angular distribution of emitted light towards a detector (by a Bragg mirror S2). As a result of the combination of BSWs supporting layers (S1) and Bragg mirror (S2), 1DPC was capable to amplify the fluorescence signal with respect to regular TIRF on a bare glass slide (see Figure 20). The theory predicts that this approach holds potential for increasing the sensitivity by more than two orders of magnitude. The model immunoassay experiments showed lower enhancement of limit of detection by a factor of 12.5, mainly due to the imperfection of prepared 1DPC.

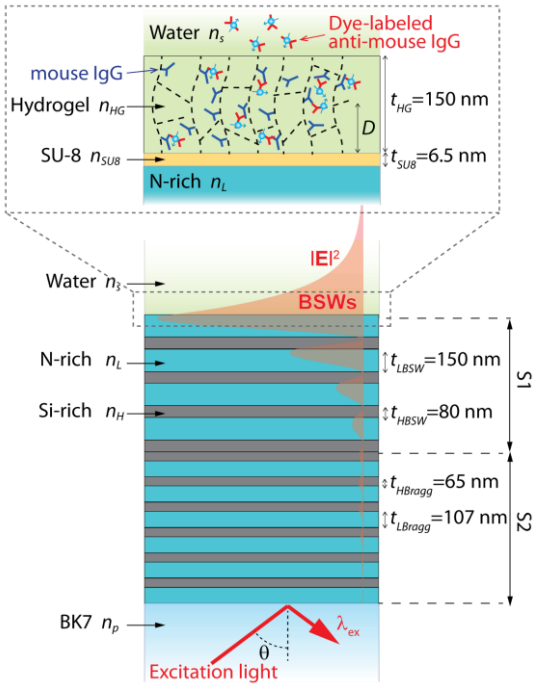

Figure 19 Designed layer structure of 1DPC composed of repetitive low (N-rich) and high (Si-rich) refractive index dielectric layers that support BSWs (S1) and Bragg mirror (S2).

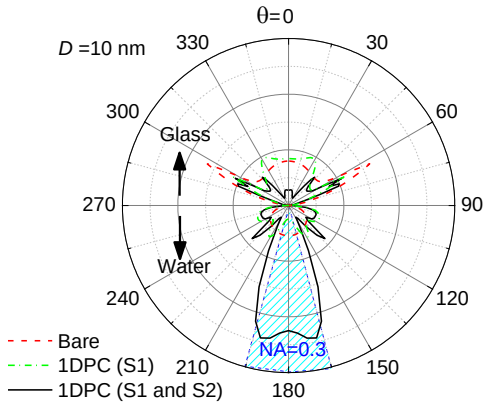

Figure 20 Simulated fluorescence light intensity distribution for 1DPC with (black solid) and without (green dash dot) Bragg mirror (S2) and a reference glass substrate (red dashed) emitted from randomly oriented dipole presented at the distance from a sensor surface *D*=10 nm.

This work is in preparation for the submission to peer-reviewed journal paper as:

K. Toma, M. Ballarini, E. Descrovi, W. Knoll and J. Dostalek, "Bloch surface wave-enhanced fluorescence biosensor", *in preparation*.

3.4. Compact biochip for surface plasmon-enhanced fluorescence assays

A new compact biochip implementing surface plasmon-enhanced fluorescence is developed. It takes advantage of fluorescence signal amplification relying on the coupling of fluorophore excitation and emission channels with confined and strongly enhanced field of surface plasmons on a metallic sensor surface. In order to excite and collect the fluorescence light emitted by fluorophore labels via surface plasmons, (reverse) Kretschmann configuration is combined with diffractive optical elements embedded on the chip surface (see Figure 21). These include a concentric relief grating for the imaging of highly directional surface plasmon-coupled emission light beam at the emission wavelength to a detector (see Figure 22). Additional linear grating is used to generate surface plasmons at the excitation wavelength on the sensor surface for the increase of fluorescence excitation rate. The reported approach offers the advantage of increased intensity of fluorescence signal, reduced background, and compatibility with nanoimprint lithography for cost-effective preparation of sensor chip. The potential of presented approach is demonstrated in a model immunoassay experiment in which the limit of detection of 11 pM is achieved.

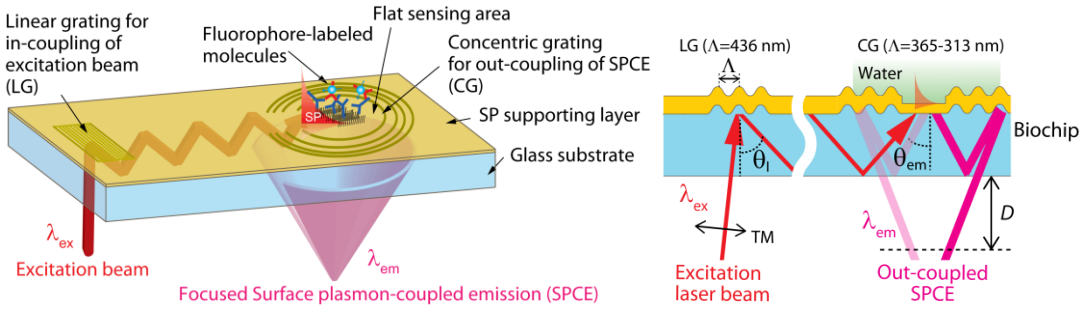

Figure 21 Schematic of biochip with diffractive optical elements for the in-coupling of the excitation beam (linear grating) to biochip and for the out-coupling and imaging of surface plasmon-coupled emission (SPCE) to a detector (concentric grating) (left) and its side view (right).

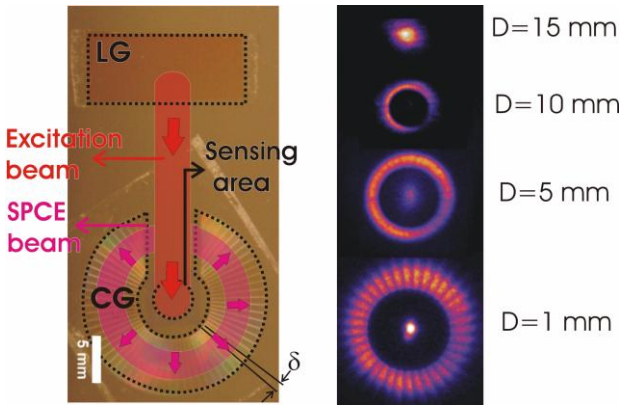

Figure 22 Top view of prepared biochip carrying LG and CG diffractive elements (left) and measured spatial distribution of SPCE cone out-coupled from the biochip by using CG element at increasing distance below the biochip *D*=1, 5, 10 and 15 mm.

This work was submitted to peer-reviewed journal paper and European patent as:

K. Toma, M. Vala, P. Adam, J. Homola, W. Knoll and J. Dostalek, "Compact Biochip for Surface Plasmon-Enhanced Fluorescence Assays", *submitted*.

J. Dostalek, **K. Toma**, M. Vala, P. Adam, J. Homola and W. Knoll, "COMPACT PLASMON-ENHANCED FLUORESCENCE BIOSENSOR", EP12168046.

4. CONCLUSIONS

In this thesis, plasmon-mediated fluorescence on metallic structures is experimentally and theoretically investigated and employed in advanced fluorescence-based biosensors. New observations of the interaction between fluorophores and surface plasmons with manipulated characteristics are presented and employed for fluorescence-based detection of molecular analytes. Novel optical schemes which exploit surface plasmon-enhanced fluorescence in miniaturized and potentially portable biosensor devices were carried out, the key biosensor characteristics were determined, and compared to those for other state-of-the-art devices.

In order to take advantage of directional emission in fluorescence-based assays, the coupling of fluorophores with metallic surfaces supporting long range surface plasmon and Bragg scattered surface plasmons was studied. The results show that these modes can efficiently collect fluorescence light emitted by fluorophore labels. Extraction of fluorescence light emitted via long range surface plasmons provides an extremely narrow polar angular distribution and enhanced peak intensity. In addition, with the reverse Kretschmann configuration, the emission occurs at lower angles compared to regular surface plasmon, which simplifies its delivery to a detector. Selective reducing or increasing the intensity of surface plasmon-coupled emission at certain azimuth angles was demonstrated by using metallic Bragg gratings. An alternative structure based on one-dimensional dielectric photonic crystal that supports Bloch surface waves were employed for the amplification of fluorescence-based assays. These modes exhibit similar characteristics to surface plasmons and were used to enhance the excitation rate of fluorophores. Bragg mirror in the structure works to shape the emission towards the detector. In a model immunoassay experiment, the enhancement of the limit of detection by an order of magnitude was achieved with respect to regular total internal reflection fluorescence method (TIRF). A new compact biosensor chip with optical diffractive elements was developed. It allows simultaneous excitation and efficient collection of fluorescence light via the confined surface plasmon modes. The developed prototype was examined in a model immunoassay experiment. The preliminary results showed the sensitivity at picomolar range. This approach combines the advantages of methods referred to as surface plasmon-enhanced fluorescence spectroscopy (SPFS) and surface plasmon-coupled emission (SPCE). They are typically implemented by bulky benchtop devices and need to be operated in specialized laboratories.

This approach holds potential for the exploitation of plasmon-enhanced fluorescence assays outside such laboratories in portable biosensor devices. This technology is urgently needed in important areas such as point-of-care medical diagnostics (rapid and simple detection of biomarkers), security and food control (rapid analysis of harmful compounds) or environmental monitoring (on-site detection of pollutants).

5. PUBLICATIONS

K. Toma, J. Dostalek, and W. Knoll, "Long range surface plasmon-coupled fluorescence emission for biosensor applications," Optics Express **19**, 11090-11099 (2011).
Also selected in The Virtual Journal for Biomedical Optics **6**, 7 (2011).

M. Toma*, **K. Toma***, P. Adam, J. Homola, W. Knoll, and J. Dostálek, "Surface plasmon-coupled emission on plasmonic Bragg gratings," Optics Express **20**, 14042-14053 (2012). *Authors equally contributed to this work.

K. Toma, M. Vala, P. Adam, J. Homola, W. Knoll and J. Dostalek, "Compact Biochip for Surface Plasmon-Enhanced Fluorescence Assays", *submitted*.

K. Toma, M. Ballarini, W. Knoll, M. Toma, U. Jonas, E. Descrovi and J. Dostalek, "Bloch surface wave-enhanced fluorescence biosensor", *in preparation*.

Submitted to small

DOI: 10.1002/smll.((please add manuscript number))

Compact Biochip for Surface Plasmon-Enhanced Fluorescence Assays

*Koji Toma, Milan Vala, Pavel Adam, Jiří Homola, Wolfgang Knoll and Jakub Dostálek**

[*] Dr. J. Dostálek, K. Toma, Prof. W. Knoll
AIT - Austrian Institute of Technology GmbH, Muthgasse 11, 1190 Vienna (Austria)
E-mail: jakub.dostalek@ait.ac.at

M. Vala, P. Adam, Prof. J. Homola
Institute of Photonics and Electronics, Czech Academy of Sciences, Chaberská 57, 182 51 Prague (Czech Republic)

Supporting Information is available on the WWW under http://www.small-journal.com or from the author.

Keywords: surface plasmon, fluorescence, diffraction, grating, biosensor

A new compact biochip for surface plasmon-enhanced fluorescence biosensors is developed. It takes advantage of fluorescence signal amplification based on the coupling of fluorophore excitation and emission channels with confined and strongly enhanced field intensity of surface plasmons on a metallic sensor surface. In order to excite and collect the fluorescence light emitted by fluorophore labels via surface plasmons, (reverse) Kretschmann configuration is combined with diffractive optical elements embedded on the chip surface. These include a concentric relief grating for the imaging of highly directional surface plasmon-coupled emission light beam at the emission wavelength to a detector. Additional linear grating is used for the generating of surface plasmons at the excitation wavelength on the sensor surface in order to increase the fluorescence excitation rate. The reported approach offers the advantage of increased intensity of fluorescence signal, reduced background, and compatibility with nanoimprint lithography for cost-effective preparation of sensor chip. The potential of

presented approach is demonstrated in a model immunoassay experiment in which the limit of detection of 11 pM is achieved.

1. Introduction

The interaction of nano-scale emitters with metallic surfaces was extensively studied[1-3] in the framework of plasmonics – emerging field of photonics that focuses on the manipulation of light at sub-wavelength dimensions through its coupling with highly confined field of surface plasmons.[4, 5] These efforts find increasing number of applications in fluorescence-based analytical tools for detection of molecular and biological analytes.[6-10] Particularly, this research addresses needs for enhanced sensitivity and shortened analysis times in important areas of medical diagnostics and food control. In plasmon-enhanced fluorescence (PEF) which is also referred to as metal-enhanced fluorescence (MEF), the coupling of fluorophore labels with surface plasmons on continuous metallic films[7, 11] or metallic nanoparticles[12, 13] offers means for improving the sensitivity in fluorescence bioassays through the combination of increased fluorophore excitation rate, decreased background signal, directional fluorescence emission and improved fluorophore quantum yield. These phenomena occur when captured fluorophore-labeled molecules are exposed to the enhanced intensity of surface plasmon field which originates from oscillations of electron density and associated electromagnetic field at close proximity to a metal surface.

Up to now, two main approaches utilizing propagating surface plasmons (SPs) for the amplification of fluorescence signal in biosensor applications were pursued. In surface plasmon-enhanced fluorescence spectroscopy (SPFS), the binding of fluorophore-labeled molecules to biomolecular recognition elements attached to a metallic sensor surface is probed by SPs at the wavelength matching the absorption band of used fluorophore labels.

This method was utilized with Kretschmann configuration of attenuated total reflection (ATR) method[11] and metallic diffraction gratings[14] enabling the excitation of SPs on the sensor surface. The enhanced field intensity of SPs increases the excitation rate of captured fluorophore-labeled molecules, which is directly translated to an increased intensity of emitted fluorescence light. In surface plasmon-coupled fluorescence emission (SPCE),[15, 16] fluorescence light emitted via surface plasmons at the emission wavelength is detected. Reverse Kretschmann configuration of ATR method[15, 17] and metallic diffraction gratings were used in order to extract the fluorescence light trapped by SPs and it offers the advantage of highly directional emission. This approach provides means for efficient collecting of fluorescence light and it enables the discrimination between background and fluorescence signals.

In this paper, we report a new approach to PEF biosensors that makes it possible to harness both SP-enhanced excitation and collection of fluorescence light intensity. It is based on Kretschmann configuration combined with diffractive optical elements for the excitation of surface plasmons at the fluorophore absorption wavelength and for the imaging of enhanced intensity of surface plasmon-coupled emission at the emission wavelength to a detector. These key optical elements can be fabricated on biochip surface by nanoimprint lithography with the potential for cost-effective production. This approach does not require optical matching to an optical prism, which makes it attractive for the development of compact sensing devices with disposable biochips. With respect to PEF exploiting linear metallic gratings for direct coupling of SPs to far field radiation,[14] the excitation light beam does not pass through the analyzed sample, which reduces the background signal and allows the measurements of reaction kinetics on the surface.

2. Results and Discussion

2.1 Surface plasmon-mediated fluorescence excitation and emission

As seen in simulations based on Chance-Prock-Silbey model[18] shown in **Figure 1**, the coupling of a fluorophore with surface plasmons strongly depends on the distance from a metal surface *d*. For a gold surface in contact with an aqueous medium and a fluorophore represented as a randomly oriented dipole, these simulations reveal that the majority of emitted light at the emission wavelength of λ_{em}=670 nm is coupled to propagating SPs at the distance around *d*=20 nm from the surface. Below this distance, the emission is strongly quenched by Förster energy transfer, while at the distances *d*>50 nm the majority of light intensity is emitted to waves propagating into free space.

Figure 1

For a thin gold film attached to a dielectric substrate, the fluorescence light emitted via SPs is transmitted through the metal film and forms a characteristic SPCE cone which is directional in polar angle θ_{em} and isotropic in azimuth angle ϕ, see Figure 1. In **Figure 2**, we simulated the dependence of the fluorescence intensity *F* on the polar angle θ_{em}, assuming a randomly oriented dipole to be located on the top of 20 nm thick spacer layer (thus *d*=20 nm), a 50 nm thick gold layer and a BK7 glass substrate. The SPCE intensity peaks at the polar angle θ_{em}=72 deg that is the plasmon resonance angle at the emission wavelength λ_{em}=670 nm. For the identical layer structure, electric field intensity enhancement $|\mathbf{E}/\mathbf{E_0}|^2$ at *d*=20 nm was calculated upon the excitation of SPs by a light beam hitting the gold surface from the substrate under the angle of incidence θ_{ex} at the excitation wavelength λ_{ex}=633 nm. The results in Figure 2 reveals that strong field intensity builds up at the angle θ_{ex}=74 deg where the resonant condition for the excitation of SP at λ_{ex} is fulfilled.

Figure 2

2.2 Biochip development

As seen in the **Figure 3**, the biochip is composed of a BK7 glass slide with a sensing area coated with a 50 nm thick gold film and attached biomolecular recognition elements for the specific capture of fluorophore-labeled target molecules on its top. In order to collect the fluorescence light intensity emitted in the form of a SPCE cone from the sensing area at the fluorophore emission wavelength λ_{em}=670 nm, a relief concentric diffraction grating (CG) surrounding the sensing area was used. The grating is chirped in the radial direction in order to function as a diffraction lens which images the SPCE cone emitted from the sensing area to a narrow spot below the biochip. The SPCE cone propagating at polar angles between θ_{em}=67-77 deg (see Figure 2) in the glass substrate is totally internally reflected at the bottom glass surface, hits CG element coated with 200 nm thick gold film, and is diffracted to a converging wave that focuses at a desired distance *D* below the biochip where a detector is placed (see **Figure 3b**).

Figure 3

The dependence of the grating period Λ on the distance from the grating center *r* was determined by simulations (shown in **Figure S1** in Supporting Information) in order to diffract the incident SPCE beam to the -1st order that propagates away from the surface through the glass substrate and converges at *D*=10 mm. Sinusoidal relief corrugation was used with the average modulation depth of 120 nm which, according to the finite element method (FEM) simulations, provides the maximum diffraction efficiency of 81 % at the emission wavelength (see **Figure S2a** in Supporting Information). In order to couple the excitation

beam at the wavelength matching the absorption band of fluorophore, an additional linear grating (LG) was employed. LG with the period of Λ=437 nm was used which allows to couple normal incident monochromatic beam at λ_{ex}=633 nm to a wave that propagates along in the glass substrate and totally internally reflects at the bottom and top interfaces with the angle θ_{ex}=74 deg. When hitting the sensing area coated with 50 nm thick gold film and aqueous sample on the top, the light beam excites SPs on the surface as this angle coincides with SP resonance angle (see Figure 2). LG exhibited sinusoidal profile with the modulation depth around 110 nm. For the 1st order of diffraction, simulations predict a moderate diffraction efficiency of 34 % (see **Figure S2b** in Supporting Information).

Figure 4a shows the preparation of CG and LG elements by using interference lithography. For the CG element, a photoresist-coated substrate was exposed to chirped interference field through a mask with a wedge window exhibiting an angular width δ (δ=10 or 3 deg). The interference pattern formed at the intersection of a collimated and divergent laser-beam was tuned in order to achieve the desired radial chirp of the CG element (see Figure S1 in Supporting Information). The whole CG element was approximated as a set of chirped linear gratings by sequentially rotating the substrate with an angular step δ. LG element was recorded by using an interference field at the intersection of two collimated light beams. After the exposure of the photoresist to the interference field, the gratings were developed. In order to prepare multiple replicas of CG and LG elements, master photoresist gratings were casted to a PDMS stamp and transferred into a UV curable polymer followed by the gold deposition as shown in **Figure 4b**.

Figure 4

2.3 Biochip imaging properties

The imaging properties of CG were observed by the measurement of spatial distribution of out-coupled fluorescence light at different distances *D* below the biochip (optical setup is shown in **Figure S3** in Supporting Information). The sensing area of the chip carrying CG (see **Figure 5a**) was coated with 20 nm thick PMMA layer doped with DiD dyes (exhibiting similar characteristics to Alexa Fluor 647 used in further biosensor experiments described in section 2.4). In the used setup, the top of the sensing area was brought in contact with water and exposed to a normal incident laser beam at the wavelength λ_{ex} illuminating the area of around ~1 mm^2. As seen in Figure 5a, the intensity of fluorescence light exhibits a characteristic ring distribution with a decreasing diameter when increasing the distance *D*. The fluorescence beam is focused and reaches a minimum area at the distance of *D*~15 mm which is close to that predicted by simulations. The diameter of the spot at which the fluorescence light is confined depends on the angular width of segments approximating the CG element. As **Figure 5b** shows, the area of the spot at which the fluorescence beam is focused is decreasing when decreasing the angular step of CG element δ and the width of the spot 0.7 mm (full width at half maximum - FWHM) was observed for the segment angular width of δ=3 deg. Let us note that additional broadening of the focused fluorescence spot is caused by the finite size of the area illuminated by the excitation beam and by chromatic abberation of the CG lens. The fluorescence intensity detected in the focal plane at the wavelength λ_{em}=670 nm is increased when dyes are excited with the enhanced intensity of surface plasmons at the excitation wavelength λ_{ex}=633 nm. In further experiments, the excitation laser beam was coupled to the biochip by using LG element, propagated along in the biochip substrate and excited SPs on the sensing area at the resonance angle θ_{ex}. Only moderate enhancement ~2.3 of the fluorescence light collected by SPCE was obtained with respect to that measured for normal incident excitation beam from the top (data not shown).

This is due to the relatively low diffraction efficiency of LG (reducing the intensity by a factor <0.34) and attenuation by multiple reflections at the surface between BK7 glass substrate and 200 nm thick gold (reducing the intensity by a factor <0.6) which decreases the excitation light intensity by a factor higher than ~5. These values are in agreement with the the electric field intensity enhancement predicted by the simulations in Figure 2.

Figure 5

2.4 Model immunoassay experiment

The developed biochip was employed in a model detection experiment by using an optical setup and surface architecture depicted in **Figure 6**. A laser beam at the wavelength λ_{ex} was coupled into the biochip by using LG element and excited SPs in the sensing area. The gold surface of the sensing area was modified with a thiol self-assembled monolayer (SAM) which serves as a linker for the covalent coupling of mouse immunoglobulin G (mIgG) molecules or reference rabbit IgG (rIgG) molecules. A flow cell was attached to the biochip top surface in order to flow the liquid samples with target anti-mouse IgG (a-mIgG) that was labeled with Alexa Fluor 647 along the sensing area. The fluorescence intensity F at the emission wavelength λ_{em} originating from the captured target a-mIgG was detected from SPCE signal focused below the biochip. The fluorescence light was collected by a microscope objective forming a parallel fluorescence beam that subsequently passed through a set of filters and was delivered to photomultiplier detector.

Figure 6

The kinetics of fluorescence signal upon the affinity binding of target molecules was measured upon sequential flow of samples with increasing concentration of a-IgG. Each sample was flowed over the sensor surface for 10 minutes followed by the 10 minutes rinsing. **Figure 7a** shows the measured fluorescence signal kinetics for the concentrations of a-mIgG between 30 pM and 30 nM. It shows that the binding of the labeled a-mIgG to the surface modified with mIgG results in the fluorescence signal *F* gradual increasing in time. The slope of the fluorescence signal *dF*/*dt* linearly increases with concentration of a-mIgG. In the control experiment, identical a-mIgG samples were flowed over the sensor surface modified with rIgG which is not specifically recognized by a-mIgG. The sensorgram in Figure 7a shows negligible increase in the fluorescence signal, indicating the highly specific response. Using the kinetics data (measured in triplicate), the calibration curve was obtained (**Figure 7b**). For each a-mIgG concentration, the fluorescence signal slope *dF*/*dt* in the initial association phase was determined by linear fitting and plotted as a function of the concentration. The error bars show the obtained standard deviation (SD) that is attributed to the chip to chip variability. The limit of detection (LOD) of 11 pM was determined at the intersection where the sensor signal *dF*/*dt* matches 3-fold SD of the baseline fluorescence signal 83 cps min^{-1}.

Figure 7

3. Conclusions

A compact biochip for sensitive fluorescence-based assays was developed. The amplification of fluorescence signal by combining surface plasmon-enhanced excitation and surface plasmon-coupled emission of fluorescence light intensity was implemented by using two diffractive elements – linear and concentric gratings. The biochip was prepared by UV-nanoimprint lithography from master gratings fabricated by interference lithography and is

thus compatible with mass production technologies. The integration of the key optical elements to the biochip allowes for substantial simplification of the sensor design, opening avenues for the development of compact portable devices for the use in the field. In a model immunoassay experiment, the biochip provided sensitivity enabling the detection of IgG molecules at concentrations as small as 11 pM.

4. Experimental Section

Materials: Polydimethylsiloxane (PDMS) prepolymer and its curing agent were purchased from Dow Corning (SYLGARD® 184). Poly(methyl methacrylate) (PMMA) was from Sigma-Aldrich Handels (Austria). 1,1'-dioctadecyl-3,3,3',3'-tetramethylindodicarbocyanine, 4-chlorobenzenesulfonate salt (DiD) was from Invitrogen. This dye exhibits the absorption and emission bands centred at wavelengths of λ_{ab}=644 nm and λ_{em}=665 nm, respectively, and it was dispersed at the concentration of 700 nM in a toluene with PMMA (1.4 wt.%). Dithiolalkanearomatic PEG 6-COOH (COOH-thiol) and dithiolalkanearomatic PEG3-OH (PEG-thiol) were from SensoPath Technologies (USA). Phosphate buffered saline (PBS) with pH 7.4 was obtained from Calbiochem (Germany). PBS-Tween (PBS-T) buffer was prepared by adding 0.05% of Tween20 (Sigma-Aldrich, USA) to PBS buffer solution. Mouse immunoglobulin G (mIgG) and anti-mouse IgG (a-mIgG) were from Molecular Probes (USA). Molecules of a-mIgG were labeled with Alexa Fluor 647 with the dye-to-protein molar ratio of 4.5. This dye exhibits the absorption and emission wavelengths of λ_{ab}=650 nm and λ_{em}=668 nm, respectively. Rabbit immunoglobulin G (rIgG) was from Abcam (USA). 10 mM acetate buffer (ACT) with pH 5.5 was prepared in house. 1-Ethyl-3-(3-dimethylaminopropyl) carbodiimide (EDC) and N-hydroxysuccinimide (NHS) were from Pierce (USA). Ethanolamine (Sigma-Aldrich, USA) was dissolved in water at 1 M concentration with the pH of the solution adjusted to 8.5 with sodium hydroxide.

Biochip preparation: Interference lithography (holography) was used for the preparation of master gratings. Two different masters with linear sinusoidal relief grating (LG) and concentric relief chirped grating (CG) were by an exposure of positive photoresist (S1818, Shipley, USA) to an interference field of two laser beams (HeCd laser IK3031R-C from Kimmon Koha, Japan) on a glass substrate followed by its development in developer (AZ303, Microchemicals, Germany, diluted 1:9 with water) and characterization by atomic force microscopy (Multimode, Veeco, USA) (data not shown). LG exhibited the period of Λ=436 nm and depth of 100 nm. CG was composed of 120 (δ=3 deg) or 36 (δ=10 deg) segments carrying chirped gratings with the period decreasing from Λ=365 to 313 nm at the radial distance increasing from r=4.7 to 8.5 mm, respectively. The average modulation depth of the CG grating was 110 nm as determined by AFM. The replication of the master grating was performed by means of UV-nanoimprint lithography as described previously in our laboratory[19]. Gold layers with the thickness of 50 and 200 nm were deposited on the flat sensing area and the outer area of the chip carrying CG and LG, respectively, by sputtering (UNIVEX 450C, Leybold Systems, Germany).

Simulations: Finite element method (FEM) grating solver DiPoG (Weierstrass Institute, Germany) was used for the calculation of the diffraction efficiency. The chirped grating and the overall sensor chip geometry was designed by using a ray-tracing tool Zemax (Radiant Zemax, USA). For the simulation of surface plasmon coupled emission, home-developed scripts based on the CPS-model was used as described in our previous works.[20] Refractive indices of gold of n_m=0.118+3.92i at λ_{em}=670 nm and n_m=0.153+3.52i at λ_{ex}=633 nm were assumed. In simulations, 20 nm thick spacer layer with the refractive index n_l=1.45 between a

fluorophore and gold surface was used. Refractive indices of glass substrate and water of n_p=1.51 and n_s=1.33, respectively, were used.

Surface modification: For the observation of imaging properties of CG element, 20 nm thick PMMA layer doped with DiD dye was spin-coated on a gold coated surface and dried overnight at the room temperature. In order to function as a biosensor, the sensing area with 50 nm thick gold layer was modified with a mixed thiol self-assembled monolayer (SAM), and IgG molecules were covalently attached to SAM carboxylic functional moieties. The biochip was immersed in a mixture of PEG-thiol and COOH-thiol dissolved in ethanol (molar ratio of 9:1 and total concentration of 1 mM[19]) overnight at the room temperature. Afterwards the biochip was rinsed with ethanol and dried in a stream of nitrogen. mIgG antibodies were immobilized by amine coupling. Carboxylic terminal groups of COOH-thiol were activated by EDC and NHS solution (concentrations in deionized water of 75 and 21 mg/mL, respectively) for 15 min, followed by the incubation with mIgG dissolved in ACT buffer at the concentration of 50 μg/mL for 90 min. Unreacted active ester groups of the COOH-thiol were passivated by 20 min incubation in ethanol amine solution. In the control experiment, rIgG with the same concentration were immobilized instead of mIgG.

Optical setups for testing of biochip performance: Details describing the optical setup used in the characterization of the imaging properties of CG is in Supporting Information (Figure S3). For the model bioassay experiment, the SPCE signal imaged by CG element was collected by a microscope objective (NA=0.85, NT38-340, Edmund Optics, Germany) and its intensity *F* was detected by a photomultiplier tube (H6240-01, Hamamatsu, Japan) which was connected to a counter (53131A, Agilent, USA) (Fig.5b). The identical set of filters was used to suppress the background signal also in the characterization of the imaging properties of CG.

Acknowledgements

Support for this work was partially provided by the Austrian NANO Initiative (FFG and BMVIT) through the NILPlasmonics project within the NILAustria cluster (www.NILAustria.at) and by the Czech Science Foundation under grant # P205/12/G118.

References

[1] G. W. Ford and W. H. Weber, Physics Reports **1984**, *113*, 195.
[2] V. Giannini, A. I. Fernandez-Dominguez, Y. Sonnefraud, T. Roschuk, R. Fernandez-Garcia and S. A. Maier, Small **2011**, *6*, 2498.
[3] V. Giannini, A. I. Fernandez-Dominguez, S. C. Heck and S. A. Maier, Chem. Rev. **2011**, *111*, 3888.
[4] B. Auguie and W. L. Barnes, Phys. Rev. Lett. **2008**, *101*, 4.
[5] J. A. Schuller, E. S. Barnard, W. S. Cai, Y. C. Jun, J. S. White and M. L. Brongersma, Nat. Mater. **2010**, *9*, 193.
[6] T. Neumann, M. L. Johansson, D. Kambhampati and W. Knoll, Advanced Functional Materials **2002**, *12*, 575.
[7] J. Dostalek and W. Knoll, Biointerphases **2008**, *3*, FD12.
[8] J. R. Lakowicz, K. Ray, M. Chowdhury, H. Szmacinski, Y. Fu, J. Zhang and K. Nowaczyk, Analyst **2008**, *133*, 1308.
[9] M. F. Garcia-Parajo, Nat. Photonics **2008**, *2*, 201.
[10] E. Fort and S. Gresillon, J. Phys. D-Appl. Phys. **2008**, *41*,
[11] T. Liebermann and W. Knoll, Colloids and Surfaces a-Physicochemical and Engineering Aspects **2000**, *171*, 115.
[12] M. E. Stewart, C. R. Anderton, L. B. Thompson, J. Maria, S. K. Gray, J. A. Rogers and R. G. Nuzzo, Chemical Reviews **2008**, *108*, 494.
[13] L. Touahir, E. Galopin, R. Boukherroub, A. C. Gouget-Laemmel, J. N. Chazalviel, F. Ozanam and S. Szunerits, Biosensors & Bioelectronics **2010**, *25*, 2579.
[14] K. Tawa, Y. Yokota, K. Kintaka, J. Nishii and T. Nakaoki, Sensors and Actuators B-Chemical **2011**, *157*, 703.
[15] J. R. Lakowicz, J. Malicka, I. Gryczynski and Z. Gryczynski, Biochemical and biophysical research communications **2003**, *307*, 435.
[16] J. R. Lakowicz, Anal. Biochem. **2004**, *324*, 153.
[17] J. S. Yuk, M. Trnavsky, C. McDonagh and B. D. MacCraith, Biosensors & Bioelectronics **2010**, *25*, 1344.
[18] R. R. Chance, A. Prock and Silbey, Adv. Chem. Phys **1978**, *37*,
[19] Y. Wang, J. Dostalek and W. Knoll, Analytical Chemistry **2011**, *83*, 6202.
[20] K. Toma, J. Dostalek and W. Knoll, Optics Express **2011**, *19*, 11090.

Submitted to NANO MICRO small

Received: ((will be filled in by the editorial staff))
Revised: ((will be filled in by the editorial staff))
Published online on ((will be filled in by the editorial staff))

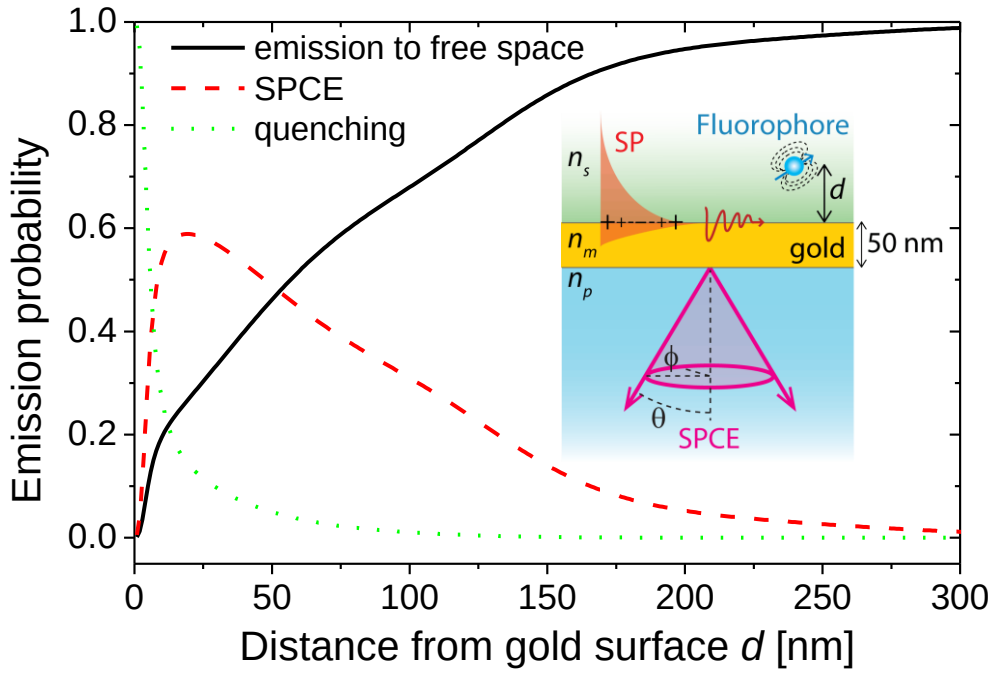

Figure 1. The probability of the emission from a randomly oriented dipole occurring via surface lossy waves (quenching), surface plasmons (SPCE) and optical waves propagating into free space as a function of the distance from a metal surface *d*.

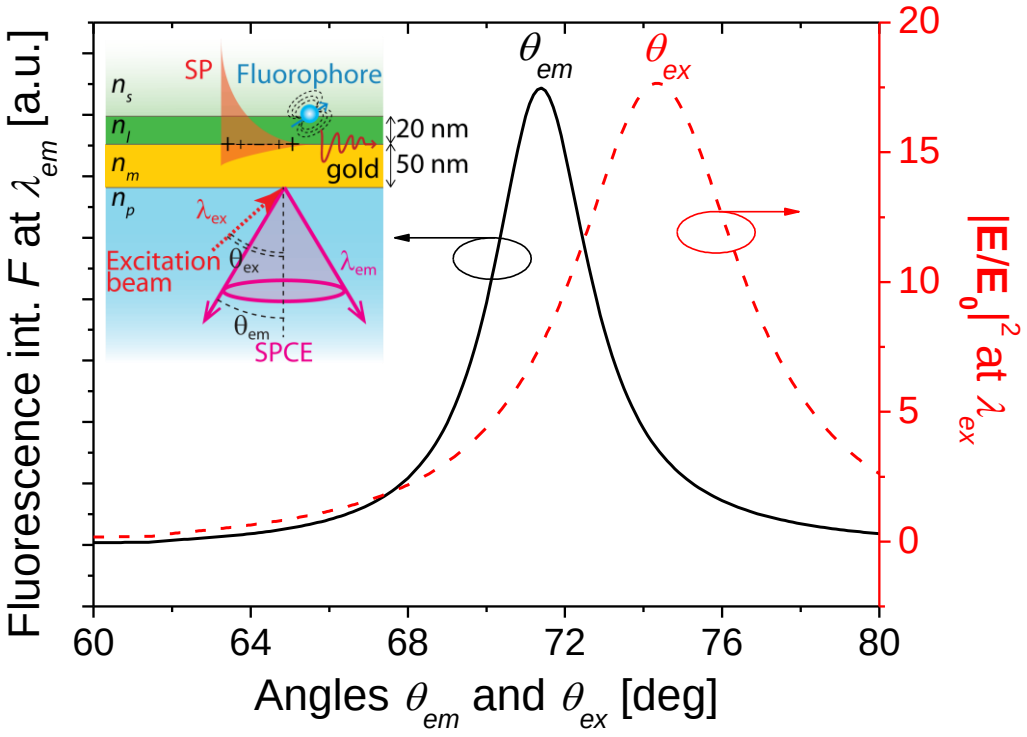

Figure 2. Dependence of the fluorescence intensity F of SPCE from a randomly oriented dipole at the distance d=20 nm from the gold surface at the wavelength of λ_{em}=670 nm (black solid line) on the polar angle θ_{em}. The electric field intensity enhancement $|E/E_0|^2$ at d=20 nm due the excitation of SPs at the wavelength λ_{ex}=633 nm is shown as a function of the angle of incidence θ_{ex} (red dashed line).

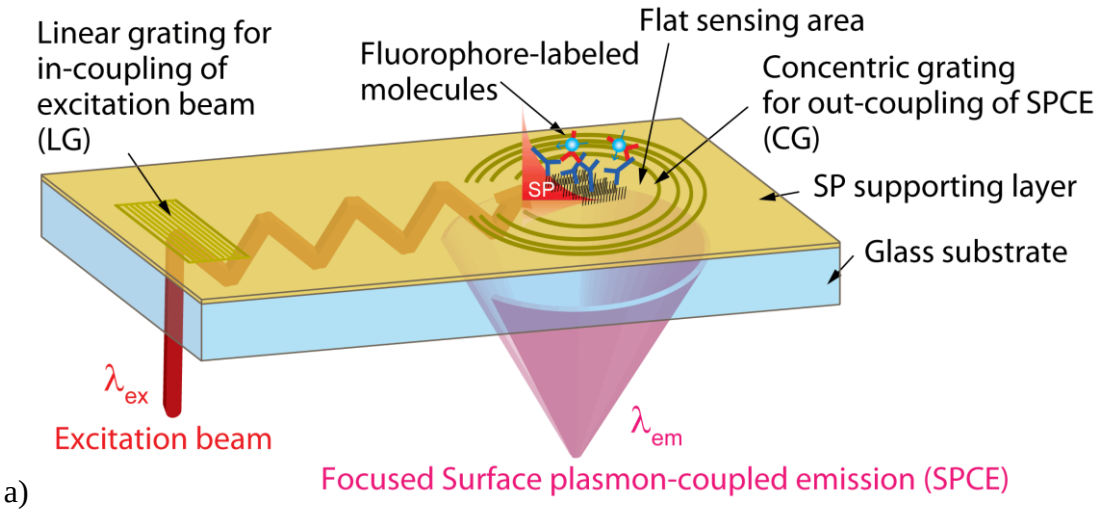

a)

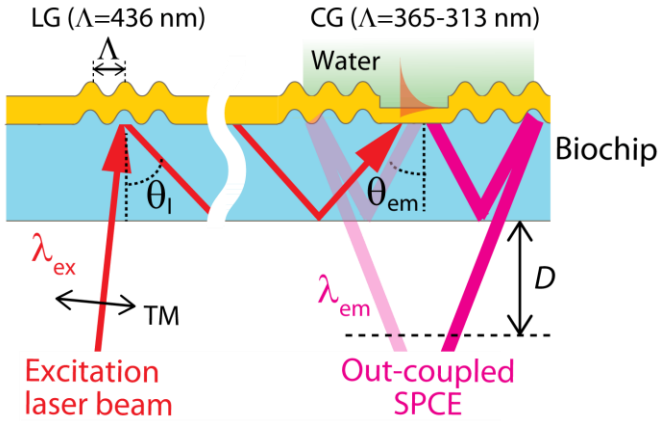

b)

Figure 3. a) Schematic of the biochip with diffractive optical elements for the in-coupling of the excitation beam (linear grating) to the biochip and for the out-coupling and imaging of surface plasmon-coupled emission (SPCE) to a detector (concentric grating). b) Side-view of the biochip.

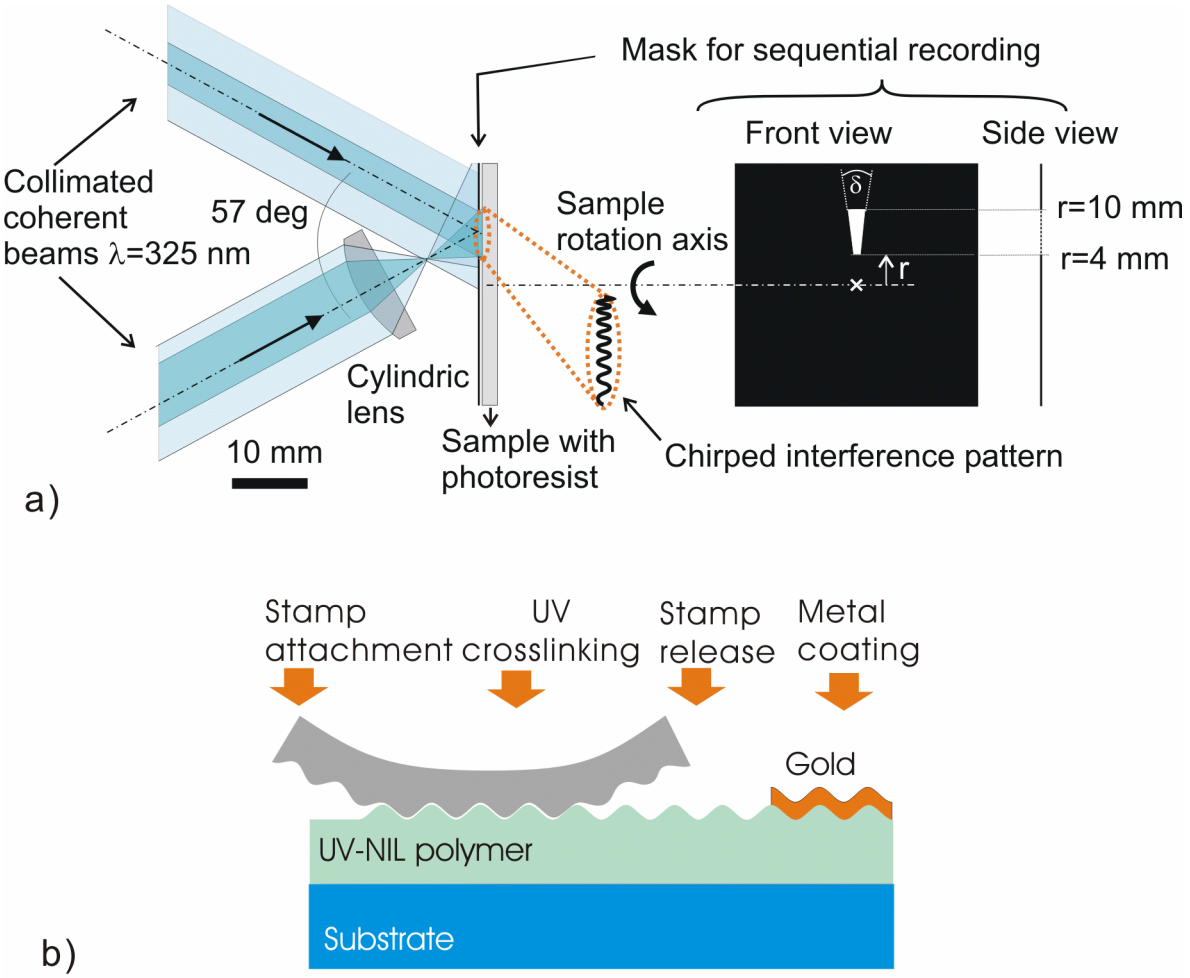

Figure 4. a) Preparation of the concentric grating element (CG) by using sequential recording into a photoresist by using interference lithography. b) Transfer of the grating elements onto the biochip surface by UV-NIL.

a)

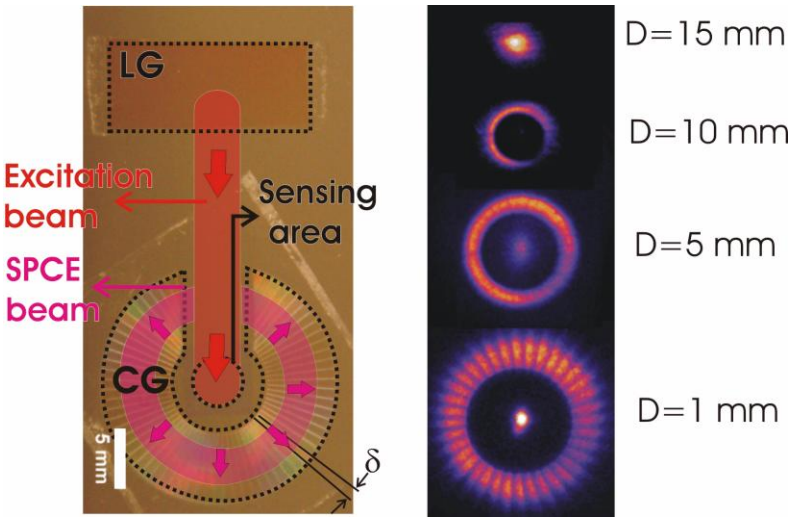

b)

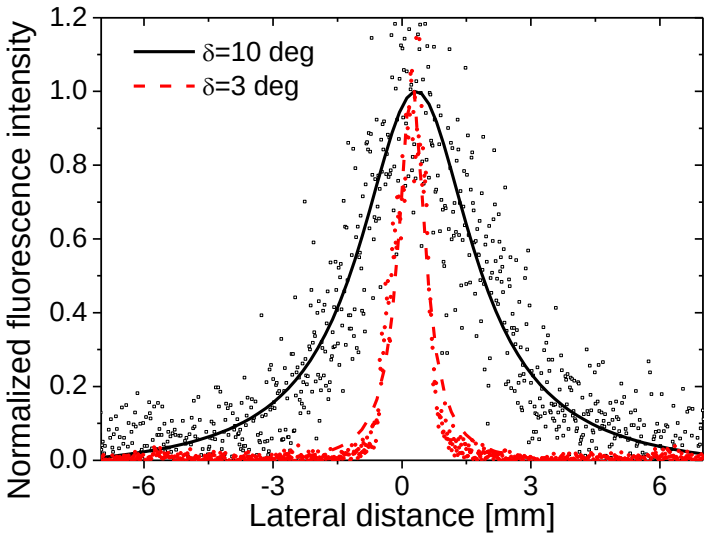

Figure 5. a) Top view of prepared biochip carrying LG and CG diffractive elements (left) and measured spatial distribution of SPCE cone out-coupled from the biochip by using CG element at increasing distance below the biochip *D*=1, 5, 10 and 15 mm. b) The cross-section of the fluorescence light at the distance of *D*=15 mm from the bottom of the biochip for angular width of the CG element δ=3 and 10 deg.

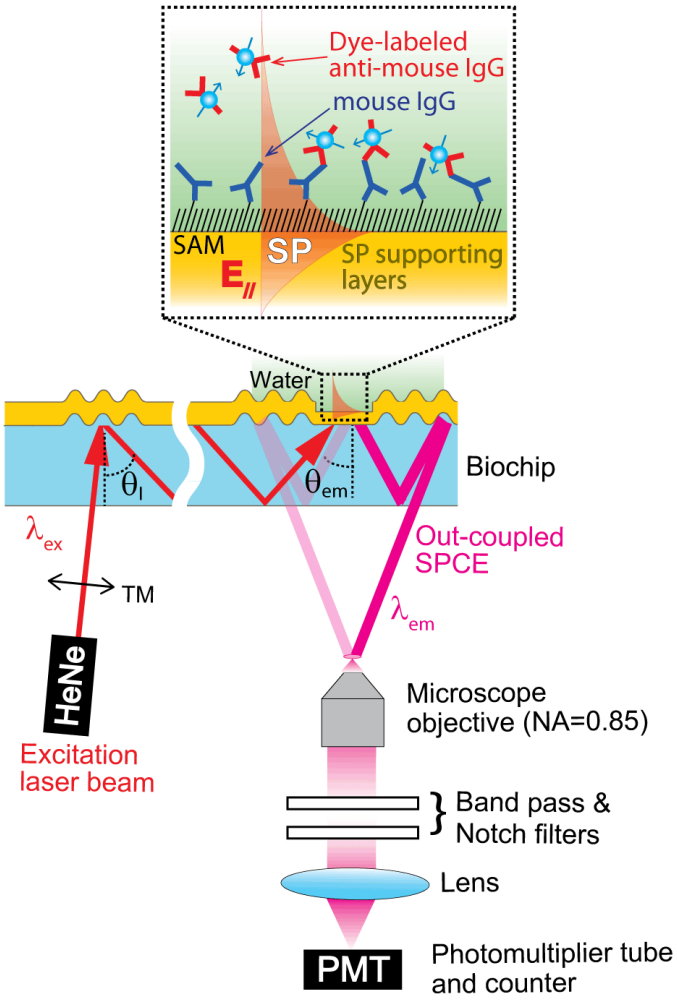

Figure 6. Optical setup employed for the model immunoassay experiment utilizing the amplification of fluorescence signal by using the developed biochip.

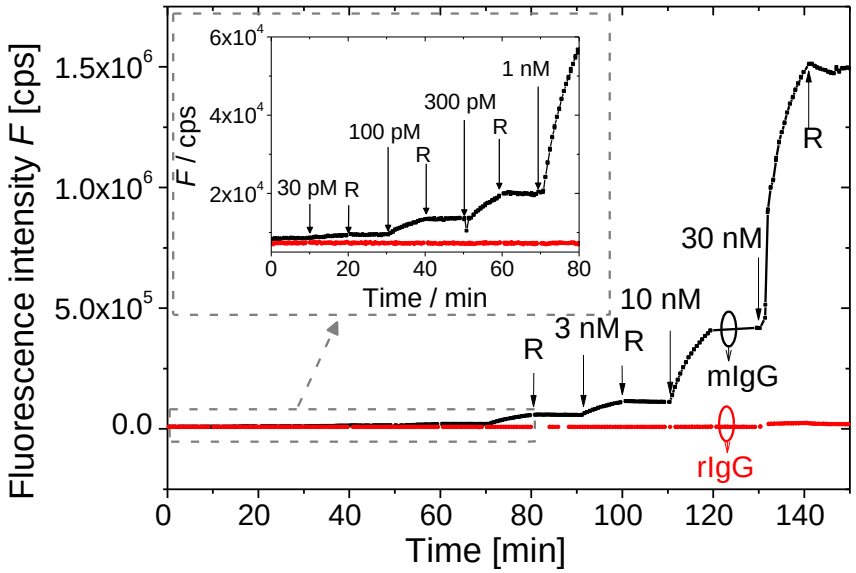

a)

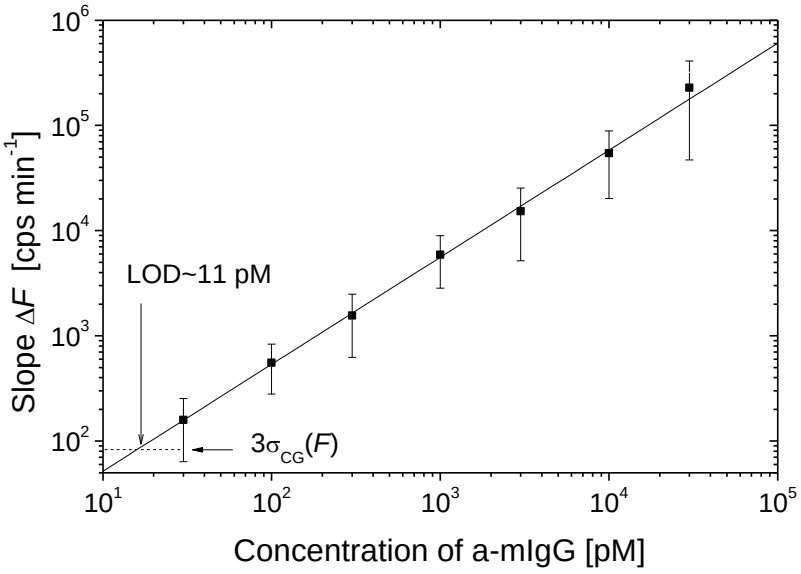

b)

Figure 7. a) Measured binding kinetics $F(t)$ upon the sequential flow of samples with a-mIgG along the surface carrying the specific affinity partner mIgG (black) and control molecules rIgG (red). The inserted graph shows the magnified fluorescence intensity $F(t)$ for the concentration from 30 pM to 1 nM. b) Calibration curve of the developed biochip fitted with a linear function. The baseline noise and LOD are indicated.

TOC Keyword: surface plasmon, fluorescence, diffraction, grating, biosensor

Koji Toma, Milan Vala, Pavel Adam, Jiri Homola, Wolfgang Knoll and Jakub Dostalek*

Title: Compact Biochip for Surface Plasmon-Enhanced Fluorescence Assays

ToC figure:

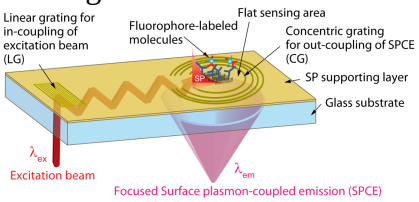

Page Headings
Left page: K. Toma et al.
Right page: Plasmon-Enhanced Fluorescence Biochip

Submitted to small NANO MICRO

Supporting Information

Compact Biochip for Surface Plasmon-Enhanced Fluorescence Assays

Koji Toma, Milan Vala, Pavel Adam, Jiří Homola, Wolfgang Knoll and Jakub Dostálek*

Dr. J. Dostálek, K. Toma, Prof. W. Knoll
AIT - Austrian Institute of Technology GmbH, Muthgasse 11, 1190 Vienna (Austria)
*E-mail: jakub.dostalek@ait.ac.at

M. Vala, P. Adam, Prof. J. Homola
Institute of Photonics and Electronics, Czech Academy of Sciences, Chaberská 57, 182 51 Prague (Czech Republic)

Design of periodic modulation of CG grating element

Figure S1 shows the simulated dependence of the CG period Λ on the distance from its centre r that allows the imaging of SPCE from a sensing area on the biochip surface to a spot at the distance D=10 mm below the bottom biochip surface. The simulated dependence (dashed line) is compared to that was measured by AFM (squares) with standard deviation represented as error bars.

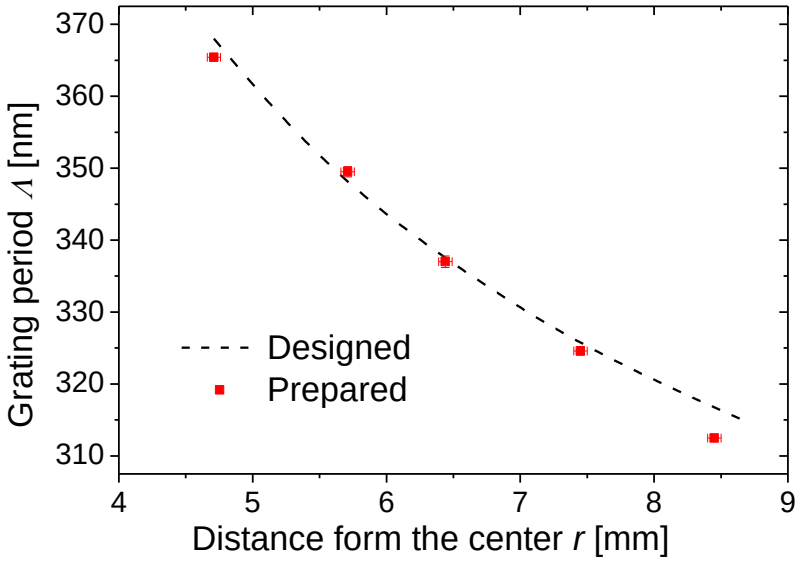

Figure S1. Dependence of the concentric grating period on the distance from its center obtained from simulations (line) and measured on prepared biochips (squares).

FEM simulations of diffraction efficiency of LG and CG elements

Figure S2 a) and b) shows the calculated dependence of the efficiency of LG and CG elements, respectively, on the modulation depth for a sinusoidal relief modulation profile.

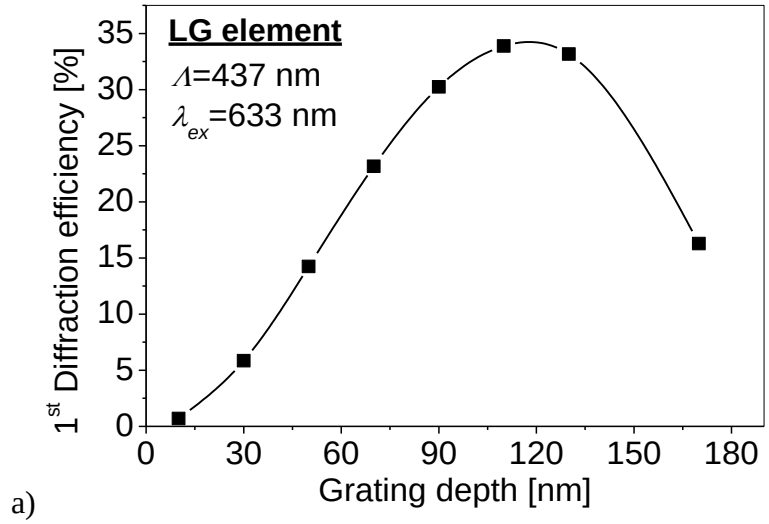

a)

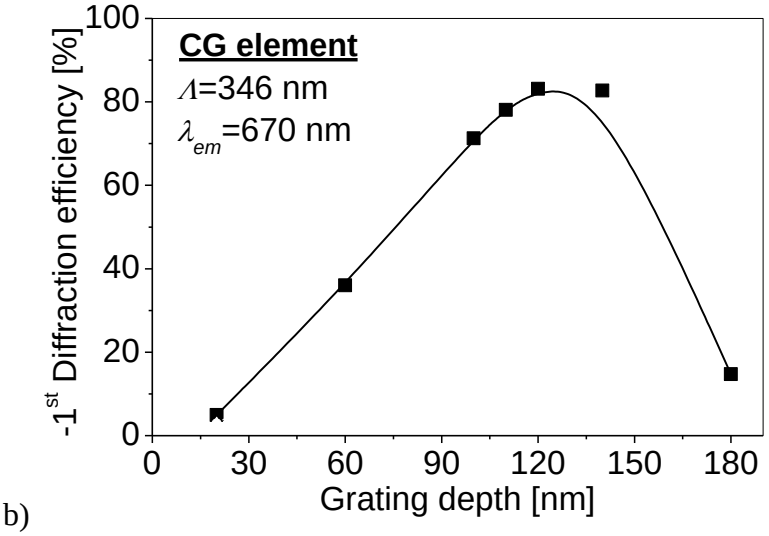

b)

Figure S2. Simulated diffraction efficiency in the ±1st orders as a function of the grating depth for a) the sinusoidal linear grating (LG) element with the period of Λ=437 nm for the normal incident TM polarized beam at the wavelength of λ_{ex}=633 nm and b) the sinusoidal concentric grating (CG) element (Λ=346 nm) for the TM polarized light beam incident at the emission angle θ_{em}=71 deg at the emission wavelength λ_{em}=670 nm.

Optical setup for observation of the SCPE imaging by CG element

The SPCE beam that was diffracted by the CG element was made incident on a diffuser which was placed at a given distance *D* from the chip. The spatial distribution of scattered fluorescence light was imaged to an electron multiplying charge-coupled device (EM-CCD iXon+885, Andor Technology, Ireland) by a camera lens (UNIFOC 58, Schneider Kreuznach, Germany). A set of filters including notch filter (XNF-632.8-25.0M, CVI Melles Griot, Germany) and band-pass filter (670FS10-25, LOT-Oriel, Germany) was used in order to suppres the background signal. For the investigation of the amplification of the fluorescence intensity by using the surface plasmon-enhanced excitation, the excitation light beam was coupled to the biochip by using the LG element and exited surface plasmons on the sensing area (2). As a reference, direct fluorescence excitation was performed with the excitation light beam hitting the sensing area from above the biochip through water (1).

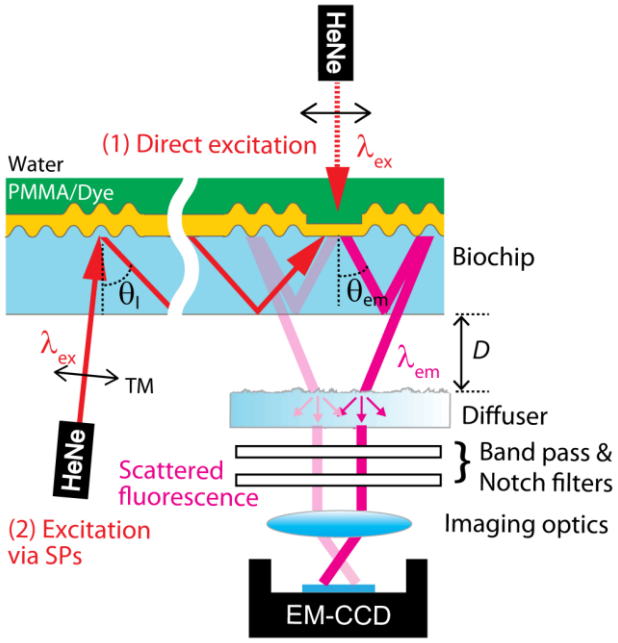

Figure S3. Optical setup for the observation of imaging properties of CG element and coupling efficiency of LG element.

Bloch surface wave-enhanced fluorescence biosensor

Koji Toma [a], Mirko Ballarini [b], Wolfgang Knoll [a], Mana Toma [a], Ulrich Jonas [c], Emiliano Descrovi [b], and Jakub Dostálek[a,*]

[a] *AIT - Austrian Institute of Technology GmbH, Muthgasse 11, 1190 Vienna, Austria*

[b] *Dipartimento di Scienza dei Materiali e Ingegneria Chimica, Politecnico di Torino, C.so Duca degli Abruzzi 24, 10129 Torino, Italy*

[c] *Macromolecular Chemistry, University of Siegen, Department Chemistry -Biology, Adolf-Reichwein-Strasse 2, Siegen 57076, Germany*

* Corresponding author, E-mail address: jakub.dostalek@ait.ac.at

Abstract

New approach to the amplification of fluorescence signal in heterogeneous assays for sensitive detection of molecular analytes is reported. It relies on a sensor chip carrying one-dimensional photonic crystal (1DPC) which is composed of two segments. The first segment on the top supports Bloch surface waves (BSWs) at the excitation wavelength and the second segment below serves as a Bragg mirror for the emission wavelength of used fluorophore labels. The two-segment 1DPC is designed to simultaneously increase the excitation rate through BSW-enhanced electromagnetic field intensity and to beam the emitted fluorescence light towards the detector. In the theoretical part of the work, simulations based on Chance-Prock-Sibley model are carried out in order to design the 1DPC layer structure and to study the distance dependence of the excitation strength and angular distribution of the emitted

fluorescence light. In experiments, increase of the fluorescence signal-to-noise ratio is demonstrated in a model immunoassay experiment in which around an order of magnitude improved limit of detection (LOD) was achieved with respect to regular total internal reflection fluorescence (TIRF) configuration.

Keywords:

Bloch surface wave, Fluorescence, Bragg mirror, Photonic crystal, Biosensor, Immunoassay

1. Introduction

Over the last decade, we witnessed growing needs for advanced analytical technologies with enhanced sensitivity and shortened analysis time in important areas of medical diagnostics [1] and food control [2]. Among various fluorescence-based approaches which arguably provide mostly used platforms for the detection and interaction analysis of molecular and biological analytes, plasmon-enhanced fluorescence (PEF) was studied to address these challenges. This method offers means for efficient amplification of fluorescence signal through the coupling of fluorophores with confined and enhanced field of surface plasmons on metallic surfaces [3-5] which were implemented to range of advanced assays and biological studies [6-10]. Bloch surface waves (BSW) supported by one-dimensional photonic crystal (1DPC) were studied over the last years and shown to provide similar optical properties like surface plasmons [11] and 1DPC structures can be designed to support BSWs that strongly enhance the electromagnetic field intensity on the surface [12, 13]. With respect to metallic materials applied for the plasmonic amplification of fluorescence, dielectric 1DPC may offer the advantage of the lack of fluorescence quenching by Förster energy transfer which occurs in close proximity to the metallic surface. In addition, these structures offer the advantage of flexibility in the design of virtually arbitrary dispersion relation of BSW and the employment

of low absorption loss materials allows the observation of extremely sharp resonances and large field intensity enhancement associated with the coupling to BSWs [14, 15].

In this paper we investigate a new approach for the amplification of fluorescence signal that utilizes dielectric 1DPC. We aim at implementing this type of photonic materials for advancing the sensitivity of fluorescence assays by the combination of two effects. Firstly, 1DPC is designed to enhance the excitation rate of fluorophore labels by the increased field intensity of BSW at the absorption wavelength of used fluorophores. Secondly, the collecting efficiency of emitted fluorescence light from the surface is improved by the control of its angular distribution. 1DPC is designed by simulations and 1DPC-based sensor chip is prepared based on it. A model immunoassay experiment showing the potential of the proposed 1DPC structure for sensitive detection of molecular analytes is presented.

2. Materials and methods

2.1 Materials

Polymer SU-8 2000.5 was purchased from Microchem (USA). Phosphate buffered saline (PBS, 140 mM NaCl, 10 mM phosphate, 3 mM KCl, and a pH of 7.4) was obtained from Calbiochem (Germany). PBS-Tween (PBS-T) buffer was prepared by adding 0.05 % of Tween20 (Sigma-Aldrich, USA) to PBS buffer solution. Mouse immunoglobulin G (mIgG) and anti-mouse IgG (a-mIgG) were from Molecular Probes (USA). a-mIgG was labeled with Alexa Fluor 647 dye with the dye-to-protein molar ratio of 4.5. This dye exhibits the absorption and emission wavelengths of λ_{ab}=650 nm and λ_{em}=668 nm, respectively. 10 mM acetate buffer (ACT) with pH=4 was prepared in house. 1-Ethyl-3-(3-dimethylaminopropyl) carbodiimide (EDC) was from Pierce (USA). Photocrosslinkable poly(N-isopropylacryamide) (NIPAAm)-based hydrogel modified with benzophenon groups for its cross-linking and

carboxylic moieties for the coupling of protein molecules and sodium para-tetrafluorophenol sulfonate (TFPS) were synthesized as described in literature [16]. Ethanolamine (Sigma-Aldrich, USA) was dissolved in water at 1 M concentration and the pH of the solution was adjusted to 8.5 by adding sodium hydroxide.

2.2 Preparation of sensor chip with 1DPC

1DPC was prepared on BK7 glass substrate by plasma-enhanced chemical vapor deposition (PECVD) of a stack of a-$Si_{1-x}N_x$:H layers. The nitrogen content x of silicon nitride layers was controlled by adjusting the ammonia fraction in SiH_4+NH_3 plasma in order to tune the refractive index. In the PECVD deposition process, the substrate temperature and the electrode distance were set to 220 °C and 20 mm, respectively. The total pressure of 0.45 Torr and the RF power density of 21 mW/cm^2 were used. The reactive gas flow ratio $[NH_3]/([SiH_4]+[NH_3])$ was set to 95 % for the low refractive index (N-rich) and to 53 % for high refractive index (Si-rich) a-$Si_{1-x}N_x$:H layers. The refractive index and the thickness of layers were determined from calibration data obtained for homogeneous films by means of standard spectroscopic measurements. As seen in Figure 1, the 1DPC structure is composed of two segments S1 and S2 with periodic stack of high (Si-rich) and low (N-rich) refractive index (RI) layers. In the first segment S1 with four pairs of layers supporting BSWs, the thickness of high and low RI layers was set to t_{HBSW}=80 nm and t_{LBSW}=150 nm, respectively. The second segment S2 was designed to serve as a Bragg mirror and the thickness of high and low RI layers was set to t_{HBragg}=65 nm and t_{LBragg}=107 nm, respectively.

Figure 1

2.3 Functionalization of sensor chip

For a model immunoassay experiment, two types of sensor chips were modified with capture antibodies. Firstly, a thin SU-8 with the thickness of t_{SU8}=6.5 nm was deposited on the 1DPC sensor chip and on the reference bare glass substrate by spin coating 3 vol. % solution. Then, NIPAAm-based hydrogel film was attached to SU-8 surface based on the protocol reported previously [17] in order to serve as a three-dimensional binding matrix. Briefly, NIPAAm-based polymer was dissolved in ethanol (concentration of 4 mg/mL) and spincoated on the SU-8 linker layer. After drying overnight, the hydrogel layer was exposed to UV light (an irradiation dose of 5 J/cm^2 at a wavelength of λ=365 nm) in order to photocrosslink and attach polymer chains to the sensor chip by reacting with benzophenon groups. Then, the hydrogel film was swollen in ACT buffer and *in situ* functionalized with capture mIgG antibodies. The carboxylic groups in the gel were activated by the incubation with a mixture of EDC and TFPS, followed by the covalent coupling of mIgG dissolved in ACT buffer via their amine moieties [18]. Finally, unreacted active ester groups of the hydrogel were passivated by the incubation in ethanolamine solution. The thickness of dry NIPAAm-based layer of 16 nm was measured by surface plasmon resonance. Based on our previous studies [17], we assumed that its thickness increases by a factor of ~9 to reach t_{HG}~150 nm and its refractive index n_{HG}=1.35 becomes close to that of water after swelling in PBS-T buffer.

2.4 Optical setup

In experiments, an optical setup based on the angular interrogation and attenuated total reflection (ATR) was employed (described previously in more detail [19]). As depicted in Figure 2, He-Ne laser beam at the excitation wavelength λ_{ex}=633 nm (that is close the absorption band of the used fluorophore label λ_{ab}=650 nm) was launched to a 90° glass prism with a sensor chip optically matched to the chip at its base. The angle of incidence of the laser beam θ (defined as the one in BK7 glass substrate) was controlled by a rotation stage. The

intensity of the laser beam reflected from the prism base was measured with a photodiode detector and a lock-in amplifier (Model 5210, Princeton Applied Research, USA). A transparent flow cell with the volume of approximately 10 μL was attached to the sensor surface in order to flow liquid samples with target molecules along the hydrogel binding matrix with the flow rate 0.503 mL/min by using a peristaltic pump (REGLO Digital MS-4/12, ISMATEC, Switzerland). Fluorescence light emitted into the aqueous medium from affinity captured molecules on the sensor surface was collected through the flow-cell with a lens (NA=0.3). The fluorescence intensity was measured in counts per second (cps) by a photomultiplier tube (H6240-01, Hamamatsu, Japan) which was connected to a counter (53131A, Agilent, USA). A set of filters including notch (XNF-632.8-25.0M, CVI Melles Griot, Germany) and band-pass (670FS10-25, LOT-Oriel, Germany) filters were used in order to suppress the background signal outside the emission wavelength λ_{em}=670 nm.

Figure 2

For the observation of dispersion relation of BSW supported by 1DPC, we measured the dependence of the reflectivity on the angle of incidence θ and wavelength λ. In this experiment, the HeNe laser was replaced with a halogen lamp (LSH102, LOT-Oriel, Germany) emitting a polychromatic light beam and a spectrometer (HR4000 from Ocean Optics, USA) was used for the analysis of its spectrum after reflecting from the sensor chip (for more details see our previous work [20]).

2.5 Modeling of 1DPC-mediated fluorescence

Chance-Prock-Silbey model [21] was implemented in Mathematica (Wolfram Research, UK) scripts for simulations of angular distribution of fluorescence emission. Fluorophores were

represented as an ensemble of randomly oriented dipoles located in the hydrogel matrix at certain distance D from the surface of 1DPC. The density of fluorescence intensity $F(\theta,\phi,D)d\theta sin(\theta)d\phi$ emitted to polar θ and azimuth ϕ angles (in aqueous superstrate and BK7 glass substrate) was calculated as described in our previous work [22]. Based on the simulated distance-dependent fluorescence emission density, we calculated the emission probability within a numerical aperture F_{NA} as:

$$F_{\mathrm{NA}}(D)=\frac{\int_{\theta\in \mathrm{NA}}\int_{\phi=0}^{2\pi} F(\theta,\phi,D)\sin(\theta)\,d\theta d\phi}{\int_{\theta=0}^{\pi}\int_{\phi=0}^{2\pi} F(\theta,\phi,D)\sin(\theta)\,d\theta d\phi}. \quad (1)$$

The average emission probability of fluorophores dispersed in a binding matrix with a thickness t_{HG} was obtained by integrating F_{NA}:

$$F_{\mathrm{HG}}=\frac{1}{t_{\mathrm{HG}}}\int_{0}^{t_{\mathrm{HG}}} F_{\mathrm{NA}}(D)\,dD. \quad (2)$$

Refractive indices of Si-rich layer of n_{H}=2.381+0.0013i and 2.403+0.0013i were used for the wavelength of λ_{em} and λ_{ex}, respectively. The refractive indices of N-rich layer n_{L}=1.784+0.0001i and 1.7844+0.0001i were used at the wavelength of λ_{em} and λ_{ex}, respectively. Refractive indices of BK7 glass n_{p}=1.51 and SU-8 film n_{SU8}=1.6 were assumed for both λ_{em} nm and λ_{ex}. Simulations of spatial distribution of electric field intensity $|\boldsymbol{E}|^2$ upon the coupling to BSW and the simulations of reflectivity from the multilayer stack were carried out by using home-developed Mathematica scripts that utilize transfer-matrix method.

3. Results and discussion

3.1 Theory - BSWs supported by 1DPC

In order to enhance the excitation rate of fluorophore labels, 1DPC was designed to increase the electric field intensity $|\boldsymbol{E}|^2$ on the sensor surface by the resonant excitation of BSW. The excitation of BSW at the wavelength λ_{ex} which is close to the absorption wavelength of adopted fluorophores λ_{ab} was used. Firstly, the dispersion relation of BSWs was studied through simulations of the reflectivity dependence on the angle of incidence θ and wavelength λ. Figure.3a reveals that the excitation of BSW (represented as a decrease in the reflectivity) occurs for transverse electric (TE) polarized light beam that is incident through the prism at wavelengths λ<670 nm and angles above the critical angle $\theta>\theta_c$=61 deg. For transverse magnetic (TM) polarization, no guided waves are observed above the critical angle θ_c. At angles below θ_c, the incident light beam is partially transmitted and the reflectivity is periodically modulated due the interference on the 1DPC layer stack. Figure 3b shows and an example of the field distribution of partially transmitted wave for the angle of incidence θ=51.4 deg and the wavelength λ_{ex}.

As seen in Figure.3b, strong electromagnetic field intensity is built up upon the resonant coupling to BSW on the top of 1DPC structure at the excitation wavelength λ_{ex} and angle of incidence θ=64.45 deg. The electric field intensity $|\boldsymbol{E}|^2$ was normalized with that of the incidence beam $|\boldsymbol{E_0}|^2$ and it peaks in vicinity to the interface between the 1DPC structure and the aqueous environment. The simulations predict that the full coupling to BSW can be achieved (coupling efficiency of 100 %) and the maximum electric field intensity enhancement reaches $|\boldsymbol{E}/\boldsymbol{E_0}|^2$~300. The resonant coupling to BSW is associated with extremely narrow resonance in the reflectivity spectrum exhibiting the angular width of

$\Delta\theta$=0.1 deg (see the cross-section in Figure 3a). The BSW evanescent field probes the aqueous medium on the top of 1DPC with the penetration depth $L_p/2$=166 nm (defined as the distance D at which the magnitude of electric field intensity $|\boldsymbol{E}/\boldsymbol{E_0}|^2$ decreases by a factor of 1/e) that is comparable to the thickness of the attached hydrogel binding matrix t_{HG}~150 nm. For comparison, the electric field intensity distribution was calculated for the total internal reflection at the surface between the bare glass substrate and aqueous medium (without the 1DPC layer structure). It shows that the maximum field intensity enhancement in vicinity to the critical angle θ_c reaches $|\boldsymbol{E}/\boldsymbol{E_0}|^2$~4 at the interface.

Figure.3

Let us note that (far from saturation) the excitation rate of fluorophore labels on the sensor surface is proportional to the electric field intensity $|\boldsymbol{E}|^2$ at the absorption wavelength λ_{ab} Therefore, the strong electromagnetic field intensity provided by the excitation of BSW on 1DPC is directly translated to the enhanced fluorescence signal. From the simulations above the fluorescence excitation rate is increased through the BSW excitation on 1DPC with respect to that for regular TIR by a factor of χ_{ex}~75 (defined as ratio of $|\boldsymbol{E}/\boldsymbol{E_0}|^2$ for the 1DPC and bare glass surfaces presented in Figure 3b).

3.2 Theory - Directional fluorescence emission mediated by1DPC

In general, the angular distribution of emitted fluorescence light intensity is altered when the emitted radiation couples with guided waves and an interference with waves back-reflected from the surface occurs [23]. Further, the design of 1DPC was carried out in order to maximize the fluorescence emission through the aqueous medium at the direction perpendicular to the surface. Firstly, 1DPC with the segment S1 was tuned not to support

BSWs at the emission wavelength λ_{em} (shown in Figure 3a). The reason is that BSWs can serve as an efficient fluorescence emission channel [24] leading to an unwanted leaking of the fluorescence light intensity into the substrate by reverse Kretschmann configuration. Secondly, an additional layer segment S2 was used in order to shape the angular distribution of emitted light towards the aqueous medium and suppress the emission intensity transmitted through the 1DPC at angles $\theta<\theta_c$. As Figure.1 shows, the element S2 was placed below the BSW-wave layer structure S1.

Further, we calculated the polar angular dependence of fluorescence intensity $F(\theta,\phi=0)$ emitted from a randomly oriented dipole located at the distance D=10 or 140 nm from the sensor surface. Figure 4 compares $F(\theta,\phi=0)$ for 1DPC structure with that obtained for a bare glass substrate in contact with aqueous medium. These data show that for the distance D=10 nm from the bare glass substrate, the majority of fluorescence intensity is emitted into the glass with characteristic lobes close to the critical angle θ_c. On the surface carrying 1DPC with the segment S1, the majority of light is also emitted into the glass but the emission at angles close to the critical angle θ_c is suppressed leading to small increase of the intensity emitted into the aqueous sample. After adding the additional segment S2, the intensity of light emitted into the substrate is strongly suppressed and directed towards the aqueous medium on the top. Depending on the distance of the emitter from the surface D, the emitted light that is back-reflected from the 1DPC structure gains different phase-shift. This leads to distance-dependent interference with the light directly emitted towards the aqueous environment and to the maximum intensity occurring at different polar angles. As illustrated in Figure 4, the maximum emission intensity is emitted perpendicular to the surface θ~180 deg at D=10 nm. When increasing the distance to D=140 nm, the altered phase shift leads to the vanishing of

fluorescence intensity emitted perpendicular to the surface θ=180 deg and to the maximum fluorescence intensity propagating to polar angles around θ=150 deg.

Figure 4

In the experimental setup, only light emitted to the numerical aperture NA=0.3 (polar angles above θ=167 deg) is collected and delivered to a detector. Based on the simulated distance-dependent angular distribution $F(\theta,\phi,D)$, we obtained the emission probability within the numerical aperture F_{NA} from equation (1). The results in Figure 5 show that the probability of emission into the desired numerical aperture oscillates with a period $\lambda_{em}/2n_s$ ~ 250 nm due to the interference with back-reflected wave. The maximum emission probability reaches F_{NA}=11 % for the 1DPC with both segments S1 and S2 and the distance D=10 nm. For the 1DPC without the segment S2, the maximum emission probability of F_{NA}=7 % occurs at the distance D=140 nm. On the bare glass surface, the maximum emission probability is of F_{NA}=4 % at the distance D=140 nm, which is about three-fold lower that for the 1DPC structure with S1 and S2 segments.

Figure 5

Further, we assumed that the fluorophore-labeled molecules is homogeneously distributed in the hydrogel binding matrix with the thickness of t_{HG}=150 nm. Therefore, the average emission probability F_{HG} from fluorophores homogeneously dispersed in the hydrogel matrix was obtained by integrating F_{NA}, which is described by equation (2). The calculated emission probability reaches F_{HG}=5.4 % for the 1DPC with S1 and S2 segments which is higher than that for the bare glass surface providing F_{HG}=3.2 %. The predicted moderate enhancement of

the collection efficiency by a factor of χ_{col}~1.7 (defined as the ratio of F_{HG} on 1DPC and bare glass substrate) is due to the rapid oscillation of the fluorescence emitted intensity with the distance *D*. The collection efficiency enhancement with a factor up to χ_{col}~4 can be achieved for a thinner binding matrix (e.g. for the immobilization of capture molecules by using monolayer-based surface architectures).

3.2 Experimental - Characterization of guided waves on 1DPC

Dispersion relation of BSW was measured on prepared 1DPC for TE and TM polarization. The results in Figure 6 are in good agreement with simulated spectrum of modes presented in Figure 3. Particularly, the measured dispersion relation shows that BSW mode is excited only for TE polarization bellow the wavelength λ<670 nm and no guided waves are supported for TM polarization. However, the measured coupling efficiency to BSW at the emission wavelength λ_{ex} is only 35 % which is almost three times lower than that predicted by simultations. In addition, the measured angular width of the resonance $\Delta\theta$=0.22 deg is significantly higher than seen in simulations. These observations are mainly due to the imperfections of prepared 1DPC layer stack and possible effect of roughness that was not taken into account in simulations. They lead to a lower the electromagnetic field intensity enhancement upon the resonant excitation of BSW. Based on the fitting of reflectivity spectra by using a transfer-matrix model (data not shown), we estimated the peak field intensity enhancement as $|\boldsymbol{E}/\boldsymbol{E_0}|^2$ ~ 20 which is about one order of magnitude lower than that simulated for the ideal structure. These data indicate that lower excitation enhancement factor of χ_{ex}~5 can be reached when comparing 1DPC with regular TIR on a bare glass surface.

Figure 6

3.3 Experimental - Model immunoassay experiment

Firstly, the angular reflectivity and fluorescence spectrum was measured from 1DPC and bare glass sensor chips carrying the hydrogel matrix. The hydrogel matrix was functionalized with the capture mIgG molecules in order to specifically bind fluorophore-labeled a-mIgG. Figure 7 shows that the coupling to BSW on 1DPC surface is manifested as a resonant dip at the angle of incidence θ=63.21 deg. The resonance shifts to higher angles after the immobilization of mIgG molecules due to the associated increase of the refractive index n_H. On the bare glass surface, no significant changes can be seen in the TIR angular spectrum before and after the coupling of mIgG molecules. After the affinity binding of fluorophore-labeled a-mIgG molecules, fluorescence intensity $F(\theta)$ was measured as a function of the angle of incidence. For the 1DPC, a narrow peak occurs in $F(\theta)$ at the resonance angle where the electric field intensity is enhanced by BSW. In contrast, the fluorescence intensity peaks at the critical angle θ=61.7 deg and gradually decreases when increasing the angle of incidence for the reference bare glass surface.

Figure 7

In order to evaluate the potential of proposed 1DPC-based biosensor for sensitive detection of molecular analytes, a titration experiment was carried out. For 1DPC, the incident angle of excitation laser beam (λ_{ex}=633 nm) was fixed at the BSW resonance θ=63.29 deg and the fluorescence signal F was measured in time upon the sequential flow of samples with a-mIgG molecules. The same angle of incidence was used for the TIRF readout on the reference bare glass sample. Samples with increasing concentration of a-mIgG molecules dissolved in PBS-T were successively flowed along the sensor surface in order to bind to the surface. For 1DPC chip, the a-mIgG concentration between 0.3 pM and 1 nM was used. For bare glass sensor

chip, the analyte concentration was varied between 10 pM and 10 nM. Each sample was flowed over the surface with mIgG-functionalized hydrogel binding matrix for 10 min followed by 10 min rinsing with PBST. The obtained sensorgrams in Figure 8 shows that the affinity binding of a-mIgG molecules is accompanied with a gradual increase in the fluorescence signal. A slow exponential decrease of the fluorescence intensity was measured due to the dissociation of a-mIgG during the rinsing step.

Figure 8

Calibration curves presented in Figure 9 were obtained from measured fluorescence kinetics $F(t)$ on 1DPC and bare glass sensor chips. The response for each association phase of the binding was fitted by a linear function, the slope $\Delta F/\Delta t$ was determined, and plotted as a function of the concentration of a-mIgG. The measurements were carried out in triplicate and the averaged calibration curves are shown with the error bars representing the standard deviation. Let us note that this error arises due to the chip to chip variability and inaccuracy in incubation times. The limit of detection (LOD) was determined as the concentration at which the linear fit of the calibration curve matches the 3-fold standard deviation of the fluorescence signal for a blank sample σ. For the 1DPC sensor chip the 3σ=149 cps/min was determined. This value is about 2.4 higher than that for the bare glass surface 3σ=62 cps/min which is due the higher background signal. This effect is probably associated with stronger auto-fluorescence and scattering of light at the excitation wavelength upon the resonant coupling to BSW (see Figure 7). The limit of detection of 2 pM was obtained for the 1DPC compared to 25 pM for the regular bare glass slide.

Figure 9

The presented experiments reveal that the employment of 1DPC allows enhancing the fluorescence intensity accompanied with the capture of target molecules on the sensor surface by a factor of 30 with respect to regular TIRF. This enhancement translates to the improved limit of detection for the immunoassay-based analysis of molecular analyte by a factor of 12.5 (let us note that deterioration by a factor of 2.4 is due to the increased background of fluorescence signal observed on 1DPC). These values are significantly lower than those predicted by simulations which show that combined enhancement of collection efficiency χ_{col}=1.7 and excitation rate χ_{ex}=75 of fluorescence light allows to increase the sensor sensitivity by a factor of $\chi_{col}\chi_{ex}$=127. The key reason for this discrepancy is the fact that the experimentally achieved field intensity enhancement χ_{ex}~5 is lower, which leads to the smaller factor $\chi_{ex}\chi_{col}$=8.5. Further discrepancies can be attributed to the inhomogeneous spatial distribution of captured a-mIgG in the binding matrix. From our previous works the affinity binding of molecules in functionalized NIPAAm-based hydrogel occurs at the distance of few hundreds of nanometers from its interface with aqueous sample [25]. However, the density of the hydrogel layer typically exhibits a gradient and the hydrogel is denser at the inner interface compared to that in contact with aqueous sample [16]. Therefore, the capture of target analyte probably occurred preferably at the inner part of the hydrogel for which the collecting efficiency of fluorescence signal is increased (see fluorescence angular emission distribution in Figure 4).

4. Conclusions

A one dimensional photonic crystal (1DPC) supporting Bloch surface waves and serving as a Bragg mirror was investigated for the enhancement of sensitivity in heterogeneous fluorescence assays for detection molecular analytes. 1DPC was designed to amplify the

intensity of fluorescence light emitted from fluorophore labels by the combination of enhanced excitation rate though strong electric field intensity of resonantly excited BSW and by shaping the angular distribution of emitted light towards a detector by a Bragg mirror. The theory predicts that this approach holds potential for increasing the sensitivity by more than two orders of magnitude with respect to regular TIRF on a bare glass slide. The experiments showed lower sensitivity enhancement of with a factor of 12.5, mainly due to the imperfection of prepared 1DPC. The future work will be devoted to further improve the design of 1DPC and towards the implementation of this detection principle to microarrays detections format.

Acknowledgements

Support for this work was partially provided by the Austrian NANO Initiative (FFG and BMVIT) through the NILPlasmonics project within the NILAustria cluster (www.NILAustria.at).

References

[1] D.A. Giljohann, C.A. Mirkin, Drivers of biodiagnostic development, Nature, 462 (2009) 461-464.

[2] O. Lazcka, F.J. Del Campo, F.X. Munoz, Pathogen detection: A perspective of traditional methods and biosensors, Biosens. Bioelectron., 22 (2007) 1205-1217.

[3] G.W. Ford, W.H. Weber, Electromagnetic interactions of molecules with metal surfaces, Physics Reports, 113 (1984) 195-287.

[4] V. Giannini, A.I. Fernandez-Dominguez, Y. Sonnefraud, T. Roschuk, R. Fernandez-Garcia, S.A. Maier, Controlling Light Localization and Light-Matter Interactions with Nanoplasmonics, Small, 6 (2011) 2498-2507.

[5] V. Giannini, A.I. Fernandez-Dominguez, S.C. Heck, S.A. Maier, Plasmonic Nanoantennas: Fundamentals and Their Use in Controlling the Radiative Properties of Nanoemitters, Chem. Rev., 111 (2011) 3888-3912.

[6] T. Neumann, M.L. Johansson, D. Kambhampati, W. Knoll, Surface-plasmon fluorescence spectroscopy, Adv Funct Mater, 12 (2002) 575-586.

[7] J. Dostalek, W. Knoll, Biosensors based on surface plasmon-enhanced fluorescence spectroscopy, Biointerphases, 3 (2008) Fd12-Fd22.

[8] J.R. Lakowicz, K. Ray, M. Chowdhury, H. Szmacinski, Y. Fu, J. Zhang, K. Nowaczyk, Plasmon-controlled fluorescence: a new paradigm in fluorescence spectroscopy, Analyst, 133 (2008) 1308-1346.

[9] M.F. Garcia-Parajo, Optical antennas focus in on biology, Nat. Photonics, 2 (2008) 201-203.

[10] E. Fort, S. Gresillon, Surface enhanced fluorescence, J. Phys. D-Appl. Phys., 41 (2008).

[11] V.N. Konopsky, E.V. Alieva, Long-range propagation of plasmon polaritons in a thin metal film on a one-dimensional photonic crystal surface, Phys. Rev. Lett., 97 (2006).

[12] W.M. Robertson, Experimental measurement of the effect of termination on surface electromagnetic waves in one-dimensional photonic bandgap arrays, Journal of lightwave technology, 17 (1999) 2013-2017.

[13] W.M. Robertson, M.S. May, Surface electromagnetic wave excitation on one-dimensional photonic band-gap arrays, Applied Physics Letters, 74 (1999) 1800-1800.

[14] M. Shinn, W.M. Robertson, Surface plasmon-like sensor based on surface electromagnetic waves in a photonic band-gap material, Sensors and Actuators B: Chemical, 105 (2005) 360-364.

[15] Y. Guo, J.Y. Ye, C. Divin, B. Huang, T.P. Thomas, J.R. Baker, T.B. Norris, Real-time biomolecular binding detection using a sensitive photonic crystal biosensor, Analytical Chemistry, 82 (2010) 5211-5218.

[16] P.W. Beines, I. Klosterkamp, B. Menges, U. Jonas, W. Knoll, Responsive thin hydrogel layers from photo-cross-linkable poly(N-isopropylacrylamide) terpolymers, Langmuir, 23 (2007) 2231-2238.

[17] Y. Wang, C.J. Huang, U. Jonas, J. Dostalek, W. Knoll, Biosensor based on Hydrogel Optical Waveguide Spectroscopy, Biosensors and Bioelectronics, 25 (2010) 1663-1668.

[18] A. Aulasevich, R.F. Roskamp, U. Jonas, B. Menges, J. Dostalek, W. Knoll, Optical Waveguide Spectroscopy for the Investigation of Protein-Funcionalized Hydrogel Films, Macromolecular Rapid Communications, 30 (2009) 872-877.

[19] J. Dostalek, A. Kasry, W. Knoll, Long range surface plasmons for observation of biomolecular binding events at metallic surfaces, Plasmonics, 2 (2007) 97-106.

[20] K. Toma, M. Toma, P. Adam, M. Vala, J. Homola, W. Knoll, J. Dostalek, Surface plasmon-coupled emission on plasmonic Bragg gratings, Optics Express, 20 (2012) 14042.

[21] R.R. Chance, A. Prock, R. Silbey, Molecular fluorescence and energy transfer near interfaces, Advances in Chemical Physics, (1978) 1-65.

[22] K. Toma, J. Dostalek, W. Knoll, Long range surface plasmon-coupled fluorescence emission for biosensor applications, Opt. Express, 19 (2011) 11090-11099.

[23] W.L. Barnes, Fluorescence near interfaces: the role of photonic mode density, J. Mod. Opt., 45 (1998) 661-699.

[24] M. Ballarini, F. Frascella, F. Michelotti, G. Digregorio, P. Rivolo, V. Paeder, V. Musi, F. Giorgis, E. Descrovi, Bloch surface waves-controlled emission of organic dyes grafted on a one-dimensional photonic crystal, Applied Physics Letters, 99.

[25] C.J. Huang, J. Dostalek, W. Knoll, Long range surface plasmon and hydrogel optical waveguide field-enhanced fluorescence biosensor with 3D hydrogel binding matrix: On the role of diffusion mass transfer, Biosens. Bioelectron., 26 (2010) 1425-1431.

Figure captions:

Figure 1 1DPC composed of periodic low (N-rich) and high (Si-rich) refractive index layers designed to support BSWs (S1) and serve as Bragg mirror (S2) with attached hydrogel binding matrix for the capture of target analyte.

Figure 2 Experimental setup for Bloch surface wave-enhanced fluorescence spectroscopy and TIRF-based biosensors.

Figure 3 a) Simulated dispersion relation of BSW on 1DPC for TE and TM polarization. b) Profiles of electric field intensity for the coupling to BSW on 1DPC [see (A) in the upper figure], for the wave transmitted below the critical angle [see (B) in the upper figure], and for totally internally reflected waves at a glass-water interface.

Figure 4 Angular distributions of fluorescence light intensity emitted from a randomly oriented dipole at the distance of D=10 and 140 nm from the surface. Substrates including 1DPC with segments S1 and S2 (black solid line), 1DPC with the segment S1 (green dash dot line), and a bare glass surface (red dash line) in contact with water were assumed.

Figure 5 Dependence of the probability of the fluorescence emission within the numerical aperture NA=0.3 above the sensor surface on the distance of a randomly oriented dipole from the sensor surface. Simulations shown for 1DPC with (black square) and without (green triangle) Bragg mirror segment S2, and for the reference bar glass surface (red circle).

Figure 6 Measured dispersion relation of BSW on 1DPC for TE and TM polarization.

Figure 7 Measured angular reflectivity and fluorescence intensity spectra for the sensor chip with bare hydrogel surface, after the covalent coupling of mIgG, and after the affinity binding of fluorophore-labeled a-mIgG. Data shown a) for the sensor chip carrying 1DPC and b) for the reference bare glass.

Figure 8 Titration experiment showing the fluorescence sensor signal upon the affinity binding of a-mIgG from a PBST samples to mIgG immobilized in the hydrogel binding matrix. Data shown a) for the sensor chip with 1DPC and b) for reference bare glass.

Figure 9 Comparison of calibration curves of the analysis of a-mIgG in PBST buffer by using immunoassays and fluorescence readout based on 1DPC-based amplification and b) for regular TIRF on bare glass slide. Calibration curves are fitted with a linear function and the baseline noise and LOD are clearly indicated.

Figure 1

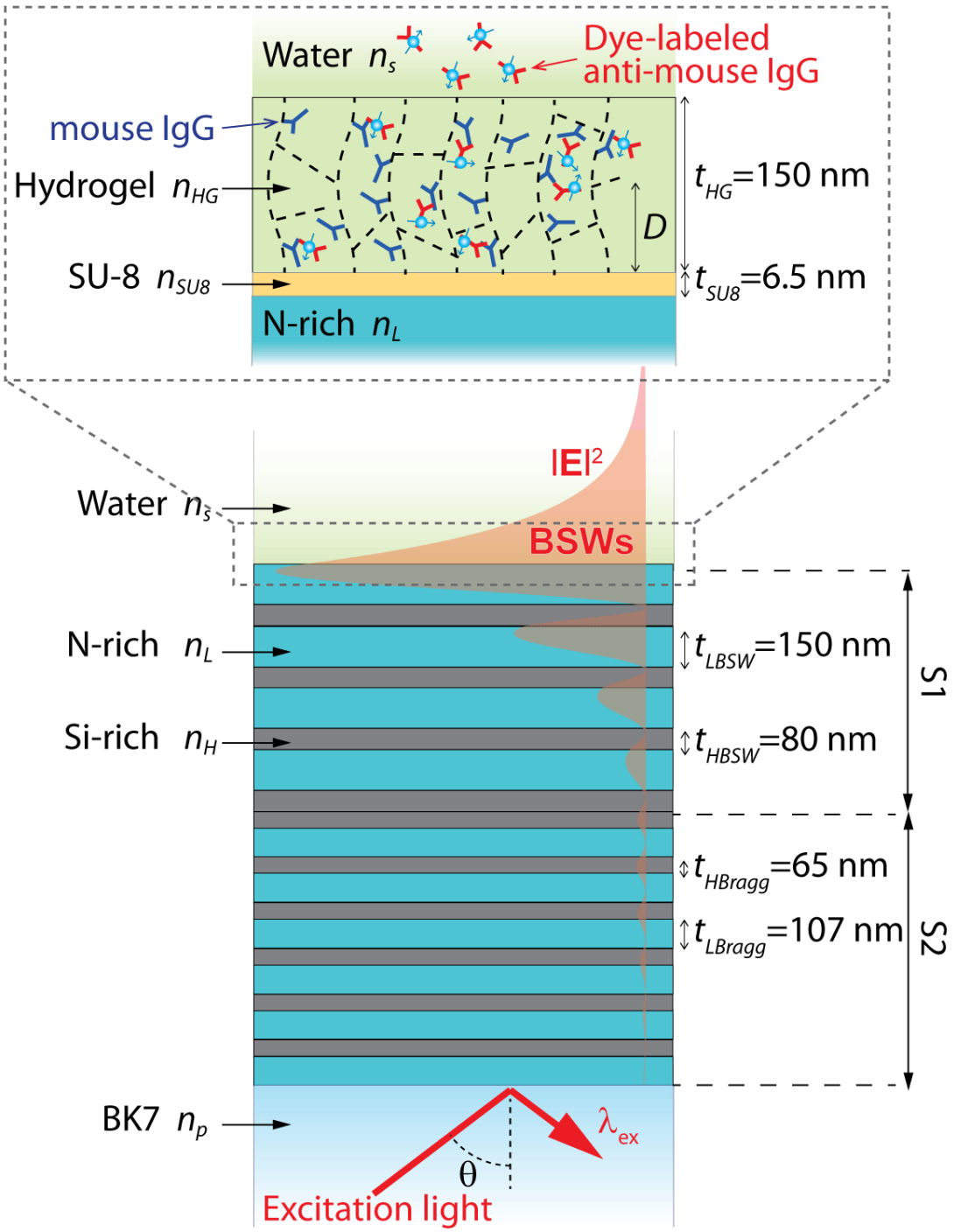
Water n_s
Dye-labeled anti-mouse IgG
mouse IgG
Hydrogel n_{HG}
SU-8 n_{SU8}
N-rich n_L
t_{HG}=150 nm
D
t_{SU8}=6.5 nm
|E|²
Water n_s
BSWs
N-rich n_L
Si-rich n_H
t_{LBSW}=150 nm
t_{HBSW}=80 nm
S1
t_{HBragg}=65 nm
t_{LBragg}=107 nm
S2
BK7 n_p
λ_{ex}
θ
Excitation light

Figure 2

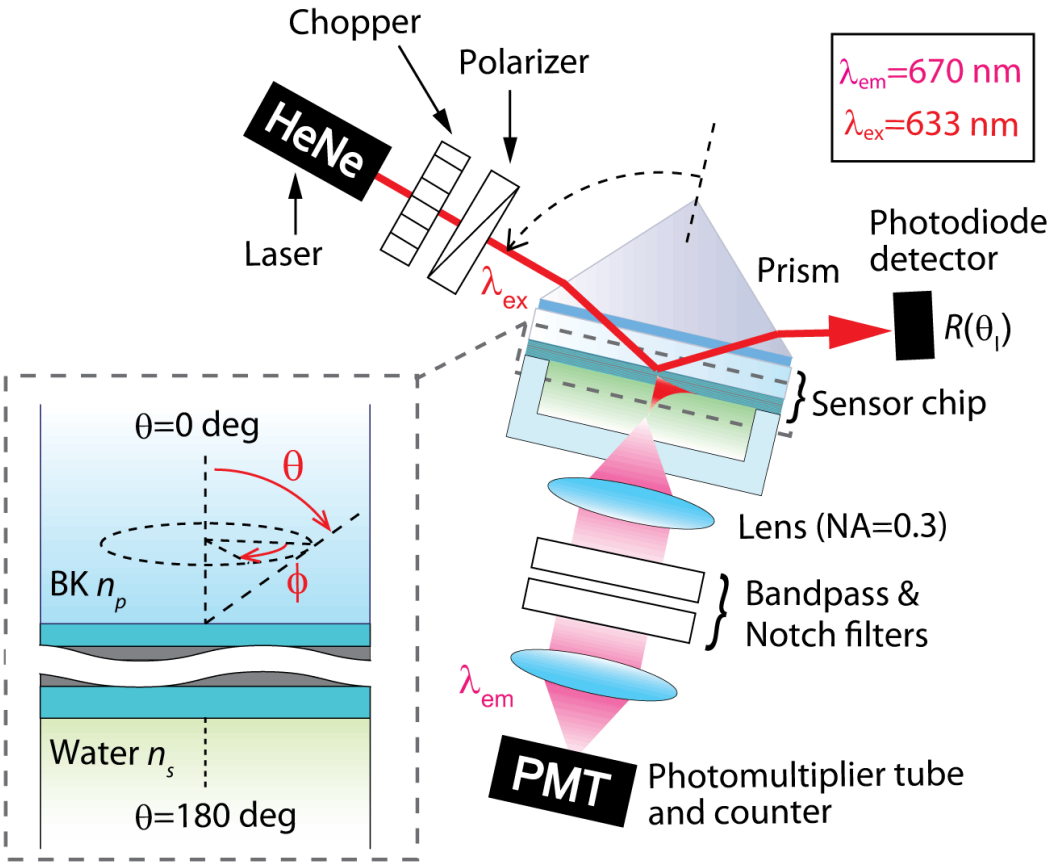
Chopper
Polarizer
HeNe
Laser
λem=670 nm
λex=633 nm
λex
Prism
Photodiode detector
R(θl)
Sensor chip
θ=0 deg
θ
ϕ
BK np
Water ns
θ=180 deg
Lens (NA=0.3)
Bandpass & Notch filters
λem
PMT
Photomultiplier tube and counter

Figure 3

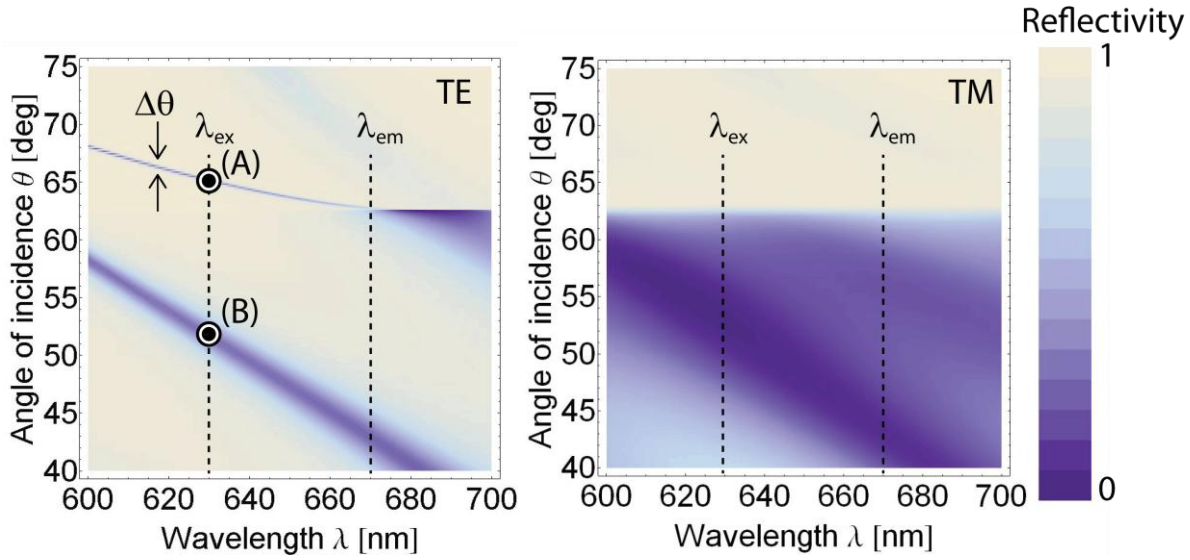
Reflectivity
1
0
TE
TM
Δθ
λex
λem
(A)
(B)
Angle of incidence θ [deg]
Wavelength λ [nm]
75
70
65
60
55
50
45
40
600
620
640
660
680
700

a)

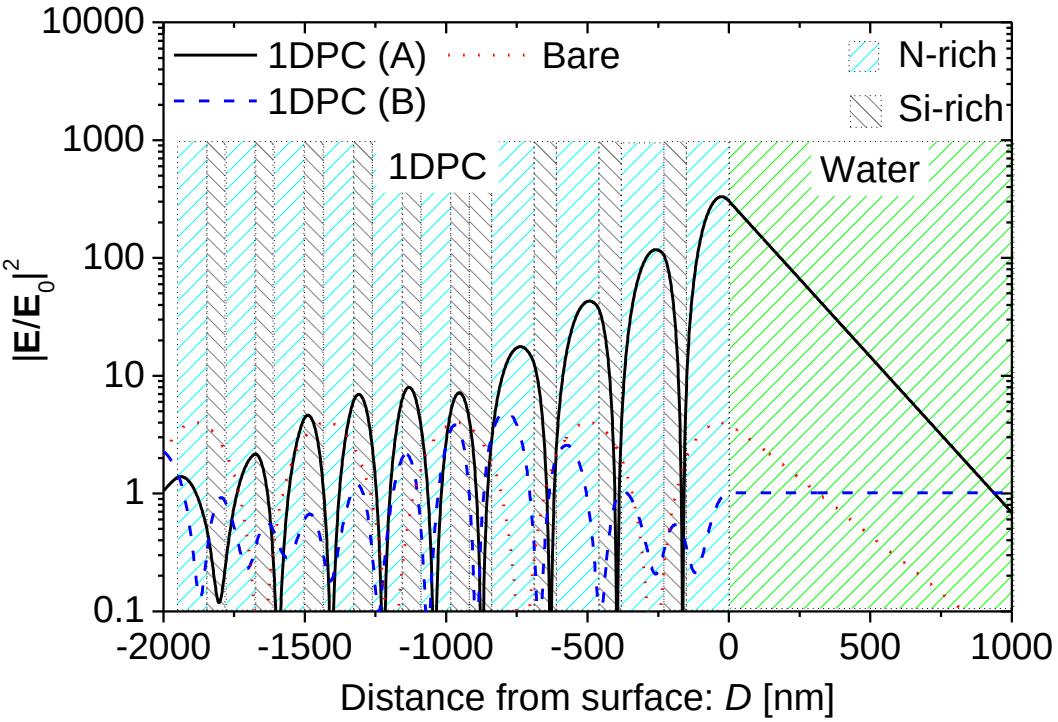
1DPC (A)
1DPC (B)
Bare
N-rich
Si-rich
1DPC
Water
|E/E0|2
Distance from surface: D [nm]
10000
1000
100
10
1
0.1
-2000
-1500
-1000
-500
0
500
1000

b)

Figure 4

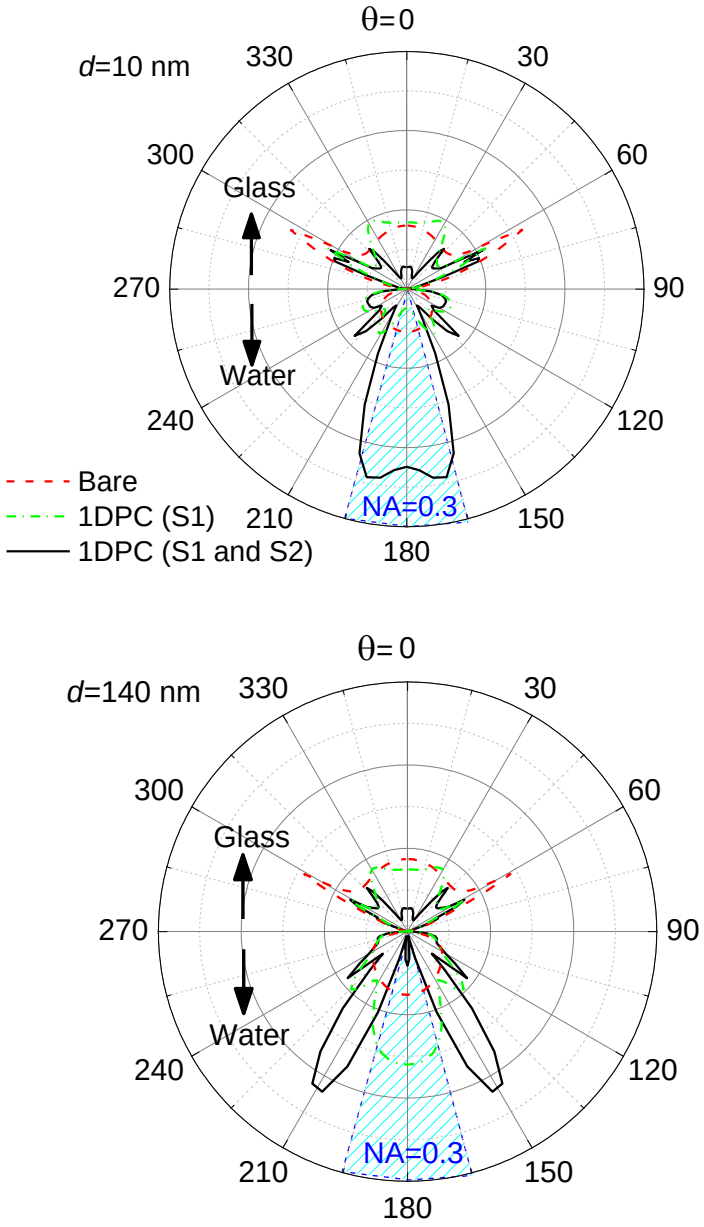
θ=0
d=10 nm
330
30
300
60
Glass
270
90
Water
240
120
NA=0.3
210
150
180
Bare
1DPC (S1)
1DPC (S1 and S2)
θ=0
d=140 nm
330
30
300
60
Glass
270
90
Water
240
120
NA=0.3
210
150
180

Figure 5

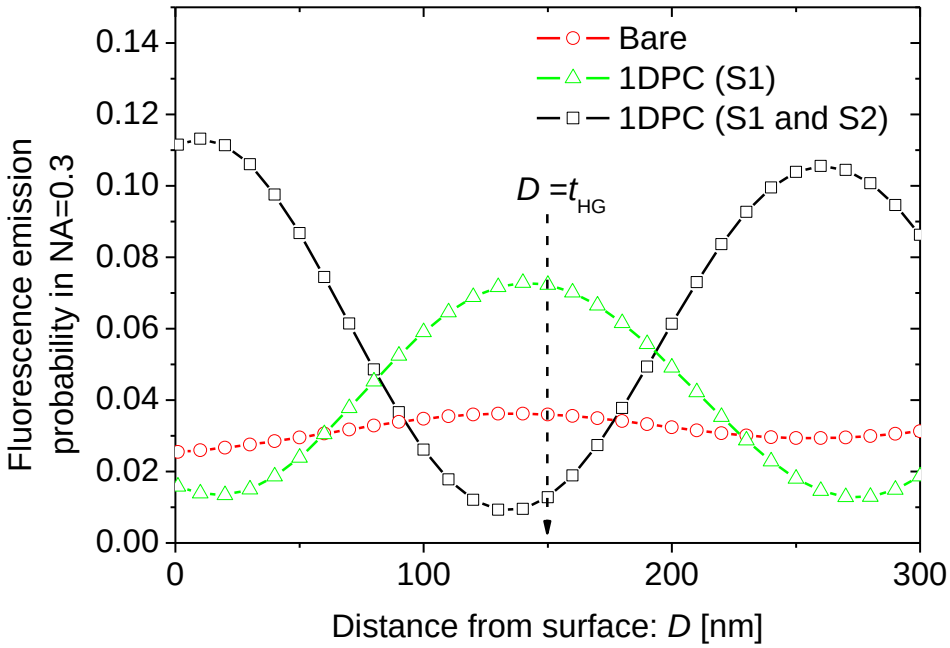
Bare
1DPC (S1)
1DPC (S1 and S2)
D =t_HG
Fluorescence emission probability in NA=0.3
Distance from surface: D [nm]
0.00
0.02
0.04
0.06
0.08
0.10
0.12
0.14
0
100
200
300

Figure 6

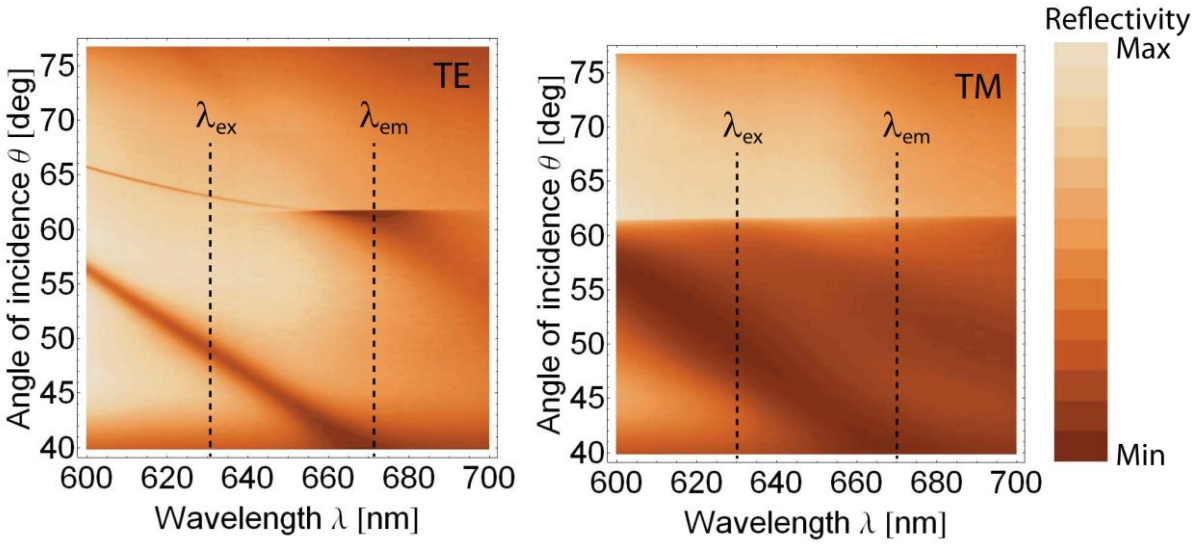
TE
TM
λ_{ex}
λ_{em}
Angle of incidence θ [deg]
Wavelength λ [nm]
75
70
65
60
55
50
45
40
600
620
640
660
680
700
Reflectivity
Max
Min

Figure 7

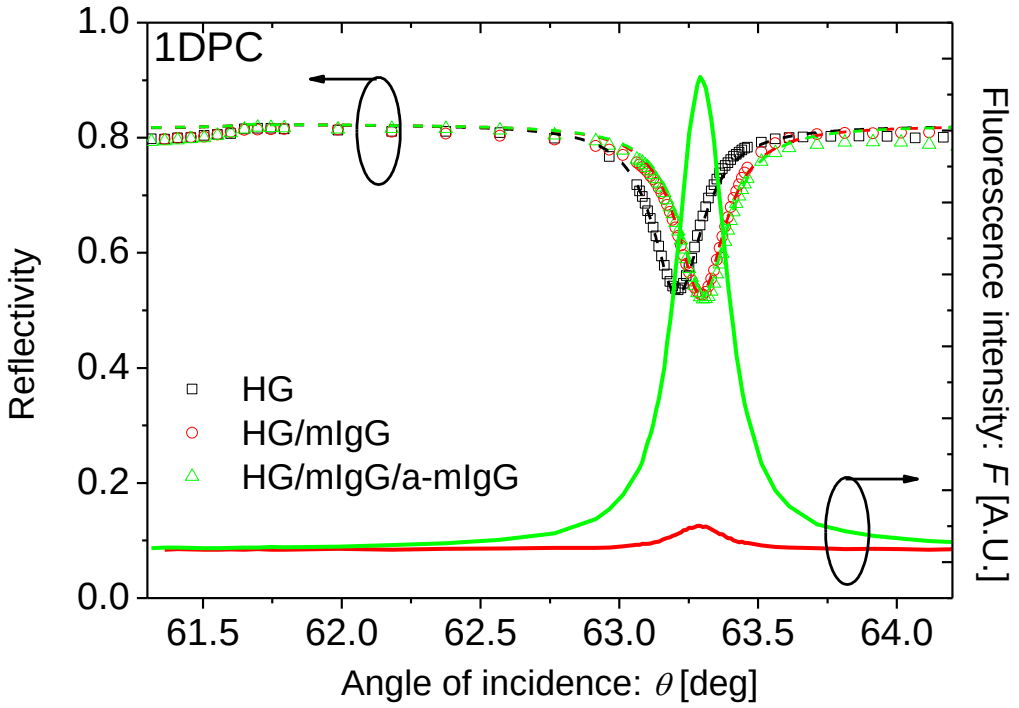
1DPC
Reflectivity
Fluorescence intensity: F [A.U.]
Angle of incidence: θ [deg]
HG
HG/mIgG
HG/mIgG/a-mIgG
1.0
0.8
0.6
0.4
0.2
0.0
61.5
62.0
62.5
63.0
63.5
64.0

a)

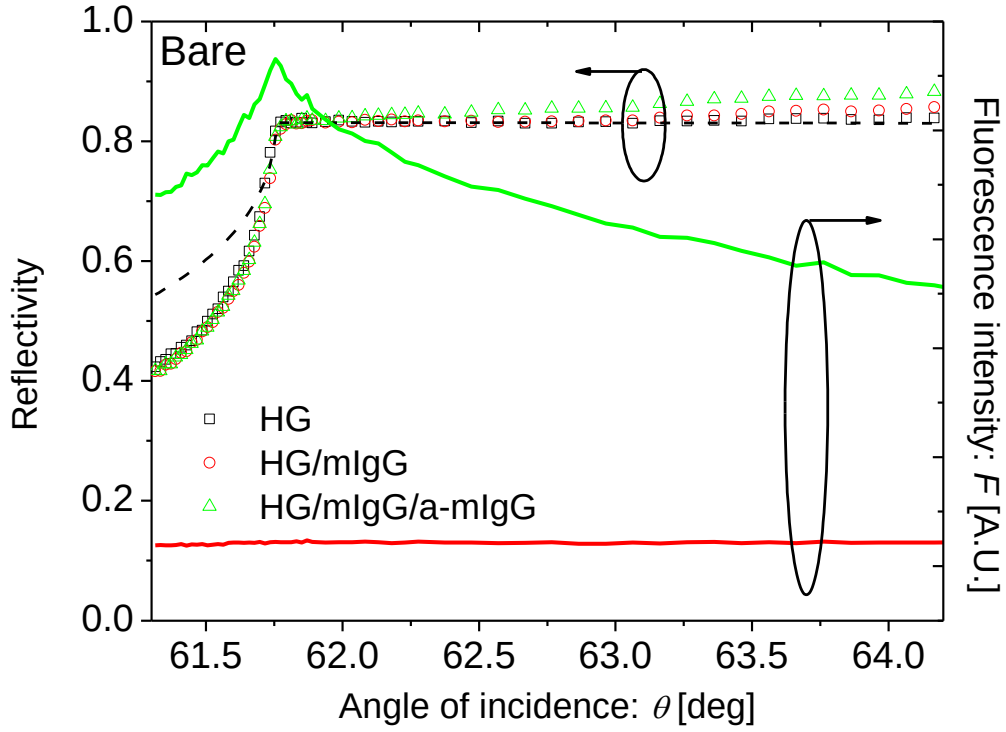
Bare
Reflectivity
Fluorescence intensity: F [A.U.]
Angle of incidence: θ [deg]
HG
HG/mIgG
HG/mIgG/a-mIgG
1.0
0.8
0.6
0.4
0.2
0.0
61.5
62.0
62.5
63.0
63.5
64.0

Figure 8

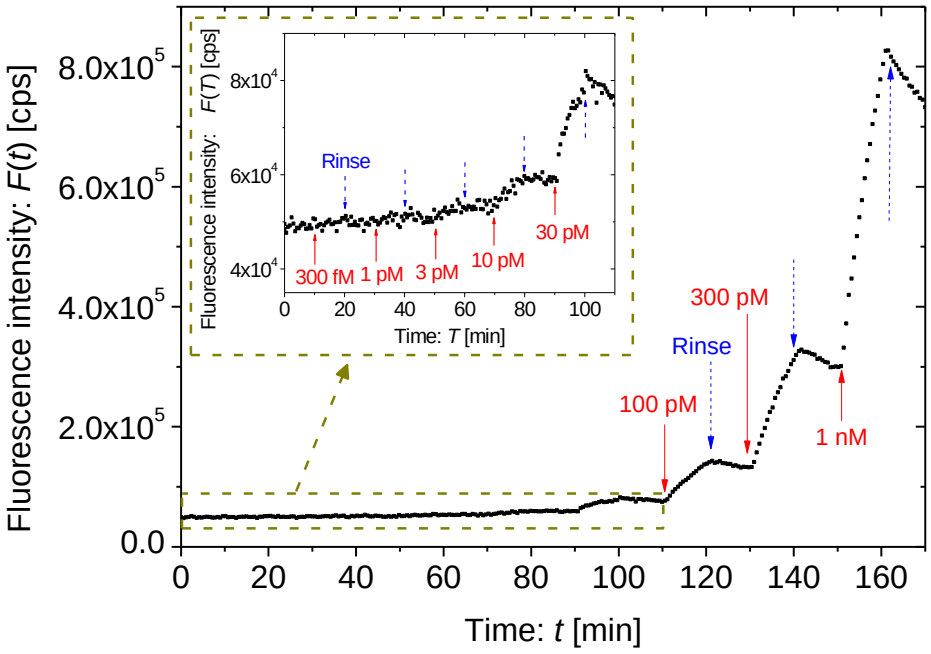
Fluorescence intensity: F(t) [cps]
8.0x10^5
6.0x10^5
4.0x10^5
2.0x10^5
0.0
0
20
40
60
80
100
120
140
160
Time: t [min]
Rinse
100 pM
300 pM
Rinse
1 nM
Fluorescence intensity: F(T) [cps]
8x10^4
6x10^4
4x10^4
Rinse
300 fM
1 pM
3 pM
10 pM
30 pM
0
20
40
60
80
100
Time: T [min]

a)

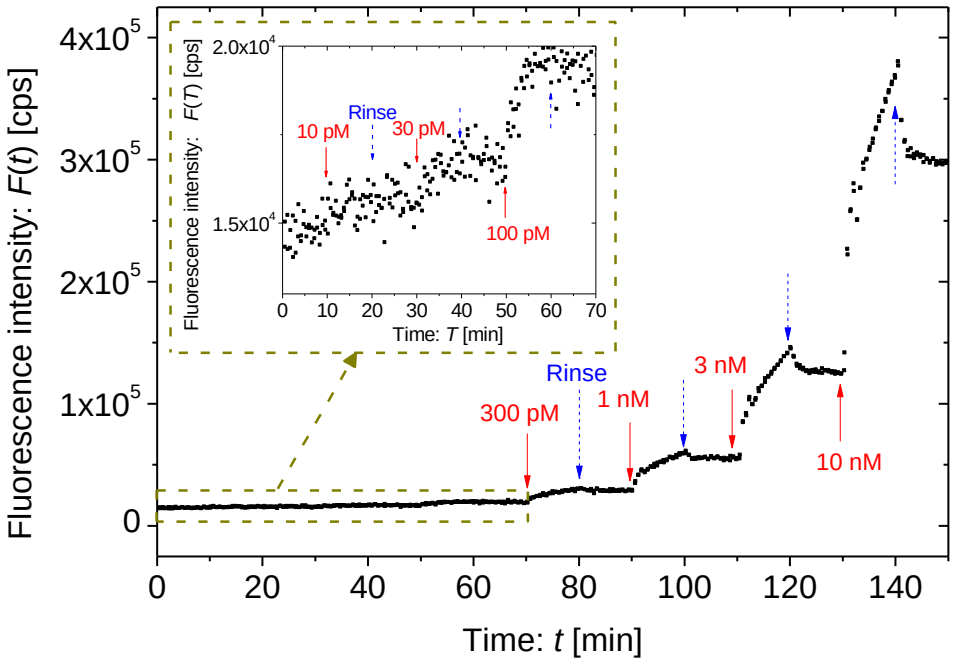
Fluorescence intensity: F(t) [cps]
4x10^5
3x10^5
2x10^5
1x10^5
0
0
20
40
60
80
100
120
140
Time: t [min]
Rinse
300 pM
1 nM
3 nM
10 nM
Fluorescence intensity: F(T) [cps]
2.0x10^4
1.5x10^4
Rinse
10 pM
30 pM
100 pM
0
10
20
30
40
50
60
70
Time: T [min]

b)

Figure 9

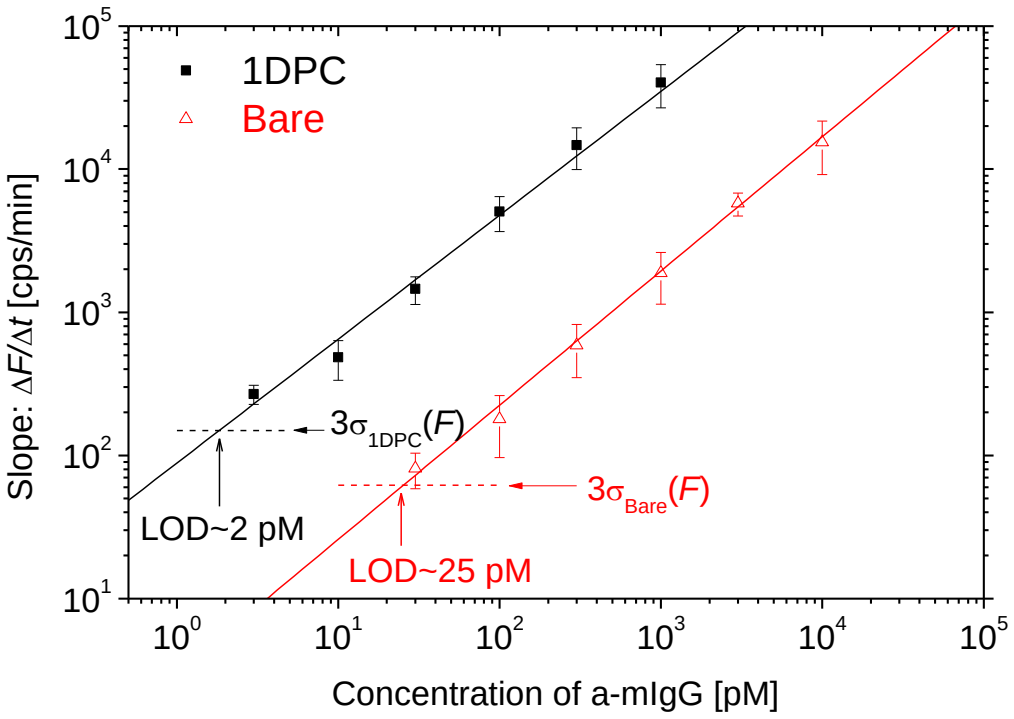
1DPC
Bare
$3\sigma_{1DPC}(F)$
$3\sigma_{Bare}(F)$
LOD~2 pM
LOD~25 pM
Slope: $\Delta F/\Delta t$ [cps/min]
Concentration of a-mIgG [pM]
10^0
10^1
10^2
10^3
10^4
10^5

Surface plasmon-coupled emission on plasmonic Bragg gratings

Mana Toma,[1,3] Koji Toma,[1,3] Pavel Adam,[2] Jiří Homola,[2] Wolfgang Knoll,[1] and Jakub Dostálek[1,*]

[1] *AIT - Austrian Institute of Technology GmbH, Muthgasse 11, 1190 Vienna, Austria*
[2] *Institute of Photonics and Electronics, Academy of Sciences CR, Chaberská 57, 18251 Prague, Czech Republic*
[3] *These authors contributed equally to this work*
[*] *jakub.dostalek@ait.ac.at*

Abstract: Surface plasmon-coupled emission (SPCE) from emitters in a close proximity to a plasmonic Bragg grating is investigated. In this study, the directional fluorescence emission mediated by Bragg-scattered surface plasmons and surface plasmons diffraction cross-coupled through a thin metallic film is observed by using the reverse Kretschmann configuration. We show that controlling of dispersion relation of these surface plasmon modes by tuning the refractive index at upper and lower interfaces of a dense sub-wavelength metallic grating enables selective reducing or increasing the intensity of the light emitted to certain directions. These observations may provide important leads for design of advanced plasmonic structures in applications areas of plasmon-enhanced fluorescence spectroscopy and nanoscale optical sources.

OCIS codes: (240.6680) Surface plasmons; (300.2530) Fluorescence, laser-induced; (050.1950) Diffraction gratings; (050.6624) Subwavelength structures.

References and links

1. H. Aouani, O. Mahboub, N. Bonod, E. Devaux, E. Popov, H. Rigneault, T. W. Ebbesen, and J. Wenger, "Bright unidirectional fluorescence emission of molecules in a nanoaperture with plasmonic corrugations," Nano Lett. **11**(2), 637–644 (2011).
2. L. Novotny and N. van Hulst, "Antennas for light," Nat. Photonics **5**(2), 83–90 (2011).
3. P. A. Hobson, S. Wedge, J. A. E. Wasey, I. Sage, and W. L. Barnes, "Surface plasmon mediated emission from organic light-emitting diodes," Adv. Mater. (Deerfield Beach Fla.) **14**(19), 1393–1396 (2002).
4. S. Wedge, A. Giannattasio, and W. L. Barnes, "Surface plasmon-polariton mediated emission of light from top-emitting organic light-emitting diode type structures," Org. Electron. **8**(2-3), 136–147 (2007).
5. T. Okamoto, J. Simonen, and S. Kawata, "Plasmonic crystal for efficient energy transfer from fluorescent molecules to long-range surface plasmons," Opt. Express **17**(10), 8294–8301 (2009).
6. J. R. Lakowicz, K. Ray, M. Chowdhury, H. Szmacinski, Y. Fu, J. Zhang, and K. Nowaczyk, "Plasmon-controlled fluorescence: a new paradigm in fluorescence spectroscopy," Analyst (Lond.) **133**(10), 1308–1346 (2008).
7. J. Dostálek and W. Knoll, "Biosensors based on surface plasmon-enhanced fluorescence spectroscopy," Biointerphases **3**(3), FD12–FD22 (2008).
8. W. L. Barnes, "Fluorescence near interfaces: the role of photonic mode density," J. Mod. Opt. **45**(4), 661–699 (1998).
9. G. W. Ford and W. H. Weber, "Electromagnetic interactions of molecules with metal surfaces," Phys. Rep. **113**(4), 195–287 (1984).
10. P. Andrew and W. L. Barnes, "Molecular fluorescence above metallic gratings," Phys. Rev. B **64**(12), 125405 (2001).
11. J. R. Lakowicz, J. Malicka, I. Gryczynski, and Z. Gryczynski, "Directional surface plasmon-coupled emission: a new method for high sensitivity detection," Biochem. Biophys. Res. Commun. **307**(3), 435–439 (2003).
12. W. Knoll, M. R. Philpott, and J. D. Swalen, "Emission of Light from Ag Metal Gratings Coated with Dye Monolayer Assemblies," J. Chem. Phys. **75**(10), 4795–4799 (1981).
13. R. M. Amos and W. L. Barnes, "Modification of spontaneous emission lifetimes in the presence of corrugated metallic surfaces," Phys. Rev. B **59**(11), 7708–7714 (1999).
14. K. Tawa, H. Hori, K. Kintaka, K. Kiyosue, Y. Tatsu, and J. Nishii, "Optical microscopic observation of fluorescence enhanced by grating-coupled surface plasmon resonance," Opt. Express **16**(13), 9781–9790 (2008).

#164156 - $15.00 USD Received 6 Mar 2012; revised 6 Apr 2012; accepted 15 May 2012; published 11 Jun 2012

15. S. C. Kitson, W. L. Barnes, and J. R. Sambles, "Surface-Plasmon Energy Gaps and Photoluminescence," Phys. Rev. B Condens. Matter **52**(15), 11441–11445 (1995).
16. M. Kreiter, S. Mittler, W. Knoll, and J. R. Sambles, "Surface plasmon-related resonances on deep and asymmetric gold gratings," Phys. Rev. B **65**(12), 125415 (2002).
17. S. Wedge and W. L. Barnes, "Surface plasmon-polariton mediated light emission through thin metal films," Opt. Express **12**(16), 3673–3685 (2004).
18. W. H. Weber and C. F. Eagen, "Energy transfer from an excited dye molecule to the surface plasmons of an adjacent metal," Opt. Lett. **4**(8), 236–238 (1979).
19. E. Matveeva, J. Malicka, I. Gryczynski, Z. Gryczynski, and J. R. Lakowicz, "Multi-wavelength immunoassays using surface plasmon-coupled emission," Biochem. Biophys. Res. Commun. **313**(3), 721–726 (2004).
20. K. Toma, J. Dostalek, and W. Knoll, "Long range surface plasmon-coupled fluorescence emission for biosensor applications," Opt. Express **19**(12), 11090–11099 (2011).
21. Y. Wang, J. Dostalek, and W. Knoll, "Magnetic nanoparticle-enhanced biosensor based on grating-coupled surface plasmon resonance," Anal. Chem. **83**(16), 6202–6207 (2011).
22. E. Kretschmann, "Die Bestimmung optischer Konstanten von Metallen durch Anregung von Oberflächenplasmaschwingungen," Z. Phys. **241**(4), 313–324 (1971).
23. E. D. Palik, *Handbook of Optical Constants of Solids* (Elsevier, 1998).
24. W. L. Barnes, T. W. Preist, S. C. Kitson, and J. R. Sambles, "Physical origin of photonic energy gaps in the propagation of surface plasmons on gratings," Phys. Rev. B Condens. Matter **54**(9), 6227–6244 (1996).
25. F. Romanato, L. Hong, H. K. Kang, C. C. Wong, Y. Zong, and W. Knoll, "Azimuthal dispersion and energy mode condensation of grating-coupled surface plasmon polaritons," Phys. Rev. B **77**(24), 245435 (2008).

1. Introduction

Surface plasmon-coupled emission (SPCE) is of great interest in various areas including nanoscale optical antennas [1, 2], organic light-emitting diodes [3, 4], dye lasers [5] and fluorescence spectroscopy [6, 7]. Surface plasmons (SPs) are electromagnetic waves which originate from collective oscillations of charge density at metallic surfaces. SPs exhibit tightly confined field profile which is associated with greatly enhanced photonic mode density (PMD) and intensity of electromagnetic field at a metallic surface. Therefore, light radiated by emitters in the vicinity of a metal can be trapped by SPs and the coupling of absorption and emission dipoles of emitters with SPs dramatically alters their characteristics including the excitation rate, lifetime, and quantum yield [8, 9].

In order to convert energy emitted to SPs back to light waves propagating away from the metal, approaches utilizing diffraction gratings [10] and the reverse Kretschmann configuration of attenuated total reflection (ATR) method [11] were most commonly used. The employment of relief diffraction gratings for the extraction of fluorescence light from a metallic surface was firstly reported by Knoll et al. [12]. In this and later experiments, the corrugated metallic surfaces with the period comparable with the wavelength were typically used in studies including plasmon-mediated emission decay kinetics [13], angular distribution of emitted light [14], and emitted wavelength spectrum [15]. These investigations were carried out for gratings supporting regular SPs as well as coupled surface plasmon modes including Bragg-scattered surface plasmons [15, 16] and long range and short range surface plasmons on thin metallic films in refractive index symmetrical geometry [5, 17]. Relief gratings with non-sinusoidal profile allow additional control of the interaction strength between emitters and SPs through surface plasmon Bragg-scattering and associated bandgap occurring in their dispersion relation [5, 15]. The surface plasmon bandgap was shown to decrease the intensity of fluorescence light emitted via surface plasmons [15] which was, for instance, proposed for selective cancelling of spontaneous emission in plasmonic lasers [5]. In addition, Bragg-scattered surface plasmons were investigated for spatially controlled photobleaching of dyes [16]. In the other common optical platform of SPCE utilizing reverse Krestchmann configuration of ATR, a thin metal layer on a flat high refractive index substrate is used. The light emission occurs via surface plasmons that are leaky into the substrate forms a characteristic SPCE cone propagating away from the metal film [18, 19]. The polar angle of the cone is defined by the surface plasmon resonance (SPR) condition and it depends on the wavelength [19]. The width of the SPCE cone depends on the losses of surface plasmons and it can be strongly decreased by using long-range surface plasmons [20].

#164156 - $15.00 USD Received 6 Mar 2012; revised 6 Apr 2012; accepted 15 May 2012; published 11 Jun 2012

In this paper, we extend studies in surface plasmon-coupled emission on structures that combine the reverse Kretschmann configuration of ATR and dense sub-wavelength metallic gratings. These gratings carry a thin metallic film and are designed to alter dispersion relation of surface plasmon modes by Bragg-scattering on individual metal interfaces as well as by diffraction cross-coupling of SPs through the metal film. We show that these modes can be engineered to efficiently collect the fluorescence light from emitters on the top of the metal film and direct the emission to specific azimuth and polar directions into high refractive index substrate below the metallic film. The used dense sub-wavelength diffraction gratings do not couple the fluorescence light to the medium above the metal film.

2. Materials and methods

2.1 Materials

Photoresist Microposit S1818-G2 was purchased from Micro Resist Technology GmbH (Germany). Metal ion containing developer AZ 303 was obtained from MicroChemicals GmbH (Germany). Polydimethylsiloxane (PDMS) prepolymer and its curing agent were from Dow Corning (SYLGARD® 184). Amonil MMS10 was purchased from AMO GmbH (Germany). Poly(methyl methacrylate) (PMMA) was from Sigma-Aldrich Handels (Austria) and 1,1'-dioctadecyl-3,3,3′,3′-tetramethylindodicarbocyanine, 4 chlorobenzene-sulfonate salt (DiD) were from Invitrogen (LifeTech Austria). DiD dye exhibits the absorption and emission wavelengths of λ_{ab} = 644 nm and λ_{em} = 665 nm, respectively, and it was dispersed at the concentration of 700 nM in a toluene with dissolved PMMA (1.4 wt.%).

2.2 UV-NIL preparation of relief gratings

Holography was used for the preparation of master gratings. A polished Schott SF2 glass substrate with spin-coated photoresist layer was exposed to the interference field of two coherent collimated beams emitted from a HeCd laser at the wavelength λ = 325 nm (IK3031R-C, Kimmon Koha, Japan). Afterwards, the gratings were etched with a developer AZ-303 diluted with distilled water (volume ratio 1:9), rinsed with water and dried. Master gratings with sinusoidal relief modulation period Λ = 225-230 nm and depths of d = 10 and 30 nm were prepared and characterized by atomic force microscopy (data not shown). UV-nanoimprint lithography was used to replicate the master gratings as we described previously [21]. Briefly, a relief master grating was casted to a PDMS stamp which was cured overnight at 60 °C. Afterwards, the PDMS stamp was detached from the master and placed onto about 100 nm thick layer of UV-curable polymer Amonil that was spin-coated on a glass substrate. Amonil film in contact with the PDMS stamp was crosslinked by UV light dose of 36 J/cm^2 at a wavelength of λ = 365 nm (Bio-Link 365, Vilber Lourmat, Germany) followed by the release of the PDMS stamp from cured replica grating.

2.3 Layer structures supporting surface plasmons

LaSFN9 glass (refractive index of n_1 = 1.84 at λ_{em}) and BK7 glass (refractive index of n_1 = 1.51 at λ_{em}) substrates with Amonil grating (refractive index of n_2 = 1.51 at λ_{em}) were successively coated by layers supporting surface plasmons and containing DiD dye, see Fig. 1. Firstly, Ta_2O_5 (refractive index of n_3 = 1.79 at λ_{em}) and gold (refractive index n_4 = 0.167 + 3.91i at λ_{em}) films were deposited on the Amonil surface by using magnetron sputtering (UNIVEX 450C, Leybold Systems, Germany). The thickness of the gold film was set to 47 nm which is close to that providing the maximum strength of the coupling between surface plasmons and propagating waves in the glass substrate based on the Kretschmann configuration [22]. Afterwards, a 40 nm thick PMMA film (refractive index n_5 = 1.49 at λ_{em}) doped with DiD dyes was spin-coated on the gold surface and dried overnight at the room temperature. The PMMA surface was brought in contact with water (refractive index n_6 = 1.33 at λ_{em}) or air (refractive index n_6 = 1 at λ_{em}) in order to tune the propagation constant of

#164156 - $15.00 USD Received 6 Mar 2012; revised 6 Apr 2012; accepted 15 May 2012; published 11 Jun 2012

surface plasmons at the outer metal surface (SP_{outer}). The propagation constant of surface plasmons on the inner metallic surface (SP_{inner}) was varied by tuning the thickness of Ta_2O_5 layer t_3. Let us note that the Ta_2O_5 layer was deposited only on the LaSFN9 glass substrates with Amonil grating.

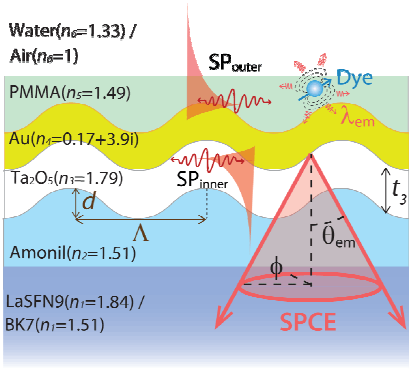

Fig. 1. Diffraction grating supporting surface plasmons that serve as emission channels for DiD dyes dispersed in a PMMA layer. Refractive indices of layers at the wavelength λ_{em} = 670 nm are shown for each layer.

3. Optical setup

Dispersion relation of surface plasmon modes on metallic grating surfaces was observed from angular reflectivity spectra R measured as a function of angle of incidence θ_I and wavelength λ. As seen in Fig. 2(a), a setup based on attenuated total reflection (ATR) method with Kretschmann configuration was used. A polychromatic beam from a halogen lamp (LSH102, LOT-Oriel, Germany) was coupled into an optical fiber (M25L02, Thorlabs, Germany), colimated with a lens (14 KLA 001, fl = 60 mm, CVI Melles Griot, Germany) and launched to a 90° glass prism that was made of identical glass as the grating sample substrate. At the prism base, the sample with a metallic grating was optically matched with a defined azimuth angle ϕ between the plane of incidence and grating vector **G**. The reflected light beam was coupled to an optical fiber and analyzed with a spectrometer (HR4000, Ocean Optics, USA). The prism and detectors were mounted on a two-circle rotation stage (Huber GmbH, Germany) in order to control the angle of incidence θ_I of the polychromatic beam in the prism. The data aquisition and control of the setup were supported by a home-built LabVIEW-based software. The reflectivity R was measured for transverse magnetic polarized incident beam (TM) and normalized with that measured for transverse electric polarization (TE).

#164156 - $15.00 USD Received 6 Mar 2012; revised 6 Apr 2012; accepted 15 May 2012; published 11 Jun 2012

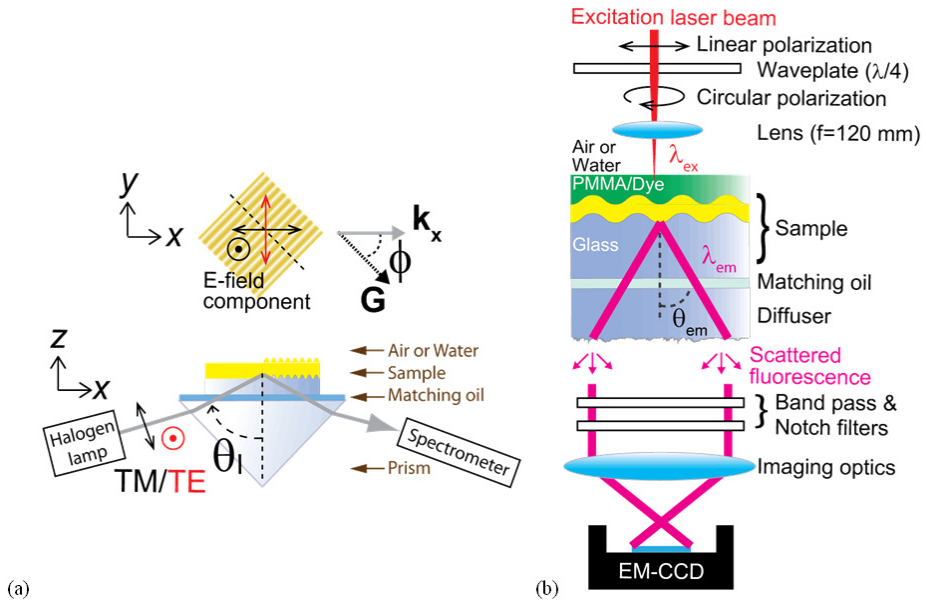

Fig. 2. Optical setup used for the measurement of (a) reflectivity spectra R as a function of angle of incidence θ_I, polar angle ϕ, and wavelength λ and (b) spatial distribution of surface plasmon-coupled emission in the glass substrate.

The measurement of spatial distribution of fluorescence intensity F emitted via surface plasmons into a glass substrate was carried out by using the setup depicted in Fig. 2(b). A sample with a metallic grating carrying a PMMA layer doped with a DiD dye was optically matched to a diffuser with rough bottom interface. Linearly polarized HeNe laser beam with the wavelength of λ = 632.8 nm that is close to the absorption wavelength of DiD dye λ_{ab} = 644 nm was circularly polarized by a quater waveplate (WPMQ05M-633, Thorlabs, Germany) and focused with a lens on the area of the surface of the structure with a diameter of about 100 μm. The fluorescence light coupled to surface plasmon modes at the emission wavelength λ_{em} of DiD dyes was re-radiated through the metal film based on the reverse Kretschamnn configuration, propagated through the substrate, and was scattered at the rough bottom surface of a diffuser made of LaSFN9 or BK7 glass. The spatial distribution of scattered fluorescence light was imaged onto an electron multiplying charge-coupled device (EM-CCD iXon + 885, Andor Technology, Ireland) by a camera lens (UNIFOC 58, Schneider Kreuznach, Germany). A set of filters including notch filter (XNF-632.8-25.0M, CVI Melles Griot, Germany) and band-pass filter (670FS10-25, LOT-Oriel, Germany) was used to reduce the background signal originating from the scattered and transmitted light at the excitation wavelength. The dependence of fluorescence signal on the polar angle θ_{em} in the glass substrate and azimuth angle ϕ was obtained from aquired fluorescence images. The central part of the image where the incident laser beam partially transmitted through the metal film was cut out by image processing as used filters did not suppress it totally.

4. Results and discussion

4.1 Surface plasmon-coupled emission on flat surface

The Bragg grating depicted in Fig. 1 supports surface plasmons at inner and outer interfaces of the metallic film. These modes act as pathways for fluorescence emission from dyes dispersed in the PMMA layer on the top of the gold film. Based on the Chance, Prock, and Silbey (CPS) model [9], we calculated the average energy dissipation density $dP/dk_{//}$ from an ensemble of dyes represented as randomly oriented dipoles. The energy dissipation density

#164156 - $15.00 USD Received 6 Mar 2012; revised 6 Apr 2012; accepted 15 May 2012; published 11 Jun 2012

for homogenously distributed dipoles in PMMA layer with the thickness of 40 nm was obtained by the averaging over distance from the metal surface between 0 and 40 nm as described in our previous work [20]. These simulations were carried out for flat layers (modulation depth d = 0 nm) shown in Fig. 1 with refractive indices taken from literature [23]. The results presented in Fig. 3 show $dP/dk_{//}$ as a function of in-plane component of the propagation constant $k_{//}$ of optical waves emitted from a dipole. $k_{//}$ is normalized by the propagation constant in vacuum k_0. They reveal that the coupling of fluorescence to surface plasmons at inner interface SP_{inner} (with the magnitude of propagation constant $k_{SPinner}$ = $|\mathbf{k}_{SPinner}|$) and outer interface SP_{outer} (with the magnitude of propagation constant $k_{SPouter}$ = $|\mathbf{k}_{SPouter}|$) is manifested as two distinct peaks. The probability of the emission via surface plasmons at inner and outer interfaces was calculated by integrating the energy dissipation density $dP/dk_{//}$ across respective peaks. For the layer architecture with 100 nm thick Ta_2O_5 on LaSFN9 glass and refractive index of the upper medium of n_6 = 1.33, 54 and 7% of emission events occurred via SP_{outer} and SP_{inner}, respectively. The fluorescence emission probability via SP_{outer} and SP_{inner} was redistributed to 40 and 14%, respectively, on the layer architecture consisting of BK7 glass without Ta_2O_5 layer. For both geometries, the peak energy dissipation density for the outer surface plasmon SP_{outer} is higher than that for the inner surface plasmon SP_{inner} due to the stronger overlap of SP_{outer} field with PMMA layer containing DiD dyes. The peak energy dissipation density for SP_{inner} is higher for the layer structure with BK7 substrate without Ta_2O_5 layer because its magnitude of propagation constant $k_{SPinner}$ is lower and thus larger portion of its field is carried in the PMMA layer. The fluorescence signal emitted via outer surface plasmon SP_{outer} can be recovered by the reverse Kretschmann configuration of ATR while that emitted via the inner surface plasmons SP_{inner} requires other means – e.g. diffraction grating. These simulations take into account fluorescence quenching due to the coupling to surface lossy waves with large propagation constant [9] ($k_{//}$ from 0 to 15k_0 was assumed in the model). This coupling is highly dependent on the distance from the metal surface. The majority of emission events is quenched below a characteristics length of about 15 nm which is smaller than the thickness of PMMA layer with dispersed DiD dyes.

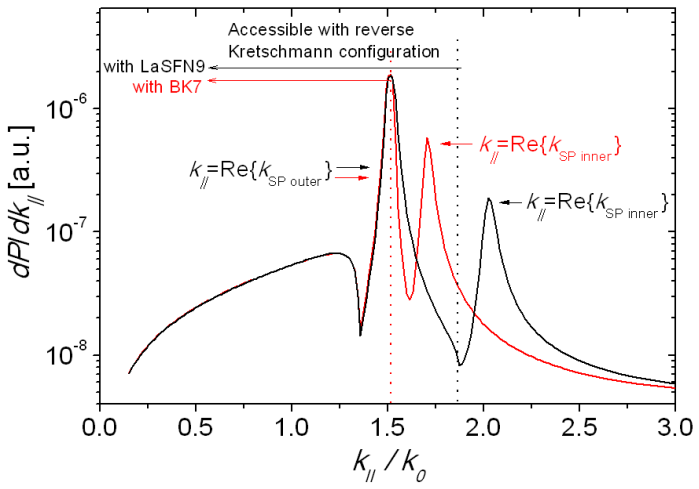

Fig. 3. Simulated average energy dissipation density $dP/dk_{//}$ of dyes dispersed in the 40 nm thick PMMA layer on the top of gold film with (t_3 = 100 nm, black line) or without (t_3 = 0 nm, red line) Ta_2O_5 layer. LaSFN9 (black line) and BK7 (red line) substrates were assumed. The PMMA layer is in contact with water (n_6 = 1.33).

4.2 Surface plasmon modes on corrugated metallic surfaces

On a corrugated layer structure, the characteristics of inner surface plasmons SP_{inner} and outer surface plasmons SP_{outer} are altered due to the interaction with the grating momentum $|\mathbf{G}|$ =

#164156 - $15.00 USD Received 6 Mar 2012; revised 6 Apr 2012; accepted 15 May 2012; published 11 Jun 2012

$2\pi/\Lambda$. In order to investigate changes in SP_{inner} and SP_{outer} modes, numerical simulations were carried out by using finite element method (FEM) implemented in a diffraction grating solver DiPoG (Weierstrass Institute, Germany). Figure 4(a) shows an example of the simulated dispersion relation of surface plasmon in the dependence of the reflectivity R on the angle of incidence θ_I and wavelength λ. For the grating structure with the modulation depth of d = 30 nm, Ta_2O_5 layer thickness of t_3 = 100 nm, and the refractive index of the upper medium n_6 = 1.33, the dispersion relation of SP_{outer} (at angles θ_I > 47 deg) is split in the vicinity to the wavelength of λ = 670 nm at which the grating momentum $\mathbf{G}$ matches the $2\mathbf{k}_{\mathbf{SPouter}}$. In this region, the counter-propagating SP_{outer} are Bragg scattered [24], which gives rise to a bandgap in their dispersion relation. At edges of the bandgap, Bragg-scattered surface plasmon modes (BSSPs) can be excited at wavelengths of λ = 630 nm and 730 nm. These SP_{outer} modes are referred as to ω^+ mode (λ = 630 nm) and ω^- mode (λ = 730 nm) and they exhibit electric field intensity localized at grating peaks (ω^-) and valleys (ω^+) as seen in Fig. 5(a) and 5(b), respectively. Let us note that the electric field intensity profiles are normalized with the maximum intensity $|\mathbf{E}_{\mathbf{max}}|^2$ to clarify the field distribution of considered plasmon modes. The increased PMD on the grating surface occurs at wavelengths where BSSPs can be excited as these modes are less dependent on the angle of incidence θ_I than regular surface plasmons, see Fig. 4. An additional resonance due to the −1st order diffraction grating coupling to surface plasmons at the inner surface of the gold film ($G\text{-}SP_{inner}$) is observed in Fig. 4(a). This resonance is associated with the field enhancement at the inner interface of the gold film as confirmed by the electric field intensity distribution presented in Fig. 5(c). $G\text{-}SP_{inner}$ resonance crosses over the SP_{outer} dispersion relation at wavelengths λ around 800 nm. When decreasing the thickness of Ta_2O_5 layer t_3, the momentum of SP_{inner} decreases and the resonance wavelength for the excitation of $G\text{-}SP_{inner}$ is blue-shifted. For the layer structure with Ta_2O_5 layer thickness of t_3 = 0 nm, $G\text{-}SP_{inner}$ resonance overlaps with the bandgap in SP_{outer} dispersion relation, see Fig. 4(b). The electric field intensity profile for $G\text{-}SP_{inner}$ inside the bandgap is presented in Fig. 5(d) and it shows this mode is partially coupled to SP_{outer} and exhibits a BSSP ω^+ nature at both inner and outer metallic interfaces. We assume that it originates from diffraction coupled counter-propagating SP_{outer} and SP_{inner} when $\mathbf{k}_{\mathbf{SPouter}} = \mathbf{G}\text{-}\mathbf{k}_{\mathbf{SPinner}}$ holds.

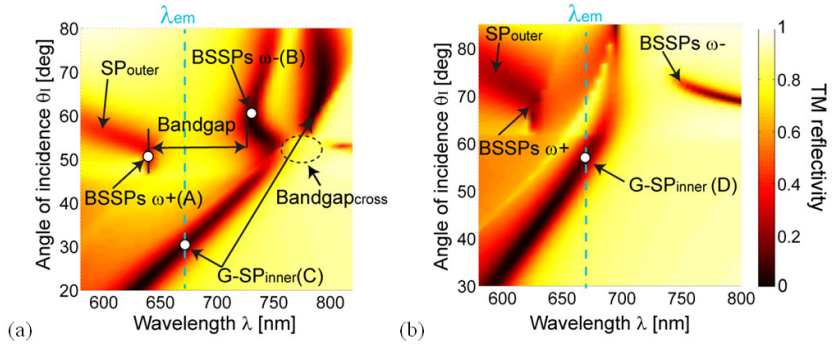

Fig. 4. Simulated reflectivity for grating modulation depth d = 30 nm and Ta_2O_5 layer with the thickness of (a) t_3 = 100 nm and (b) t_3 = 0 nm. The reflectivity (a) was calculated for LASFN9 substrate and (b) for BK7 substrate. Water on the top of PMMA layer and the azimuth angle ϕ = 0 deg are assumed.

#164156 - $15.00 USD Received 6 Mar 2012; revised 6 Apr 2012; accepted 15 May 2012; published 11 Jun 2012

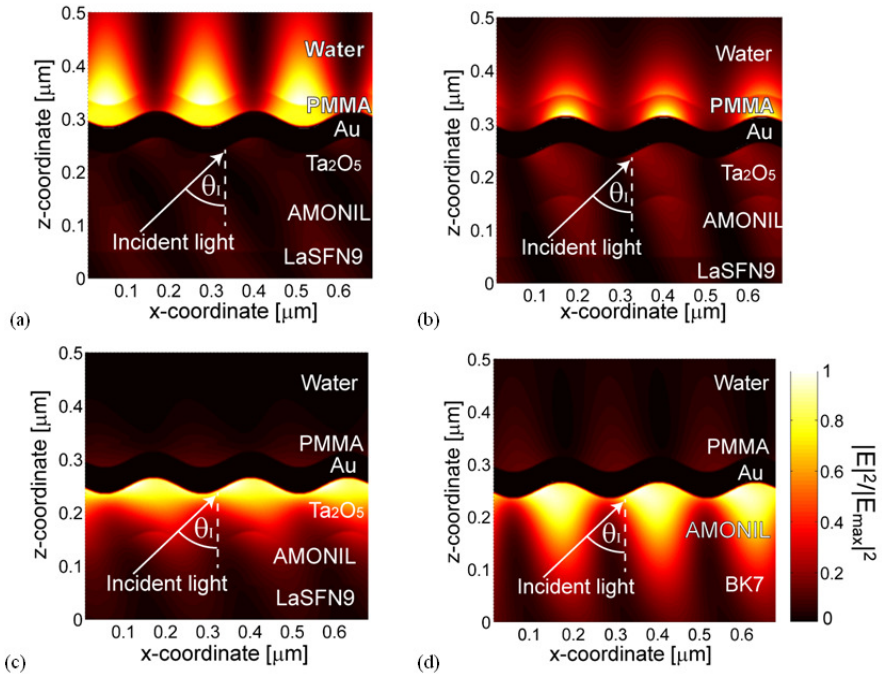

Fig. 5. Electric field intensity across the Bragg grating $|E|^2$ normalized with the maximum intensity $|(\mathbf{E})_{max}|^2$ calculated for (a) ATR–coupled BSSP mode ω^+ and (b) ATR–coupled BSSP mode ω^- at the outer gold interface, (c) grating-coupled propagating SP at the inner gold interface, and (d) coupled surface plasmon at the inner and outer interfaces. The respective angles and wavelengths are noted as circles in Fig. 4.

4.3 SPCE mediated by regular surface plasmons

SPCE on a flat layer structure without the corrugation (d = 0 nm) and air on the top (n_6 = 1) was firstly examined. The measured dispersion relation of surface plasmons for this geometry is shown in Fig. 6(a). It reveals that SPR occurs at the angle θ_I~39 deg in the LaFN9 glass substrate for the emission wavelength λ_{em} = 670 nm. The fluorescence image presented in Fig. 6(b) exhibits the characteristic SPCE cone with the polar angle θ_{em}~38 deg which is in agreement with the SPR condition at the emission wavelength λ_{em} in Fig. 6(a).

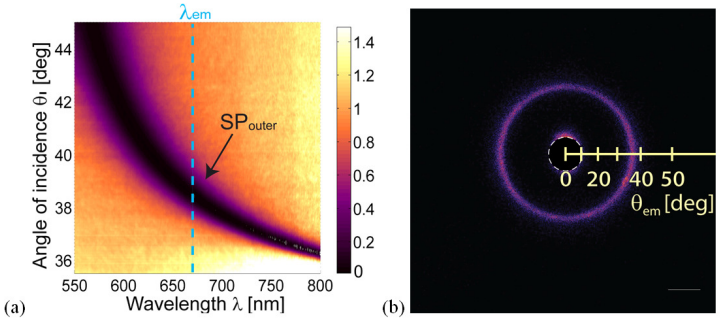

Fig. 6. (a) Dispersion relation of surface plasmons and (b) corresponding fluorescence emission image for flat layer structure on LaSFN9 substrate without Ta_2O_5 layer (t_3 = 0 nm) and air on the top n_6 = 1.

#164156 - $15.00 USD Received 6 Mar 2012; revised 6 Apr 2012; accepted 15 May 2012; published 11 Jun 2012

4.4 SPCE mediated by Bragg-scattered surface plasmons

Further, we investigated the effect of a Bragg grating to fluorescence emission on the samples supporting BSSPs modes close to the emission wavelength λ_{em}. When the refractive index of the upper medium is increased to n_6 = 1.33 and the layer structure is corrugated with the modulation depth of d = 10 nm, the resonant coupling to SP_{outer} shifts to higher angles and a gap appears in their dispersion relation. As seen in Fig. 7(a), BSSP modes located at edges of the bandgap occur at wavelengths of λ = 670 nm (ω^+) and 700 nm (ω^-). The BSSP ω^+ wavelength matches the fluorescence emission wavelength λ_{em} which leads to additional confinement of fluorescence signal on the SPCE cone at azimuth angles close to ϕ = 0 and 180 deg, see Fig. 7(b). The peak intensity at these angles where emission via BSSP ω^+ occurs was increased by a factor of ~3 compared to that for regular SPCE cone. This effect is due to the enhanced PMD associated with the presence of BSSP at the emission wavelength λ_{em} [24]. The emission via BSSPs occurs only at narrow range of azimuth angles as the bandgap is blue-shifted away from the emission wavelength λ_{em} by increasing ϕ. When increasing the modulation depth to d = 30 nm, the bandgap becomes wider and BSSP ω^+ and ω^- modes shifts to the wavelengths of 625 nm and 730 nm, respectively [see Fig. 7(c)] which agrees well with simulations presented in Fig. 4(a). Small differences between measured and simulated dispersion relation can be attributed to the discrepancy in refractive indices of materials and possible changes in modulation depth of the replicated grating. For this sample, the emission wavelength λ_{em} lies inside the bandgap and thus SPCE signal is canceled in the direction ϕ = 0 and 180 deg as shown in Fig. 7(d). Interestingly, the intensity of whole SPCE cone associated with emission via SP_{outer} modes is strongly decreased and the intensity of fluorescence signal at smaller polar angles θ_{em} is dramatically enhanced. This emission pattern is not symmetrical and the maximum intensity is observed at azimuth angles ϕ~ ± 50 and ± 130 deg.

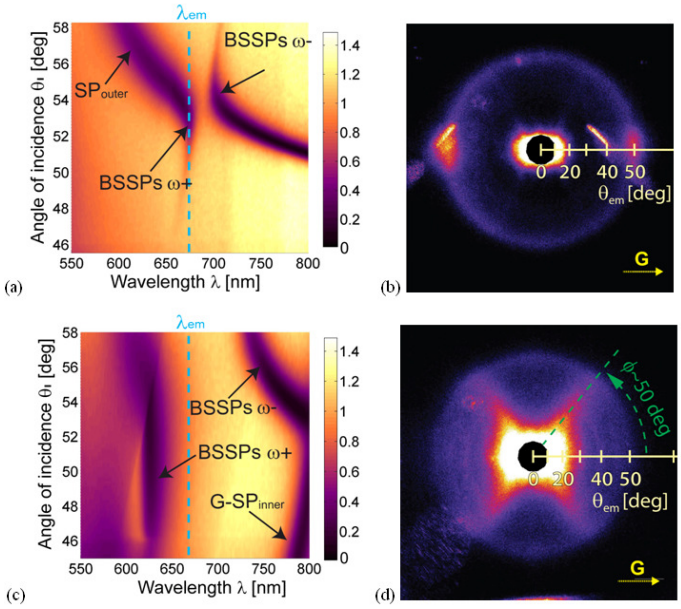

Fig. 7. Dispersion relations of surface plasmon modes on a gold grating surface with the Ta_2O_5 layer (t_3 = 100 nm) and water on the top (n_6 = 1.33) for the modulation depth of (a) d = 10 nm and (c) d = 30 nm. Corresponding spatial distribution of fluorescence light emitted into a LaSFN9 glass substrate for grating with the modulation depth of (b) d = 10 nm and (d) d = 30 nm.

In order to elucidate the origin of this feature, dispersion relation of surface plasmon modes supported by the grating was measured for azimuth angles varied from ϕ = 0 to 90 deg.

#164156 - $15.00 USD Received 6 Mar 2012; revised 6 Apr 2012; accepted 15 May 2012; published 11 Jun 2012

As shown in Fig. 8(a)-8(d), the wavelength at which G-SP_{inner} occurs is gradually blue-shifted and become less dependent on the angle of incidence θ_1 when increasing the azimuth angle ϕ. This observation agrees with previously reported works [25]. The measured azimuthal dispersion indicates that the the resonant coupling to G-SP_{inner} occurs at the emission wavelength of DiD dye λ_{em} = 670 nm for the azimuth angle ϕ = 50 deg. This angle matches the one at which the enhanced fluorescence emission was observed in Fig. 7(d). The weak dependence of the resonant wavelength on the angle of incidence θ_1 explains the broad polar angular range at which the fluorescence light is emitted via G-SP_{inner}. These data reveal that SP_{inner} can efficiently collect fluorescence light from fluorophores placed at the outer metallic surface. This feature is interesting as the simulated probability of the fluorescence emission for SP_{inner} on a flat structure is 6 times smaller than that for SP_{outer} (see Fig. 3) due to the relatively small overlap of SP_{inner} field with the top PMMA layer containing dyes [see Fig. 5(c)]. The enhanced emission rate via SP_{inner} can be ascribed to the redistribution of fluorescence emission pathways associated with the cancelling SP_{outer} on the corrugated grating layer architecture.

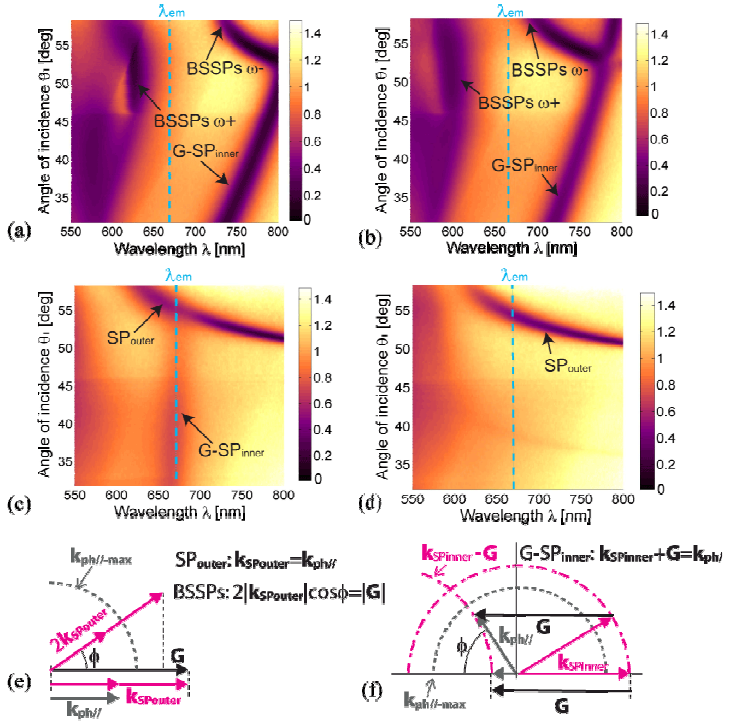

Fig. 8. Azimuth dependence of surface plasmon dispersion relation on a grating with the modulation depth d = 30 nm, Ta_2O_5 layer thickness t_3 = 100 nm, and water medium on the top n_6 = 1.33: (a) ϕ = 0 deg, (b) ϕ = 30 deg, (c) ϕ = 50 deg and (d) ϕ = 90 deg. Polar angles in LaSFN9 glass were measured. Momentum vector scheme for azimuth dependence of (e) Bragg-scaterred SP_{outer} and (f) diffraction grating-coupled SP_{inner}.

In addition, momentum vector schemes are shown in Fig. 8(e)-8(f) in order to illustrate the azimuth dispersion of the coupling to SP_{outer} and SP_{inner}. On the outer surface, the grating was designed to support Bragg-scattered SP_{outer} (occurring when $2\mathbf{k_{SPouter}} = \mathbf{G}$) at the wavelength 670 nm and azimuth angle ϕ = 0. Upon the excitation of SP_{outer} at an increased azimuth angle $\phi > 0$ deg, the parallel component of $2\mathbf{k_{SPouter}}$ to $\mathbf{G}$ is decreased and its magnitude does not match $|\mathbf{G}|$, see Fig. 8(e). In order to fulfill the Bragg-scattering condition, the magnitude of $\mathbf{k_{SPouter}}$ needs to be enlarged which occurs at lower wavelength and leads to

#164156 - $15.00 USD Received 6 Mar 2012; revised 6 Apr 2012; accepted 15 May 2012; published 11 Jun 2012

a blue shift of the bandgap as observed in Fig. 8(a)-8(d). For the inner surface, $SP_{SPinner}$ is excited by −1st diffraction order when the condition $\mathbf{k_{ph}}$-$\mathbf{G}$ = $\mathbf{k_{SPinner}}$ holds (where $\mathbf{k_{ph//}}$ is the in-plane momentum vector of the incident light beam). As Fig. 8(f) shows, the G-SP_{inner} excitation requires an enhanced magnitude of the in-plane momentum of the incident light beam $|\mathbf{k_{ph//}}|$ when the azimuth angle ϕ is increased. This leads to the larger resonance (polar) angle of incidence θ_I at a given wavelength and to a blue shift of the G-SP_{inner} resonance at a fixed angle of incidence θ_I. This trend is in agreement with measured data presented in Fig. 8(a)-8(d).

4.5 SPCE mediated by cross-coupled surface plasmons

Finally, SPCE on the grating structure with cross-coupled surface plasmons at inner and outer metallic surface was studied. The gold grating with the modulation depth of d = 30 nm on BK7 glass substrate was brought in contact with air (n_6 = 1) and water (n_6 = 1.33) in order to tune the SP_{outer}. The refractive index at the inner gold surface was decreased by choosing the thickness of Ta_2O_5 layer t_3 = 0 nm which shifted the excitation of G-SP_{inner} to lower wavelength below 700 nm. For the structure in contact with air, anti-crossing between G-SP_{inner} and ATR-coupled SP_{outer} occurs as seen in the measured dispersion relation in Fig. 9(a). Figure 9(b) shows that for this configuration the SPCE signal at the direction parallel to the grating vector ϕ = 0 and 180 deg is cancelled due to the gap occurring at emission wavelength λ_{em}. In other directions ($\phi \neq 0$ deg), SPCE retains its characteristic circular shape in the same manner with Fig. 8(b). When the refractive index of the upper medium is increased to n_6 = 1.33, the dispersion relation of SP_{outer} shifts to higher angles and a BSSP bandgap opens at wavelengths close to the emission wavelength λ_{em}, see Fig. 9(c).

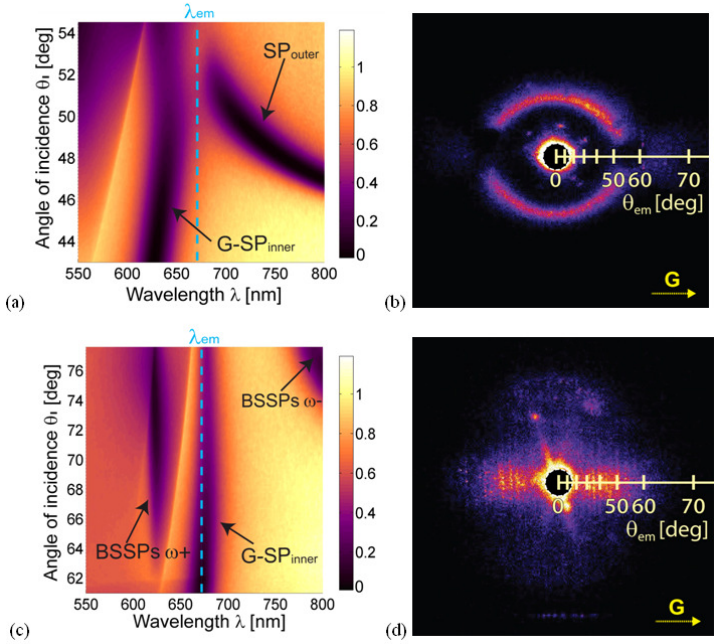

Fig. 9. Dispersion relation of cross-coupled surface plasmon modes for grating with the modulation depth of d = 30 nm and without Ta_2O_5 layer t_3 = 0 nm and the refractive index of upper medium (a) n_6 = 1 and (c) n_6 = 1.33 and respective fluorescence distributions emitted through the substrate (b) and (d).

As discussed in previous section, the grating-coupled SP_{inner} occurring inside this bandgap is partially cross-coupled to BSSPs ω^+ mode (see simulated dispersion relation in Fig. 4(b) which agree well with the experiment and electric field intensity profile in Fig. 5(d)). This

#164156 - $15.00 USD Received 6 Mar 2012; revised 6 Apr 2012; accepted 15 May 2012; published 11 Jun 2012

cross-coupling effect alters the dispersion relation of SP_{inner} which makes the resonance wavelength weakly dependent on the angle of incidence θ_I and increases the field strength at the outer gold interface, see Fig. 5(d). The corresponding SPCE image shows a dominant emission via SP_{inner} centered at azimuth angles $\phi = 0$ and 180 deg and cancelled SPCE cone via SP_{outer} modes. This fluorescence emission pattern has similarity to that shown in Fig. 7(d) for which the emission occurs at higher azimuth angles due to the larger propagation constant of SP_{inner} probing the Ta_2O_5 layer.

5. Conclusions

Dense sub-wavelength plasmonic gratings allow controlling spatial distribution of surface plasmon-coupled emission (SPCE) through a thin metal film on a dielectric substrate. The dispersion relation of surface plasmons at upper and lower interfaces of the thin metallic film can be simply tuned by changing the refractive index at respective metallic interfaces and enables exploiting a rich spectrum of Bragg scattered and cross-coupled surface plasmon modes. These waves can serve as efficient fluorescence decay channels for emitters placed on the top of the metallic film. In particular, modification of surface plasmon characteristics can suppress or enhance the fluorescence light intensity emitted to specific polar and azimuth directions on or inside the characteristic SPCE emission cone. These features can provide means for tuning the interaction of emitters with surface plasmons in areas including optical sources relying on nanoscale antennas and sensor utilizing surface plasmon-enhanced fluorescence spectroscopy. In particular, these observations may provide leads to advance plasmon-enhanced fluorescence sensors through more efficient collecting of fluorescence light emitted via Bragg-scattered surface plasmons, simpler detection of SPCE signal emitted at smaller polar angles and can be useful for multiplexing of sensing channels by emitting the fluorescence light from different sensing areas to different directions.

Acknowledgments

Support for this work was partially provided by the Austrian NANO Initiative (FFG and BMVIT) through the NILPlasmonics project within the NILAustria cluster (www.NILAustria.at) and by the Czech Science Foundation under grant # P205/12/G118.

#164156 - $15.00 USD Received 6 Mar 2012; revised 6 Apr 2012; accepted 15 May 2012; published 11 Jun 2012

Long range surface plasmon-coupled fluorescence emission for biosensor applications

Koji Toma, Jakub Dostalek,* and Wolfgang Knoll

AIT - Austrian Institute of Technology GmbH, Health and Environment Department, Muthgasse 11, 1190 Vienna, Austria

**jakub.dostalek@ait.ac.at*

Abstract: A biosensor scheme that employs long range surface plasmons (LRSPs) for the efficient excitation and collection of fluorescence light from fluorophore-labeled biomolecules captured in a three-dimensional hydrogel matrix is discussed. This new approach to plasmon-enhanced fluorescence (PEF) is experimentally and theoretically investigated by using the Kretschmann configuration of attenuated total reflection (ATR) method. A layer structure supporting LRSPs that consists of a low refractive index fluoropolymer layer, a thin gold film and a large binding capacity N-isopropylacrylamide (NIPAAm)-based hydrogel matrix swollen in an aqueous sample is employed. By using this layer architecture, the extended field of LRSPs probes the binding of biomolecules in the binding matrix at up to micrometer distances from the gold surface. With respect to regular surface plasmon-enhanced fluorescence spectroscopy (SPFS) and surface plasmon-coupled emission (SPCE), a narrower angular distribution of the fluorescence light intensity, a larger peak intensity and the excitation and emission at lower angles were observed.

OCIS codes: (240.6680) Surface plasmons; (170.6280) Spectroscopy, fluorescence and luminescence; (160.5470) Polymers.

References and links

1. M. Seidel and R. Niessner, "Automated analytical microarrays: a critical review," Anal. Bioanal. Chem. **391**(5), 1521–1544 (2008).
2. M. E. Stewart, C. R. Anderton, L. B. Thompson, J. Maria, S. K. Gray, J. A. Rogers, and R. G. Nuzzo, "Nanostructured plasmonic sensors," Chem. Rev. **108**(2), 494–521 (2008).
3. J. R. Lakowicz, "Plasmonics in biology and plasmon-controlled fluorescence," Plasmonics **1**(1), 5–33 (2006).
4. J. Dostálek and W. Knoll, "Biosensors based on surface plasmon-enhanced fluorescence spectroscopy," Biointerphases **3**(3), FD12–FD22 (2008).
5. T. Liebermann and W. Knoll, "Surface-plasmon field-enhanced fluorescence spectroscopy," Colloids Surf. A Physicochem. Eng. Asp. **171**(1-3), 115–130 (2000).
6. J. R. Lakowicz, J. Malicka, I. Gryczynski, and Z. Gryczynski, "Directional surface plasmon-coupled emission: A new method for high sensitivity detection," Biochem. Biophys. Res. Commun. **307**(3), 435–439 (2003).
7. J. S. Yuk, M. Trnavsky, C. McDonagh, and B. D. MacCraith, "Surface plasmon-coupled emission (SPCE)-based immunoassay using a novel paraboloid array biochip," Biosens. Bioelectron. **25**(6), 1344–1349 (2010).
8. S. C. Kitson, W. L. Barnes, and J. R. Sambles, "Photoluminescence from dye molecules on silver gratings," Opt. Commun. **122**(4-6), 147–154 (1996).
9. D. Sarid, "Long-range surface-plasma waves on very thin metal-films," Phys. Rev. Lett. **47**(26), 1927–1930 (1981).
10. G. Winter, S. Wedge, and W. L. Barnes, "Can lasing at visible wavelength be achieved using the low-loss long range surface plasmon-polariton mode?" N. J. Phys. **8**(8), 125–138 (2006).
11. T. Okamoto, J. Simonen, and S. Kawata, "Plasmonic crystal for efficient energy transfer from fluorescent molecules to long-range surface plasmons," Opt. Express **17**(10), 8294–8301 (2009).
12. I. De Leon and P. Berini, "Amplification of long-range surface plasmons by a dipolar gain medium," Nat. Photonics **4**(6), 382–387 (2010).
13. A. Kasry and W. Knoll, "Long range surface plasmon fluorescence spectroscopy," Appl. Phys. Lett. **89**(10), 101106 (2006).
14. J. Dostálek, A. Kasry, and W. Knoll, "Long range surface plasmons for observation of biomolecular binding events at metallic surfaces," Plasmonics **2**(3), 97–106 (2007).

#144352 - $15.00 USD Received 18 Mar 2011; revised 7 May 2011; accepted 13 May 2011; published 23 May 2011

15. Y. Wang, A. Brunsen, U. Jonas, J. Dostálek, and W. Knoll, "Prostate specific antigen biosensor based on long range surface plasmon-enhanced fluorescence spectroscopy and dextran hydrogel binding matrix," Anal. Chem. **81**(23), 9625–9632 (2009).
16. Y. Wang, J. Dostálek, and W. Knoll, "Long range surface plasmon-enhanced fluorescence spectroscopy for the detection of aflatoxin M_1 in milk," Biosens. Bioelectron. **24**(7), 2264–2267 (2009).
17. C. J. Huang, J. Dostalek, and W. Knoll, "Optimization of layer structure supporting long range surface plasmons for surface plasmon-enhanced fluorescence spectroscopy biosensors," J. Vac. Sci. Technol. B **28**(1), 66–72 (2010).
18. C. J. Huang, J. Dostalek, and W. Knoll, "Long range surface plasmon and hydrogel optical waveguide field-enhanced fluorescence biosensor with 3D hydrogel binding matrix: on the role of diffusion mass transfer," Biosens. Bioelectron. **26**(4), 1425–1431 (2010).
19. A. Aulasevich, R. F. Roskamp, U. Jonas, B. Menges, J. Dostalek, and W. Knoll, "Optical waveguide spectroscopy for the investigation of protein-functionalized hydrogel films," Macromol. Rapid Commun. **30**(9-10), 872–877 (2009).
20. M. Daimon and A. Masumura, "Measurement of the refractive index of distilled water from the near-infrared region to the ultraviolet region," Appl. Opt. **46**(18), 3811–3820 (2007).
21. W. N. Hansen, "Electric fields produced by the propagation of plane coherent electromagnetic radiation in a stratified medium," J. Opt. Soc. Am. **58**(3), 380–388 (1968).
22. G. W. Ford and W. H. Weber, "Electromagnetic interactions of molecules with metal surfaces," Phys. Rep. **113**(4), 195–287 (1984).
23. L. Polerecký, J. Hamrle, and B. D. MacCraith, "Theory of the radiation of dipoles placed within a multilayer system," Appl. Opt. **39**(22), 3968–3977 (2000).
24. P. W. Beines, I. Klosterkamp, B. Menges, U. Jonas, and W. Knoll, "Responsive thin hydrogel layers from photo-cross-linkable poly(N-isopropylacrylamide) terpolymers," Langmuir **23**(4), 2231–2238 (2007).

1. Introduction

Over the last decade, increasing efforts were devoted to fluorescence-based detection of chemical and biological analytes [1] with advanced sensitivity by using plasmon-enhanced fluorescence (PEF) [2–4]. Surface plasmons (SPs) are optical waves that originate from coupled collective oscillations of electron plasma and associated electromagnetic field at a metallic surface. Up to now, two main approaches that rely on SPs propagating along continuous metallic films were pursued for PEF. In surface plasmon-enhanced fluorescence spectroscopy (SPFS) [5], the binding of fluorophore-labeled molecules to biomolecular recognition elements attached on a metallic sensor surface is probed by the enhanced field intensity of SPs. This method takes advantage of increased excitation rate of fluorophores that is directly translated to an enhanced fluorescence signal. In surface plasmon-coupled fluorescence emission (SPCE) [6], fluorescence light emitted by fluorophores via SPs is detected. The out-coupling of fluorescence light that is trapped in SPs to far field radiation by using hemispherical [6] and parabolic [7] dielectric elements and metallic diffraction gratings [8] was reported to provide efficient means for collecting of SPCE signal. Owing to the evanescent profile of the SP electromagnetic field, only the fluorescence signal originating from fluorophores in a close proximity to the metallic surface (distance up to ~100 nm) is detected by SPFS and SPCE methods leading to a greatly suppressed background.

In this paper, we investigate the excitation and emission of fluorophore-labeled biomolecules on a sensor surface that is supporting long range surface plasmons (LRSPs). These surface plasmon modes propagate along a thin metallic film that is embedded in dielectrics with similar refractive indices. They exhibit lower losses and an evanescent field that probe deeper away from a metallic surface compared to regular SPs [9]. The coupling of fluorophores with LRSPs was subject to theoretical investigation [10,11] and recently it found applications in areas including plasmonic lasers [12] and SPFS biosensors [13]. In the biosensor applications, LRSPs are particularly attractive for probing biointerfaces with an extended three-dimensional hydrogel matrix that offer a large binding capacity [14] and allowed for the detection of molecular analytes at low femtomolar concentrations in real samples [15,16]. In order to push forward the sensitivity of this biosensor scheme, we experimentally and theoretically study the excitation and emission of fluorescence light from dye molecules dispersed in a hydrogel binding matrix via LRSPs. The implementation of this method for more efficient and simpler detection of the fluorescence light is discussed.

#144352 - $15.00 USD Received 18 Mar 2011; revised 7 May 2011; accepted 13 May 2011; published 23 May 2011

2. Materials and methods

2.1 Materials

Cytop fluoropolymer (CTL-809M, 9 wt % in the solvent of CT-solv 180) was purchased from Asahi Glass (Japan). Phosphate buffered saline (PBS) with pH 7.4 was obtained from Calbiochem (Germany). PBS-Tween (PBS-T) buffer was prepared by adding 0.05% of Tween20 (Sigma-Aldrich, USA) to PBS buffer solution. Anti-mouse IgG (a-IgG) and mouse IgG (IgG) were from Molecular Probes (USA). a-IgG molecules were labeled with Alexa Fluor 647 with the dye-to-protein molar ratio of 4.5. This dye exhibits the quantum efficiency of $\eta = 0.33$ and the absorption and emission wavelengths at 650 nm and 668 nm, respectively. 10 mM acetate buffer (ACT) with pH 4 was prepared in house. 1-Ethyl-3-(3-dimethylaminopropyl) carbodiimide (EDC) was from Pierce (USA). Photocrosslinkable poly(*N*-isopropylacryamide) (NIPAAm)-based hydrogel with benzophenon and carboxylic groups, S-3-(benzoylphenoxy)propyl ethanthioate (benzophenone-thiol) and sodium *para*-tetrafluorophenol sulfonate (TFPS) were synthesized at Max Planck Institute for Polymer Research in Mainz, Germany. Ethanolamine (Sigma-Aldrich, USA) was dissolved in water at 1 M concentration with the pH of the solution adjusted to 8.5 with sodium hydroxide.

2.2 Preparation of sensor layer structures supporting LRSPs and regular SPs

The preparation of a layer structure supporting LRSP, grafting of a hydrogel binding matrix on its top and the immobilization of biomolecules were described in our previous works [17], [18]. Briefly, Cytop fluoropolymer film (thickness $d_{Cytop} = 655 \pm 15$ nm) was spin coated on a glass substrate followed by the deposition of gold layer (thickness $d_m = 18.9 \pm 1.7$ nm) by means of magnetron sputtering (UNIVEX 450C, Leybold Vacuum, Germany). For a comparison, a gold film (thickness $d_m = 47.2 \pm 0.8$ nm) was prepared on a glass substrate for the excitation of regular SPs. After the gold deposition, the surface of substrates supporting LRSP and regular SP was subsequently modified by benzophenon-thiol self-assembled monolayer (SAM), coated with NIPAAm-based hydrogel (thickness in a dry state of 60 nm) and exposed to UV light (an irradiation dose of 2 J cm^{-2} at a wavelength of $\lambda = 365$ nm) in order to photocrosslink the hydrogel film. As shown in our previous studies [19], the prepared NIPAAm-based hydrogel film swells in PBS-T buffer with the factor of around 10 leading to an increase in its thickness to d_h~600 nm. Swollen hydrogel film was *in situ* functionalized with IgG molecules by the reacting of carboxylic groups in the gel with a mixture of EDC and TFPS followed by the covalent coupling of IgG molecules dissolved in ACT buffer via their amine moieties [19]. Afterwards, unreacted active ester groups of the hydrogel were passivated by the incubation in ethanolamine solution. Finally, fluorophore-labeled a-IgG molecules dissolved in PBS-T were flowed over the surface until the saturation of the affinity binding to immobilized IgG molecules was reached. The concentration of a-IgG that was captured in the gel was $c \sim 10^{-4}$ M which corresponds to the surface mass density $\Gamma = c/d_h \sim 10$ ng/mm^2 (for a-IgG molecular weight 160 kDa).

2.3 Optical setup

An optical setup based on attenuated total reflection (ATR) method with Kretschmann configuration was employed. As depicted in Fig. 1(a), He-Ne laser beam at the wavelength of $\lambda_{ex} = 633$ nm was launched to a 90° LASFN9 glass prism. On the prism base, a sensor chip for the excitation of LRSPs or regular SPs was optically matched, see Fig. 1(b). The intensity of the laser beam reflected from the prism base was measured with a photodiode detector and a lock-in amplifier (Model 5210, Princeton Applied Research, USA). Fluorescence light emitted from the surface at the wavelength of $\lambda_{em} = 670$ nm was coupled to an optical fiber by using a collimator (F220SMA-B, Thorlabs, Germany) and its intensity was detected by a photomultiplier tube (H6240-01, Hamamatsu, Japan) which was connected to a counter (53131A, Agilent, USA). The prism and detectors were mounted on a two-circle rotation

#144352 - $15.00 USD Received 18 Mar 2011; revised 7 May 2011; accepted 13 May 2011; published 23 May 2011

stage (Huber GmbH, Germany) in order to control the angle of incidence of the laser beam θ_I (wavelength λ_{ex}) and the angle θ_F at which the fluorescence light was collected (wavelength λ_{em}). A set of filters including edgepass filter (FES0650, Thorlabs, Germany), notch filter (XNF-632.8-25.0M, CVI Melles Griot, Germany) and band-pass filter (670FS10-25, LOT-Oriel, Germany) was used in order to suppress the background signal. The optical setup was controlled with a software Wasplas (developed at Max Plank Institute for Polymer Research in Mainz, Germany) and it allowed recording angular spectra of the reflectivity $R(\theta_I)$ and fluorescence intensity $F(\theta_I, \theta_F)$ at wavelengths λ_{ex} and λ_{em}, respectively. The fluorescence light emitted via LRSP and regular SP waves forms a characteristic cone centered at a (polar) angle θ_F for which surface plasmon modes are out-coupled by reverse Kretschmann configuration. A cross-section of the cone was measured for the azimuth angle fixed at $\phi = 0$ (see Fig. 2).

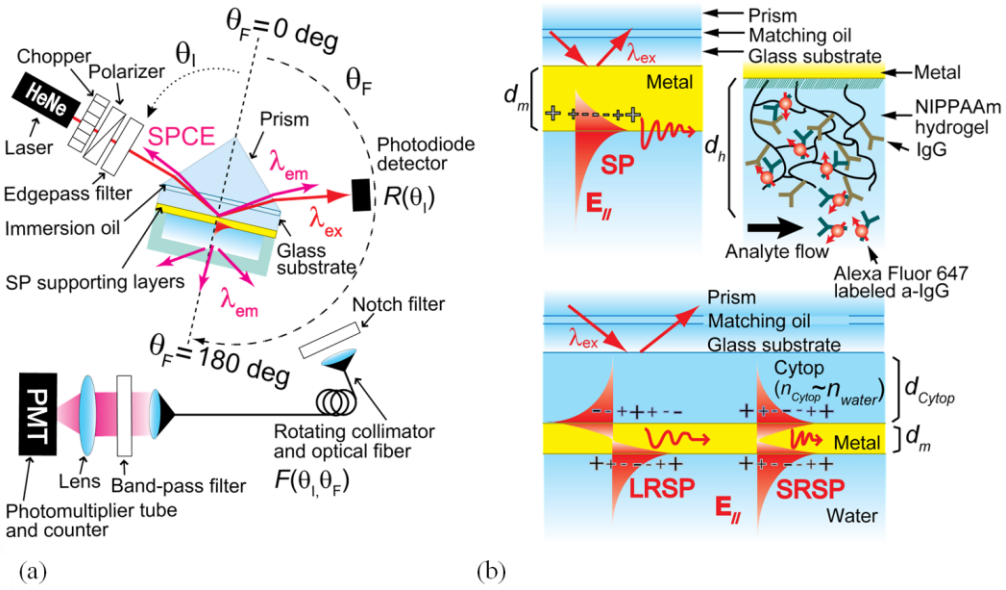

Fig. 1. (a) Optical setup for the measurement of fluorescence intensity $F(\theta_I, \theta_F)$ and reflectivity $R(\theta_I)$ angular spectra. (b) Layer architectures supporting regular SPs and LRSPs with a hydrogel binding matrix.

For the measurement of angular reflectivity spectra $R(\theta_I)$ at wavelengths λ_{ex} and λ_{em} , we used a modified setup where the laser light source and photodiode detector were replaced with a halogen lamp coupled to an optical fiber with a collimator producing a parallel polychromatic beam and with a spectrometer (HR4000 from Ocean Optics, USA), respectively. Refractive indices of gold films supporting LRSP and regular SP waves were obtained by fitting measured reflectivity curves $R(\theta_I)$ by using transfer matrix-based Fresnel reflectivity model (see Fig. 3) which was implemented in the software Winspall (developed at Max Planck Institute for Polymer Research in Mainz, Germany). The refractive indices of a gold film on Cytop polymer were $n_{Au}(\lambda_{em}) = 0.128 + 2.65i$ and $n_{Au}(\lambda_{ex}) = 0.2 + 2.68i$. The refractive indices of gold film on a glass substrate were determined as $n_{Au}(\lambda_{em}) = 0.118 + 3.92i$ and $n_{Au}(\lambda_{ex}) = 0.153 + 3.52i$ which differ from those on the Cytop surface due to a different morphology [17]. In further simulations, refractive indices of LASFN9 glass n_p, Cytop polymer n_{Cytop}, and buffer n_s at the emission and excitation wavelengths were taken from the literature as $n_p(\lambda_{em}) = 1.841$, $n_p(\lambda_{ex}) = 1.845$, $n_{Cytop}(\lambda_{em}) = 1.336$, $n_{Cytop}(\lambda_{ex}) = 1.337$, $n_s(\lambda_{em}) = 1.331$ and $n_s(\lambda_{ex}) = 1.332$ [17,20]. Refractive index of hydrogel matrix was assumed to be $n_h(\lambda_{ex}, \lambda_{em}) = 1.35$ [19].

#144352 - $15.00 USD Received 18 Mar 2011; revised 7 May 2011; accepted 13 May 2011; published 23 May 2011

2.4 Simulations

The classical theory of fluorescence near a metal surface [21,22] was employed for the simulation of fluorescence intensity F emitted from the hydrogel binding matrix. In these simulations, we assumed homogenously distributed, randomly oriented and identical dye molecules that were represented as oscillating emission and absorption dipoles. The orientation of emission dipole moment $\boldsymbol{\mu}_{em}$ was defined by polar α and azimuth β angles as shown in Fig. 2. A relative angle between the emission $\boldsymbol{\mu}_{em}$ and excitation $\boldsymbol{\mu}_{ex}$ dipole moments γ was assumed in order to take into account the structure of the dye molecule. This angle is between 0 ($\boldsymbol{\mu}_{em}$ and $\boldsymbol{\mu}_{ex}$ are parallel) and 90 deg ($\boldsymbol{\mu}_{em}$ and $\boldsymbol{\mu}_{ex}$ are perpendicular). In the model, rotation of dye molecules upon the emission was omitted. This assumption is reasonable as organic dyes were attached to a large protein which rotates much slower (characteristic time >10 ns) compared to the lifetime of excited dye (τ = 1 ns for Alexa Fluor 647 according to the manufacturer). Therefore, the excitation dipole $\boldsymbol{\mu}_{ex}$ lying on a cone with the axis parallel to $\boldsymbol{\mu}_{em}$, fixed aperture 2γ and an azimuth angle ρ between 0 and 360 deg was used. The spatial position of a dipole was described by its distance from the metal surface t.

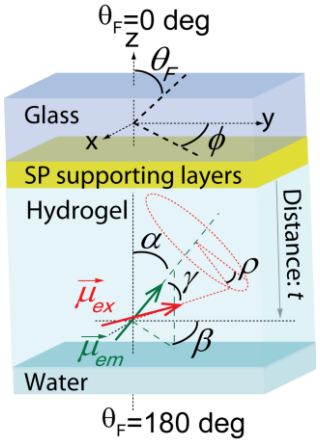

Fig. 2. Multilayer system and definition of coordinate system.

By averaging over all possible dipole orientations α, β and ρ and distances t, the fluorescence intensity F emitted at the wavelength λ_{em} to the solid angle $d\Omega = \sin(\theta_F)d\theta_F d\phi$ was obtained as:

$$F(\theta_I,\theta_F,\phi)d\Omega \propto \int P_{ex}\frac{P_{em}}{P_{tot}+P_{nr}}d\alpha\, d\beta\, d\rho\, dt\, d\Omega, \tag{1}$$

where θ_F and ϕ are fluorescence emission polar and azimuth angles, respectively, P_{ex} is the excitation rate due to the absorption of photons at the wavelength λ_{ex}, P_{em} is the emission rate that is accompanied with emitting photons at the wavelength λ_{em} and P_{nr} is the non-radiative decay rate with which the excited dye relaxes to the grounds state without emitting a photon. P_{tot} is the total radiative dissipation rate to all propagating and evanescent waves at the emission wavelength λ_{em}. The excitation rate P_{ex} was obtained as:

$$P_{ex}(t,\alpha,\beta,\theta_I) \propto \left|\boldsymbol{\mu}_{ex}(\alpha,\beta)\cdot\mathbf{E}_{ex}(\theta_I,t)\right|^2, \tag{2}$$

where $\mathbf{E}_{ex}$ is the electric field amplitude at distance t from the metal surface upon the excitation plane wave at the wavelength λ_{ex} hits the surface under an angle θ_I. The emission rate $P_{em}(\theta_F,\phi,t,\alpha,\beta)$ was calculated by using the transfer matrix-based model described by Polerecky et al. [23]. The non-radiative decay rate was described as $P_{nr} = P_{tot}(1/\eta\text{-}1)$ where P_{tot}

#144352 - $15.00 USD Received 18 Mar 2011; revised 7 May 2011; accepted 13 May 2011; published 23 May 2011

for $t\rightarrow\infty$ was used (which corresponds to a dye immersed in water). For a dye in the proximity to a metal film, the total radiative energy dissipation rate P_{tot} is altered by additional emission channels associated with coupling to optical waves propagating along its surface. P_{tot} was obtained as a function of distance t by using the theory described by Ford et al. [22] as:

$$P_{tot}(t,\alpha)=\int_0^{\infty}\frac{dP_{em}}{dk_{//}}\left(k_{//},t,\alpha\right)dk_{//}, \tag{3}$$

$$\frac{dP_{em}}{dk_{//}}\left(k_{//},t,\alpha\right)=\frac{3}{2}\frac{1}{k_h^3}\Re e\left[\frac{k_{//}}{\sqrt{k_h^2-k_{//}^2}}\left\{\mu_{em\perp}^2\left(k_{//}^2r_{\perp}^{TM}\right)+\frac{1}{2}\mu_{em//}^2\left(k_h^2r_{//}^{TE}+\left(k_h^2-k_{//}^2\right)r_{//}^{TM}\right)\right\}\right], \tag{4}$$

where $dP_{em}/dk_{//}$ is the energy dissipation density and $k_{//}$ is the component of the propagation constant that is parallel to the surface (e.g., $k_{//}=2\pi/\lambda_{em}n_p sin\theta_F$ for waves propagating in the glass and $k_{//}>2\pi/\lambda_{em}n_p$ for evanescent lossy surface waves). The propagation constant of light in the hydrogel film is denoted as $k_h=2\pi/\lambda_{em}n_h$. $\mu_{em\perp}=|\mu_{em}|\cos(\alpha)$ and $\mu_{em//}=|\mu_{em}|\sin(\alpha)$ are the perpendicular and parallel components of the emission dipole moment, respectively. Coefficients $r_{\perp}^{TM}$ and $r_{//}^{TM}$ take into account changes in perpendicular and parallel components of electric field amplitudes of transverse magnetic polarized (TM) field upon multiple reflections at the hydrogel interfaces. Similarly, the coefficient $r_{//}^{TE}$ is the amplitude change for transverse electrical (TE). These coefficients can be described by the TM reflectivity $r_{+,-}^{TM}$ and TE reflectivity $r_{+,-}^{TE}$ at the interface between hydrogel and metal (+) and at the interface between hydrogel and water (-) as follows and are discussed in more detail in [22].

$$r_{\perp}^{TM}=\frac{[1+r_{-}^{TM}\exp(2i\sqrt{k_h^2-k_{//}^2}\cdot(d_h-t))][1+r_{+}^{TM}\exp(2i\sqrt{k_h^2-k_{//}^2}\cdot t)]}{1-r_{-}^{TM}r_{+}^{TM}\exp(2i\sqrt{k_h^2-k_{//}^2}\cdot d_h)}, \tag{5a}$$

$$r_{//}^{TM}=\frac{[1-r_{-}^{TM}\exp(2i\sqrt{k_h^2-k_{//}^2}\cdot(d_h-t))][1-r_{+}^{TM}\exp(2i\sqrt{k_h^2-k_{//}^2}\cdot t)]}{1-r_{-}^{TM}r_{+}^{TM}\exp(2i\sqrt{k_h^2-k_{//}^2}\cdot d_h)}, \tag{5b}$$

$$r_{//}^{TE}=\frac{[1+r_{-}^{TE}\exp(2i\sqrt{k_h^2-k_{//}^2}\cdot(d_h-t))][1+r_{+}^{TE}\exp(2i\sqrt{k_h^2-k_{//}^2}\cdot t)]}{1-r_{-}^{TE}r_{+}^{TE}\exp(2i\sqrt{k_h^2-k_{//}^2}\cdot d_h)}. \tag{5c}$$

3. Results and discussion

3.1 Profile of probing field

As Fig. 3(a) shows, the coupling of a light beam to LRSPs and regular SPs is manifested as a resonance dip in the angular spectrum $R(\theta_I)$. In Fig. 3(b), respective profiles of electric field intensity upon the resonant coupling to LRSPs and SPs (Kretschmann configuration with θ_I = 48.5 and 56.7 deg, respectively, at the wavelength λ_{ex}) are compared to those when the light beam is normal incident at the gold surface through the sample (direct excitation θ_I = 180 deg). The electric field intensity $|\mathbf{E}|^2$ was normalized with the intensity of the light beam $|\mathbf{E_0}|^2$ incident through the prism (Kretschmann configuration) or through the sample (direct excitation). These data show that fields of LRSPs and regular SPs peak at the interface between the metal and hydrogel and then exponentially decay through the hydrogel in the aqueous medium. LRSP mode exhibits a penetration depth of L_p = 542 nm and average field intensity enhancement of $|\mathbf{E}|^2_{ave}/|\mathbf{E_0}|^2$ = 37 in the hydrogel matrix with the thickness of d_h = 600 nm. Let us note that the penetration depth L_p is defined as the distance at which the amplitude of the evanescent field drops by the factor of 1/e and the average field intensity was calculated as:

#144352 - $15.00 USD Received 18 Mar 2011; revised 7 May 2011; accepted 13 May 2011; published 23 May 2011

$$|\mathbf{E}|^2_{ave} = \frac{1}{d_h}\int_0^{d_h} |\mathbf{E}(t)|^2 \, dt. \tag{6}$$

The excitation of regular SPs is associated with lower average electric field intensity enhancement of $|\mathbf{E}|^2_{ave}/|\mathbf{E_0}|^2$ = 8 as its penetration depth L_p = 180 nm and maximum field intensity enhancement are smaller than those for LRSP. Directly incident light beam is reflected at the gold surface and the interference gives rise to an oscillating field intensity profile with average intensity enhancement of $|\mathbf{E}|^2_{ave}/|\mathbf{E_0}|^2$ = 1.3 and $|\mathbf{E}|^2_{ave}/|\mathbf{E_0}|^2$ = 2.0 on substrates supporting LRSPs and regular SPs, respectively.

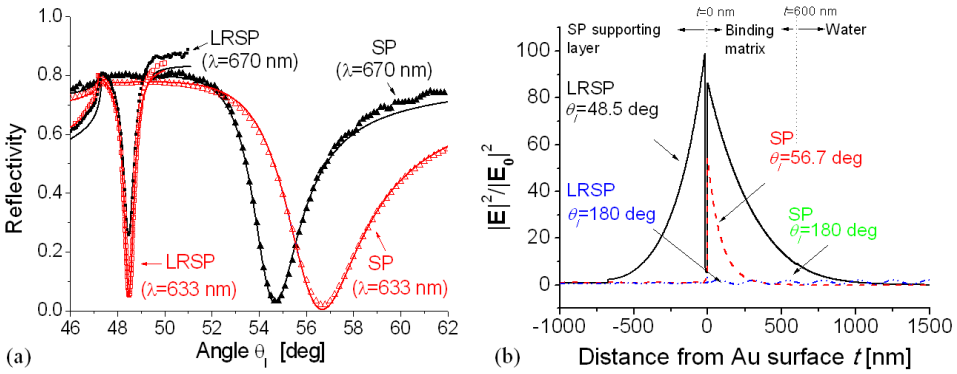

Fig. 3. (a) Angular reflectivity spectra measured for the excitation of LRSP (■, □) and SP modes (▲, Δ) at wavelengths of λ_{em} = 670 nm (filled) and λ_{ex} = 633 nm (blank). Lines denote the fitted curves. (b) Simulated electric field intensity profile at the wavelength λ_{ex} = 633 nm upon the resonant coupling of LRSPs (θ_I = 48.5 deg, solid line) and SPs (θ_I = 56.7 deg , dashed line) compared to that of directly incident light (θ_I = 180, LRSP: dotted line and SP: dashed dot line).

3.2 Emission via surface plasmon waves

After the excitation, dyes in vicinity to a metal surface can emit photons via surface plasmon modes at the wavelength λ_{em}. These decay channels can be observed from the energy dissipation density $dP_{em}/dk_{//}$ that is presented in Fig. 4. It compares the emission dissipation density for dyes dispersed in a dielectric layer with the refractive index n_h and thickness of d_h = 20 and 600 nm on the top of the structure supporting (a) LRSPs and (b) regular SPs. The propagation constant region $0 \le k_{//} \le n_s k_0$ corresponds to the fluorescence emission via modes propagating away from a metal surface (far field emission). For propagation constants in the range $n_s k_0 \le k_{//} \le n_p k_0$, the fluorescence emission couples to waves that are evanescent in the sample and propagating in the glass. For larger propagation constants $k_{//} > k_0 n_p$, the fluorescence is emitted via waves that are evanescent to both glass and the sample and they contribute to the dissipation of fluorescent light in the metal (quenching).

The emission via surface plasmon modes is manifested as a series of peaks in the energy dissipation density located at distinct $k_{//}$. The emission via LRSPs (1) is manifested as a narrower peak that is located at smaller $k_{//}$ with respect to the one for regular SPs (2). In addition, one can see the emission via other modes including surface plasmons propagating at the interface between glass and gold (3) and short range surface plasmons (SRSPs) (4). For the dipole-loaded layer with the thickness of d_h = 600 nm, the peak energy dissipation density associated with the coupling to LRSPs is 10.6 fold higher compared to that with regular SPs. For a thinner layer with a thickness of d_h = 20 nm, the LRSP peak energy dissipation density is 2.2 fold higher that for the SP.

#144352 - $15.00 USD Received 18 Mar 2011; revised 7 May 2011; accepted 13 May 2011; published 23 May 2011

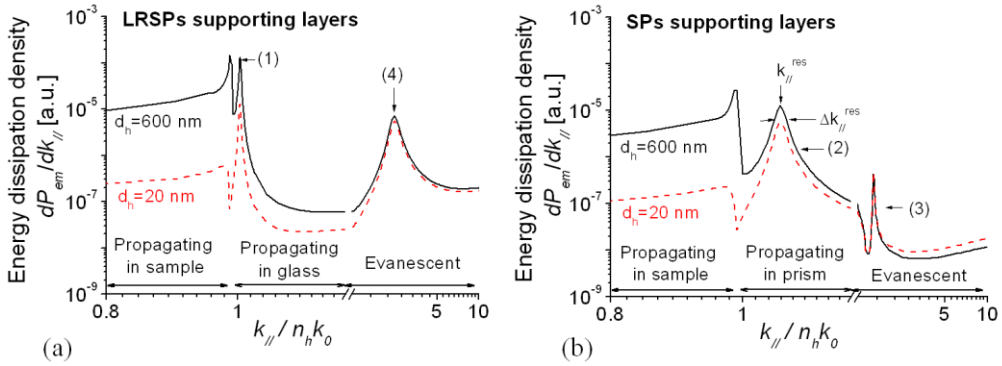

Fig. 4. Simulated energy dissipation density as a function of parallel component of the propagation constant $k_{//}$ for the binding matrix with the thickness d_h = 20 nm (red) and 600 nm (black) on the top of a layer structure supporting (a) LRSP and (b) regular SP modes.

Figure 5 presents the dependence of the energy dissipation probabilities $D(t)$ via regular SP, LRSP and SRSP modes on the distance t between a randomly oriented dye and the metal surface. The energy dissipation probability was calculated as:

$$D(t) = \int_0^{2\pi} \int_{-3/2\Delta k_{//}^{res}}^{3/2\Delta k_{//}^{res}} \frac{1}{P_{tot}(t,\alpha)} \frac{dP_{em}}{dk_{//}} \left(k_{//} - k_{//}^{res}, t, \alpha\right) d\alpha dk_{//}, \qquad (7)$$

where $k_{//}^{res}$ is the propagation constant at which the coupling to respective mode occurs and $\Delta k_{//}$ is the full width in the half maximum of the peak in the energy dissipation density [see Fig. 4(b)]. As seen in Fig. 5, the coupling efficiency to SRSPs has the maximum at distances around t = 10 nm (where more than 90% of fluorescence light is emitted via this mode) and it rapidly decreases for t>20 nm. As SRSPs cannot be out-coupled by the used reverse Kretschmann configuration, the emission via these modes enhances quenching of the fluorescence. For regular SPs, the maximum emission probability of around 60% occurs at distances around t = 20 nm. The emission of fluorescence light is coupled weaker to LRSP mode and reaches its maximum of around 20% at t = 60 nm from the metal surface.

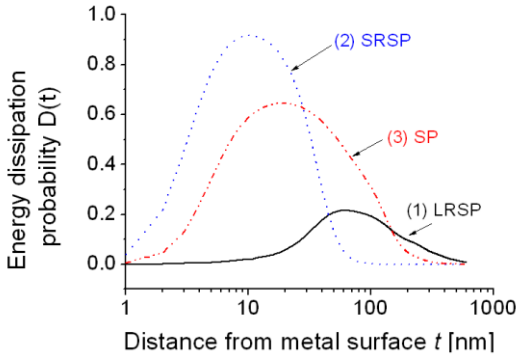

Fig. 5. The dependence of energy dissipation probability on the distance from a gold surface t. The probabilities through surface plasmon waves (LRSP: (1), SP: (3)) that can be recovered by reverse Kretschmann configuration $n_h k_0 \leq k_{//} \leq n_p k_0$ and that of SRSP which is a part of lossy wave are plotted (2).

For dyes distributed in the hydrogel, the average energy dissipation probability of via different surface plasmon modes was obtained by integrating respective $D(t)$:

#144352 - $15.00 USD Received 18 Mar 2011; revised 7 May 2011; accepted 13 May 2011; published 23 May 2011

$$D_{ave} = \frac{1}{d_h}\int_0^{d_h} D(t)dt. \quad (8)$$

For LRSP, the average energy dissipation probability for dyes dispersed in a 600 nm thick hydrogel matrix reaches D_{ave} = 7% which is comparable to that for regular SPs (D_{ave} = 11%) and SRSPs (D_{ave} = 5%), respectively. These data illustrate the balance between the effect of surface plasmon field confinement (enabling more efficient collecting of fluorescence light from a tight volume) and the thickness of the binding matrix (that can accommodate larger amount of molecules and can provide to stronger fluorescence signals).

3.3 Out-coupling of fluorescence light emitted through LRSP and SP modes

The excitation and out-coupling of fluorescence light via LRSPs and SPs modes was experimentally observed and compared with simulations. Firstly, dye-labeled biomolecules captured in a 600 nm thick binding matrix were directly excited by a laser beam normal incident at the gold surface (θ_I = 180 deg) and the fluorescence intensity $F(\theta_F)$ emitted through the prism was measured. As Fig. 6(a) shows, the fluorescence light emitted via LRSP and SP modes gives rise to distinct peaks in $F(\theta_F)$ spectra centered at angles θ_F = 49.3 and 56.5 deg, respectively. In the experiment, the maximum fluorescence intensity is about 1.9 ± 1.2 (standard deviation - SD) fold higher for LRSPs compared to that for SPs. In addition, full width at half maximum (FWHM) of the emission peak is 6-times narrower than that of SPs which is attributed to the lower damping of LRSPs. In Fig. 6(b), spectra from identical substrates were measured upon the fluorescence excitation by the enhanced field intensity of LRSP and regular SP modes. One can see that the peak fluorescence intensity was increased by a factor of 37 ± 10 (SD) for LRSPs with respect to that for direct excitation. Similarly, the measured peak fluorescence intensity was increased by a factor of 16 ± 8 (SD) for the SPs. The ratio of the peak fluorescence intensity for the excitation and emission via LRSP and regular SP was 4.4, see Fig. 6(b).

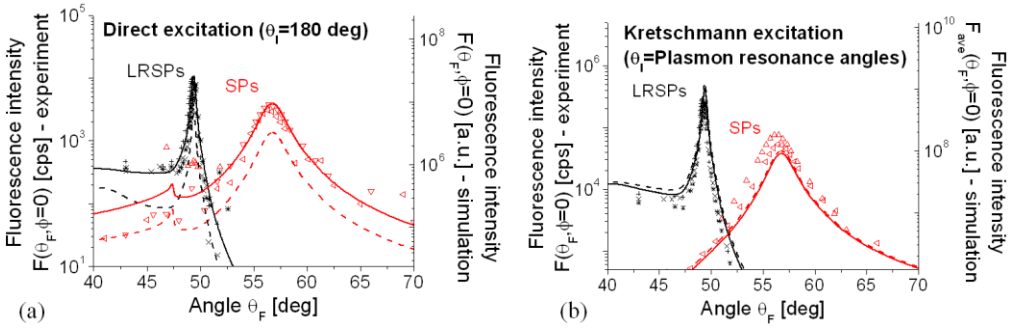

Fig. 6. Experimental fluorescence intensity emitted via LRSP and SP modes for (a) direct excitation with a laser beam (θ_I = 180 deg) and (b) for the excitation via LRSP and SP modes. In each experiment, three samples were measured (black symbols for LRSPs and red symbols for SPs) and compared to the simulations with the relative angles γ = 0 and 45 deg (dashed and solid lines, respectively).

In the simulations, for the relative angle between the emission and absorption dipole γ = 0, the enhancement of peak fluorescence intensity F upon the excitation by LRSP and regular SPs is significantly larger (197-fold and 31-fold, respectively) and it decreases to 44 and 10, respectively, when increasing to the relative angle to γ = 45 deg. As the structure and the relative angle of used Alexa Fluor 647 dye are not known, this parameter was varied to match simulations with experimental data. The data presented in Fig. 6 reveal good agreement between experimental and simulation curves for γ close to 45 deg. Additional small discrepancies can be attributed to the inhomogeneous distribution of a-IgG in the hydrogel film. The used NIPAAm-base hydrogel was reported to exhibit higher density in vicinity to

#144352 - $15.00 USD Received 18 Mar 2011; revised 7 May 2011; accepted 13 May 2011; published 23 May 2011

the metal surface compared to the outer interface with a sample [24] and thus the density of dyes attached to individual IgG molecules is likely gradually decreasing when increasing the distance from the metal surface. Lastly, let us note that the measured enhancements for the excitation of the fluorescence light intensity via LRSPs and regular SPs, respectively, are comparable to the calculated average field intensity enhancement of $|\mathbf{E}|^2_{ave}/|\mathbf{E_0}|^2$ = 37 and 8, respectively. However, the presented work shows that besides increasing the excitation rate by large field intensity enhancement, also careful design of fluorescence decay channels needs to be addressed in order to achieve maximum sensitivity of fluorescence light detection.

4. Conclusions

We investigated the long range surface plasmon-assisted excitation and emission of fluorophore-labeled molecules captured in a large-binding capacity hydrogel matrix. These surface plasmon modes offer the advantage of lower damping, more extended profile of electromagnetic field and higher field intensity enhancement with respect to regular surface plasmons. The obtained experimental data measured by using the ATR method with Kretschmann configuration exhibited good agreement with simulations. It revealed that, compared to regular surface plasmons, the combined excitation and emission via long range surface plasmons allowed increasing the peak fluorescence intensity with a factor of 4.4 and squeezing the emission in a cone that exhibited 6-fold narrower full width in half maximum. The results indicate that probing the hydrogel interface by LRSPs and regular SPs leads to similar total fluorescence light intensity collected through the surface plasmon-coupled emission. However, the employing of LRSPs offers the advantage of excitation and emission at lower angles which can simplify the implementation of this method to practical biosensor devices. In addition, the highly directional emission manifested as a narrow emission peak can be more efficiently filtered from the background signal and it can be useful for e.g. angular multiplexing of sensing channels. Our future work will be devoted to the suppressing of competing emission via LRSPs and SRSPs modes by using (nano)structured metallic films and to the implementation of combined SPFS and SPCE with LRSP modes to compact biosensor devices.

Acknowledgments

Alena Aulasevich, Basit Yameen and Martina Knecht from Max Planck Institute for Polymer research in Mainz (Germany) are gratefully acknowledged for the synthesis of NIPPAm polymer and benzophenon-terminated thiol. Partial support for this work was provided by ZIT, Center of Innovation and Technology of Vienna.

#144352 - $15.00 USD Received 18 Mar 2011; revised 7 May 2011; accepted 13 May 2011; published 23 May 2011